

Characterization of Quantum Phase Transitions in Dissipative Cavity QED Systems and Cold Atoms with Disorder

DISSERTATION

zur Erlangung des akademischen Grades

“Doktor der Naturwissenschaften”

an der

Fakultät für Mathematik, Informatik und Physik

der

Leopold-Franzens-Universität Innsbruck

vorgelegt von

Sarah Morrison

2008

ZUSAMMENFASSUNG

Die vorliegende Dissertation befasst sich mit der Entwicklung neuartiger Methoden zur Implementierung und Charakterisierung von Quantenphasenübergängen (QPU) in atomaren Systemen. Sie ist in zwei Abschnitte aufgeteilt: i) Verschränkungsverhalten bei QPU in dissipativen Spinsystemen im Rahmen der optischen Cavity-QED; ii) Ein Schema zur Charakterisierung von ungeordneten Quantensystemen, realisiert durch kalte atomare Gase in optischen Gittern.

Der erste Teil der Dissertation zeigt die Auswirkungen der Dissipation auf das bereits bekannte Auftreten von Verschränungskritikalität in QPU in wechselwirkenden kollektiven Spinsystemen. Es wird ein optischer Cavity-QED Aufbau präsentiert, der ein dissipatives Lipkin-Meshkov-Glick Model für wechselwirkende Spins realisiert und bei dem die aus dem Hohlraumresonator entweichenden Photonen eine quantitative Aussage über das kritische Verhalten des Systems liefern, insbesondere über die Verschränkung zwischen Spinpaaren. Im Fall schwacher Dissipation, das bedeutet, bei dominierender kohärenter Dynamik, stellt sich heraus, dass der wohlbekannte Zweite-Ordnung QPU für ferromagnetische Kopplung erhalten bleibt. Bemerkenswerterweise ergibt aber ein Hinzufügen von Dissipation einen zusätzlichen Erste-Ordnung QPU, welcher in einem äquivalenten geschlossenen System nicht existiert. Eine Analyse der messbaren Spin-Spin Verschränkung im stationären Zustand zeigt ein deutliches Maximum an beiden kritischen Punkten, das mittels einer atomaren Phasenraumverteilung interpretiert wird. Die Dynamik der Verschränkung in dem System weist neben der Kritikalität am QPU für lange Zeiten zudem ein vielschichtiges transientes Verhalten für kurze Zeiten auf.

Im entgegengesetzten Regime mit starker Dissipation verursacht der Wettbewerb zwischen dissipativen und kohärenten Prozessen entweder einen Zweite- oder Erste-Ordnung dissipativen QPU, abhängig allein vom Verhältnis der Systemparameter. Überraschenderweise bleibt die Verschränkung im stationären Zustand am QPU weiterhin maximal, trotz deutlicher Modifikationen gegenüber dem Fall schwacher Dissipation. Zusätzlich weist der Erste-Ordnung Übergang im semiklassischen Limes sowie auch in den messbaren homodynalen Spektren des Ausgangsfeldes des Hohlraumresonators Merkmale von Bistabilität auf.

Der zweite Teil der Dissertation befasst sich mit der Unterscheidung von verschiedenen Phasen in ungeordneten Quantensystemen bei Betrachtung von Korrelationen zwischen unabhängigen Systemen mit identischem Unordnungspotential, sogenannte “Replikas”. Mittels kalte atomare Gase in einem optischen Gitter wird eine neue Methode vorgestellt für die Kreation von Replikas und anschließender Messung der durch die Unordnung induzierten Korrelationen dazwischen, assoziiert mit Quanten-Glas Phasen. Als Anwendung werden Ergebnisse für Korrelationen im ungeordneten Bose-Hubbard Model präsentiert, die zur Identifizierung der Bose-Glas Phase führen.

ABSTRACT

This thesis develops novel schemes to implement and characterize quantum phase transitions (QPTs) using atomic systems. It is divided into two parts: i) Entanglement behavior in the QPT of dissipative spin systems realized in optical cavity QED and ii) A proposal for the characterization of disordered quantum systems implemented with cold atomic gases in optical lattices.

The first part of the thesis determines the effects of dissipation on the well known entanglement criticality occurring in the QPTs of interacting collective spin systems. An optical cavity QED setup is presented which realizes a dissipative Lipkin-Meshkov-Glick model of interacting spins where light emanating from the cavity provides quantitative probes of the critical behavior of the system, including the entanglement between pairs of spins. In the case of weak dissipation, where coherent dynamics predominates, the well known second-order QPT for ferromagnetic coupling is found to persist. Remarkably, the addition of dissipation induces an additional first-order QPT not present in the equivalent closed system. An analysis of the measurable spin-spin entanglement in the steady state shows pronounced maxima at both critical points which can be interpreted using an atomic phase space distribution. The dynamics of the entanglement in this system also exhibits criticality at the QPT at long times as well as a rich transient behavior at shorter times.

In the opposite regime of strong dissipation the competition between dissipative and coherent processes drives either first- or second-order dissipative QPTs depending only on the ratio of system parameters. Surprisingly the steady state entanglement still reaches a maximum at either QPT, despite significant modifications compared to the weak dissipation case. Furthermore, the first-order transition exhibits signatures of bistability in the semiclassical limit and also in the measurable homodyne spectra of the cavity output field.

The second part of the thesis is concerned with distinguishing different phases of a disordered quantum system by considering correlations between independent systems with identical disorder potentials, so-called “replicas”. Utilizing cold atomic gases in an optical lattice a novel method is proposed to create replicas, and subsequently measure the disorder induced correlations between them, associated with quantum glass phases. As an application results for the correlations in the disordered Bose-Hubbard model are presented and shown to help identify the Bose-Glass phase.

CONTENTS

Zusammenfassung	iii
Abstract	v
Contents	vii
General Introduction	1
 I Entanglement in Dissipative Collective Spin Systems	 13
 Chapter 1. Entanglement in quantum phase transitions	 15
1.1 Entanglement Criticality in Closed Systems	16
1.1.1 Entanglement	16
1.1.2 Criticality in quantum phase transitions	16
1.1.3 Example: Lipkin-Meshkov-Glick model	17
1.2 Entanglement and Phase Space	20
1.2.1 Example: Closed Lipkin-Meshkov-Glick model	22
1.2.2 Entanglement criticality in open systems	23
 Chapter 2. Publication: Quantum phase transitions in the dissipative LMG model	 27

Chapter 3. Publication: Collective spin systems in dispersive optical cavity QED	37
3.1 Introduction	37
3.2 Theoretical Model	41
3.2.1 Adiabatic elimination of atomic excited states	41
3.2.2 Adiabatic elimination of the cavity modes	43
3.2.3 Cavity output fields and measurement	44
3.3 Collective (LMG) Spin Models	44
3.3.1 Conventional $\gamma = -1$ LMG model	45
3.3.2 Isotropic $\gamma = 1$ LMG model	46
3.3.3 Simple $\gamma = 0$ LMG model	46
3.3.4 Methods of analysis	47
3.4 Potential Experimental Implementation	47
3.5 Second-Order Phase Transition	49
3.5.1 Linearized model	50
Semiclassical equations of motion and steady-state solutions . .	50
Holstein-Primakoff representation	52
Eigenvalue analysis	53
Probe transmission spectrum	54
3.5.2 Entanglement	57
Entanglement criteria	57
Steady-state entanglement	58
Entanglement dynamics	62
3.6 First-Order Phase Transition	64
3.6.1 Linearized model	64
Semiclassical steady-state solutions	64
Holstein-Primakoff representation	65
Eigenvalue analysis	65
Transmission spectrum	66
3.6.2 Entanglement	67
Steady-state entanglement	67
Entanglement dynamics	70
3.7 Conclusions	70
3.A Coefficients of Atom-Cavity Hamiltonian in the Linearized Regime . .	71

Chapter 4. Microscopic cavity QED system	75
4.1 Atomic System	75
4.2 Cavity System	76
4.3 Atom, Laser and Cavity Coupling	76
4.4 Microscopic Atom-Cavity Model	77
Chapter 5. Adiabatic elimination of the cavity modes	79
5.1 Reduced System	79
5.2 Dispersive and Cross-Cavity Terms	80
5.3 Cavity Correlation Functions and Born-Markov Approximation . . .	81
Chapter 6. Publication: Strongly dissipative collective spins models	83
6.1 Introduction	84
6.2 Cooperative Resonance Fluorescence Model	85
6.2.1 Steady-states	86
6.2.2 Entanglement	88
6.3 Second-Order Transition in Dissipative LMG Model	90
6.3.1 Semiclassical analysis	91
Steady-state solutions	91
Time-dependent solutions	93
6.3.2 Entanglement	94
6.4 First-Order Transition in Dissipative LMG Model	98
6.4.1 Semiclassical analysis	98
Steady-state solutions	98
Time-dependent solutions	100
6.4.2 Entanglement	101
6.4.3 Homodyne spectra	104
6.5 Conclusion	106

II Physical Replicas in Cold Atoms with Disorder 109

Chapter 7. Publication: Physical replicas and the Bose-glass in cold atomic gases	111
7.1 Introduction	112
7.2 Bose-Hubbard model with Disorder	115
7.3 Measurement of the Overlap Function	117
7.3.1 Initial preparation of disorder replicas	117
7.3.2 Measurement process	118
Quantities that need to be measured	120
Combining layers	121
Number distribution characterization	123
7.4 Overlap Function in the Disordered Bose-Hubbard model	127
7.4.1 Analytical determination of the overlap function	127
7.4.2 Numerical results	131
7.5 Conclusion	132
7.A Energy Shifts and Couplings for Three and Four particles	133
7.A.1 Three particles	134
7.A.2 Four particles	135
7.B Perturbation Theory	136
7.B.1 Mott-insulator	137
7.B.2 Bose-glass	138
7.C Mean Field Theory	139
Acknowledgments	145

GENERAL INTRODUCTION

Atomic physics has recently emerged as being one of the most rich and diverse research areas of modern physics due to its suitability for engineering, controlling and observing individual and many-body quantum systems. The vast and rapid experimental developments in the area of cavity quantum electrodynamics (cavity QED) [1, 2] and trapped ultra-cold atomic gases [3] allow for the direct manipulation of atoms and photons, and for the fundamental study of matter-matter [4] and matter-light interactions [5]. These tremendous achievements have lead to many new fascinating and far reaching applications, such as high precision atomic clocks [6, 7], quantum information processing [8–10], simulation of quantum many-body systems [10, 11], and tests of the theory of quantum electrodynamics [12].

Cavity QED traditionally explores the coupling of atoms (or ions) to the confined electromagnetic field of radiation inside a resonator [13]. When the cavity field contains only a few photons, the quantum description of the electromagnetic radiation becomes important and the corresponding strong coupling regime for individual atoms has been observed [14–16]. Employing cold atomic clouds, and improved trapping techniques [17, 18], has enabled cavity QED to enter a new regime where the quantum motion of the atoms can be manipulated by the light force of the cavity field. This advance has lead to important applications including the observation of the motion of atoms inside the cavity [19, 20], cavity cooling of atoms [21, 22], the non-destructive observation of photons inside a cavity [23], and the controlled production of single photons [24–26]. Beyond single atom experiments, collective coupling of multiple cold atoms to the same field mode of the cavity [27] has lead to the observation of collective atomic recoil lasing [28], collective motion and ordering of the atoms [29], and super-radiant Rayleigh scattering [30]. An important aspect of cavity QED systems is the possibility of monitoring the photons that leak out of the cavity, offering a unique window on the system’s behavior and properties via fluorescence and quadrature-variance measurements. Recently, alternative systems that offer the possibility to study cavity QED have emerged such as superconducting qubits coupled to transmission lines cavities [31] and quantum dots in photonic crystal nano-cavities [32].

Dilute atomic gases can now be routinely cooled to the regime where particles exhibit fully quantum behavior by employing the well developed techniques of laser cooling [33], magnetic and optical trapping [33], and evaporative cooling [34]. For bosonic particles this results in the formation of a Bose-Einstein-Condensate at sufficiently low temperatures [35–39], in which all particles occupy the same quantum state and the system exhibits matter-wave coherence. On the other hand, for fermionic particles, at sufficiently low temperatures a quantum degenerate Fermi gas is obtained [40–42], enabling for example the study of fermionic superfluidity [43, 44]. Mixtures of bosonic and fermionic gases have also recently been cooled to quantum degeneracy [45–48] and used to create composite molecules [48] and to observe phase separation [46]. In addition to manipulating atoms by magnetic fields, far-off resonant coherent laser light can be used to generate tailored dipole traps for neutral atoms and to couple the internal states of an atom. The strength and type (repulsive or attractive) of collisional interactions between particles can also be modified using optical [49] and magnetic [50] Feshbach resonances. Importantly, many different techniques have been developed to precisely measure properties of cold trapped gases, for example time-of-flight measurements reveal the momentum distribution of the system.

The common defining feature of the above systems is their suitability for implementing a broad range of quantum many-body systems that can be described accurately and transparently by idealized (but nontrivial) many-body Hamiltonians. Furthermore these systems offer the possibility for quantum critical phenomena, i.e., transitions between distinct quantum phases, in response to variations of an effective field or particle-particle interaction strength around some critical value [51]. It should be noted that in contrast to classical systems, where phase transitions are driven by thermal fluctuations, quantum phase transitions (QPTs) are driven purely by quantum fluctuations. Observing critical behavior of various properties in these system is also straightforward by employing standard measurement techniques.

Cavity QED systems also offer the possibility to study many-body systems with, in particular, long-range interactions due to the collective coupling of all atoms to a single cavity field mode of the resonator. This was first considered by Dicke, who studied the collective effects of atoms coupled to a common single field mode, albeit in a different physical scenario, and showed that the spontaneous emission of the atoms can become enhanced, so called superradiance [52]. Subsequently, it was shown that both a thermal equilibrium phase transition [53] and a QPT [54] occur in the Dicke model, where for sufficiently strong coupling the system can enter the superradiant phase. Recently, generalizations of the Dicke model have emerged, incorporating for example general linear coupling [55], additional short range spin interactions [56], extended ensembles [57], and multiple modes [58], all of which offer the opportunity to study more complex QPT's. A closely related model occurs in nuclear physics, namely the Lipkin-Meshkov-Glick (LMG) model [59] used to describe the behavior of fermions in nuclei. Originally, this model described a collection of spins identically coupled via ferromagnetic interactions, and it was shown that as the coupling strength is varied a

QPT occurs between states of different spin polarization. Similarly to the Dicke model, a generalization of the coupling can lead to different types of QPT, such as continuous and discontinuous [60].

Important insights into quantum phase transitions have been obtained from an analysis of the quantum entanglement properties of critical spin systems [61–64]. Entanglement expresses the presence of non-local quantum correlations [65, 66] and has been the subject of intense study over the last two decades, especially in the context of being a resource for quantum information processing [67]. In the context of QPT’s it has been demonstrated that entanglement between pairs of individual spins, characterized by the so-called concurrence, or between blocks of spins, characterized by the so-called entanglement entropy, can display marked critical behavior and scaling at quantum critical points [64]. Perhaps the most intriguing insight provided by studies of entanglement criticality is the manifestation of universality at the critical point; for example it has been observed that a calculation of the scaling of the entanglement entropy in spin systems is quantitatively equivalent to the entropy of the vacuum in quantum field theories [63]. Despite these exciting developments, the vast majority of studies of entanglement criticality has been restricted to closed systems, with very little being known about entanglement criticality in open dissipative quantum many-body systems [68].

Dissipation in quantum many-body systems adds yet another degree of freedom to a system which can modify an underlying closed system QPT or lead to entirely new dissipation-driven QPTs. For individual systems the effects of dissipation on the same scale as the characteristic frequency are well known [69]. However, only very recently have dissipative many-body systems in condensed matter physics been considered [70], for example the Ising model [71], 1D electron liquids [72], 2D Josephson-Junction arrays [73], and disordered systems [74, 75]. In quantum optical systems, such as cavity QED, dissipation is typically unavoidable and non-equilibrium phase transitions in open collective atomic systems have previously been considered, such as the phenomenon of optical bistability [76] and collective resonance fluorescence [77]. Dissipation will also affect entanglement in a system, and for the case of few body systems this has been intensively studied, especially in the context of quantum computing (see for example [78]). Surprisingly, it has been shown in many systems that despite dissipation and associated decoherence, entanglement can still persist [79–83].

Obviously, entanglement in a dissipative quantum many-body system is of considerable interest and in fact can persist and exhibit criticality at a QPT [68]. Nonetheless a QPT of collective spin models, such as the Dicke model or the LMG model, in optical cavity QED systems remains elusive (despite the long-range interaction provided by the cavity field mode) due to the large frequencies associated with optical fields [84]. Recently, however, a feasible experimental implementation for the Dicke model has been proposed [85] by considering an open cavity QED system that is driven by additional external laser fields involving Raman transitions between atomic ground states. In such an open setup conventional thermal equilibrium transitions are replaced by

dynamical non-equilibrium transitions, and measurements on photons that leak out of the cavity can provide direct information about the energy spectrum or entanglement [85]. Motivated by these findings, a cavity QED setup in the dispersive regime is proposed in part I of this thesis which can be used to realize an open dissipative LMG model. After characterizing the QPTs, the measurable pairwise entanglement in the steady state is determined and shown to reach a maximum at the QPT. For the case of weak dissipation only slight modifications occur compared to the closed system case, whilst in the opposite limit of strong dissipation the QPT is dramatically altered and, surprisingly, entanglement criticality is still exhibited.

By contrast, cold gases in a periodic optical lattice (a standing wave formed by a pair of counter-propagating lasers) can be used to implement a wide variety of quantum lattice models commonly having short range interactions [4, 86, 87]. One of the classic examples is the Bose-Hubbard model [88] describing interacting bosons in an optical lattice, which exhibits a superfluid to Mott-Insulator transition as the interaction strength is varied [89]. Further elementary models include the Fermi-Hubbard model [90], Bose-Fermi mixtures where phases of composite fermions are predicted [91], and low dimensional systems [93–95], where strong quantum fluctuations occur [92]. Changing the geometry of the optical lattice can for example be used to investigate frustrated quantum magnets [96], whilst more elaborate setups, for example involving multiple internal states or coupling to a molecular state, can be used to realize models exhibiting exotic quantum phases [97, 98]. By using dipolar molecules in an optical lattice [99], general lattice-spin models can be realized where the range, strength and anisotropy of the interactions can be completely controlled giving rise, for example, to topological quantum phases [99].

The additional presence of disorder in quantum many-body systems presents another exciting avenue of research, and has been extensively studied in condensed matter systems. Disorder was first considered by Anderson, who showed that a single particle in a static disordered potential can become localized due to coherent back-scattering off random impurities [100]. Since Anderson’s seminal work, much progress has been made towards understanding the role of disorder in many-body systems; for “dirty” electrons (fermions) the phenomenon of weak localization [101] and the Metal-Insulator transition [101, 102] have been extensively studied, as well as the super-conductor to insulator transition in thin super-conducting films [103]. On the other hand, for a system of bosons in a random potential, originally proposed in the context of superfluid ^4He in porous media, the addition of disorder gives rise to an insulating Bose Glass phase [104], characterized by a finite compressibility and vanishing excitation gap. Perhaps one of the most exciting disordered systems though is the much-debated Spin-Glass, which occurs in a collection of spins that are randomly coupled and consequently exhibit frustration due to conflicting couplings [105, 106]. The striking “glassy” behavior of this system is manifested in the observation of the slow dynamics of magnetic properties associated with long relaxation times and randomly frozen directions of individual spins [106]. One of the major difficulties that arises in glass phases in disordered media

is the absence of a simple order parameter distinguishing the different phases of the system. Whilst it has been shown that the correlations between independent systems subjected to the same disorder potential, so-called replicas, can be used to identify a glass phase [107], this generally remains an inaccessible quantity in the disordered materials usually considered in condensed matter physics.

Clearly then, implementing these systems in cold atomic gases, where in contrast to condensed matter systems one has unprecedented control over the system parameters, would provide useful insight into understanding disordered systems. In this vein there have been several proposals recently for the implementation of the Bose-Glass [108], Fermi-Glass [109], and Spin-Glass [109], and for the observation of Anderson Localization [110]. The main challenge from the experimental point of view is the addition of disorder to cold atomic gases which are inherently clean and isolated systems. Laser speckle patterns have been used to implement disordered optical potentials [111–113] and recently this has led to the observation of Anderson Localization [114, 115]. Alternatively, superimposing two optical lattices with incommensurate frequencies results in a quasi-disordered potential [108] and this has been recently used to observe some characteristics of the Bose-Glass [116]. Another implementation for disorder is the use of a mixture of cold gases, where one species is quenched and acts as a local impurity for the second species [110, 117, 118].

The main benefit of using atomic gases to implement disordered systems is the possibility for controlling, in addition to system parameters such as interaction, the aspects of the disorder itself’ for example, a specific random configuration (disorder realization) can be recorded [112] and potentially reused. Another interesting possibility is that the disorder average over many different random realizations, which is generally very difficult to determine theoretically in condensed matter systems, may be calculated by using a superposition of quantum systems each encoded with a different disorder realization [118]. Motivated by these notions, part II of this thesis comprises a proposal of an efficient scheme for (i) the preparation of independent systems of cold atomic gases in an optical lattice subjected to identical disorder potentials, so-called replicas, and (ii) the subsequent measurement of the disorder induced correlations between these replicas. Such a scheme enables one to access the aforementioned order parameters of glass phases and could be used to experimentally distinguish different phases of a disordered system. Whilst the scheme is applicable to any type of one- or two-dimensional disordered system realized with cold atomic gases in an optical lattice, the focus will be on the case of bosons in a random potential where a determination of this order parameter helps identify the Bose-Glass phase.

Overview

This thesis is split into two parts and contains 4 reprinted articles together with supplementary chapters covering additional information not presented in the publications.

Part I of the thesis focuses on entanglement criticality in open dissipative collective spin models that undergo quantum phase transitions. Chapter 1 provides some background to entanglement in QPTs for closed systems. The articles in chapters 2 and 3 summarize an implementation for a dissipative Lipkin-Meshkov-Glick model using a cavity QED setup, and associated studies of the QPTs and corresponding entanglement criticality for the case of weak dissipation. In chapter 4 the detailed microscopic Hamiltonian underlying the proposed cavity QED setup is presented, which has been omitted from the two preceding articles. Chapter 5 contains a detailed derivation of the adiabatic elimination of the cavity modes used to derive the effective spin model of the two preceding chapters. The article in Chapter 6 is concerned with collective spin systems in the regime of strong dissipation and summarizes the study on entanglement criticality for the resonance fluorescence model and the dissipative LMG model.

In part II of the thesis the characterization of disordered systems is considered. The article in chapter 7 summarizes a novel proposal for the measurement of the correlations between systems with identical disorder potential and demonstrates how this can be used to identify the Bose-Glass phase in the disordered Bose-Hubbard model.

Bibliography

- [1] H. Mabuchi and A. C. Doherty, *Science* **298**, 1372 (2002).
- [2] S. Haroche and J. M. Raimond, *Exploring the Quantum*, (Oxford University Press, Oxford, 2006).
- [3] I. Bloch and M. Greiner, *Adv. At. Molec. Opt. Phys.* **52**, 1 (2005).
- [4] I. Bloch, J. Dalibard, and W. Zwerger, arXiv:0704.3011, accepted to *Rev. Mod. Phys.* (2008).
- [5] H. J. Kimble, *Phys. Scr.* **76**, 127 (1998).
- [6] H. S. Margolis, G. P. Barwood, G. Huang, H. A. Klein, S. N. Lea, K. Szymaniec, and P. Gill, *Science* **306**, 1355 (2004).
- [7] W. H. Oskay, S. A. Diddams, E. A. Donley, T. M. Fortier, T. P. Heavner, L. Hollberg, W. M. Itano, S. R. Jefferts, M. J. Delaney, K. Kim, F. Levi, T. E. Parker, and J. C. Bergquist, *Phys. Rev. Lett.* **97**, 020801 (2006) .
- [8] C. H. Bennett and D. P. DiVincenzo, *Nature* **404**, 247 (2000).
- [9] L. M. K. Vandersypen, M. Steffen, G. Breyta, C. S. Yannoni, M. H. Sherwood and I. L. Chuang, *Nature* **414**, 883 (2001).
- [10] J. I. Cirac and P. Zoller, *Physics Today* **57**, 38 (2004).

- [11] S. Lloyd, *Science*, **273**, 1073 (1996).
- [12] B. Odom, D. Hanneke, B. D’Urso, and G. Gabrielse, *Phys. Rev. Lett.* **97**, 030801 (2006).
- [13] P. Berman, ed., *Cavity Quantum Electrodynamics* (Academic Press, Boston, 1994).
- [14] R. J. Thompson, G. Rempe, and H. J. Kimble, *Phys. Rev. Lett.* **68**, 1132 (1992).
- [15] M. Brune, F. Schmidt-Kaler, A. Maali, J. Dreyer, E. Hagley, J. M. Raimond, and S. Haroche, *Phys. Rev. Lett.* **76**, 1800 (1996).
- [16] J. A. Sauer, K. M. Fortier, M. S. Chang, C. D. Hamley, and M. S. Chapman, *Phys. Rev. A* **69**, 051804 (2004).
- [17] J. Ye, D. W. Vernooy, and H. J. Kimble, *Phys. Rev. Lett.* **83**, 4987 (1999).
- [18] J. McKeever, J. R. Buck, A. D. Boozer, A. Kuzmich, H.-C. Nägerl, D.M. Stamper-Kurn, and H. J. Kimble, *Phys. Rev. Lett.* **90**, 133602 (2003).
- [19] C. J. Hood, T. W. Lynn, A. C. Doherty, A. S. Parkins, H. J. Kimble, *Science* **287**, 1447 (2000).
- [20] P. W. H. Pinkse, T. Fischer, P. Maunz, and G. Rempe, *Nature* **404**, 365 (2000).
- [21] P. Horak, G. Hechenblaikner, K. M. Gheri, H. Stecher, and H. Ritsch, *Phys. Rev. Lett.* **79**, 4974 (1997).
- [22] P. Maunz, T. Puppe, I. Schuster, N. Syassen, P. W. H. Pinkse, and G. Rempe, *Nature* **428**, 50 (2004).
- [23] G. Nogues, A. Rauschenbeutel, S. Osnaghi, M. Brune, J. M. Raimond and S. Haroche, *Nature* **400**, 239 (1999).
- [24] J. McKeever, A. Boca, A. D. Boozer, R. Miller, J. R. Buck, A. Kuzmich, and H. J. Kimble, *Science* **303**, 1992 (2004).
- [25] M. Keller, B. Lange, K. Hayasaka, W. Lange, and H. Walther, *Nature* **431**, 1075 (2004).
- [26] M. Hijlkema, B. Weber, H. P. Specht, S. C. Webster, A. Kuhn, and Gerhard Rempe, *Nature Physics* **3**, 253 (2007).
- [27] P. Münstermann, T. Fischer, P. Maunz, P.W. H. Pinkse, and G. Rempe, *Phys. Rev. Lett.* **84**, 4068 (1999).
- [28] D. Kruse, C. von Cube, C. Zimmermann, and Ph.W. Courteille, *Phys. Rev. Lett.* **91**, 183601 (2003).

- [29] C. von Cube, S. Slama, M. Kohler, C. Zimmermann, and Ph.W. Courteille, Fortschr. Physik **54**, 726 (2006).
- [30] S. Slama, S. Bux, G. Krenz, C. Zimmermann, and Ph. W. Courteille, Phys. Rev. Lett. **98**, 053603 (2007).
- [31] A. Wallraff, D. I. Schuster, A. Blais, L. Frunzio, R.-S. Huang, J. Majer, S. Kumar, S. M. Girvin and R. J. Schoelkopf, Nature **431**, 162 (2004).
- [32] A. Badolato, K. Hennessy, M. Atatüre, J. Dreiser, E. Hu, P. M. Petroff, and Atac Imamoğlu, Science **308**, 1158 (2005).
- [33] H. J. Metcalf and P. van der Straten, *Laser Cooling and Trapping*, (Springer, New York, 1999).
- [34] W. Ketterle and N. J. van Druten, Adv. At. Mol. Opt. Phys. **37**, 181 (1996).
- [35] C. Pethick and H. Smith, *Bose-Einstein Condensation in Dilute Gases*, (Cambridge University Press, Cambridge, 2001).
- [36] L. Pitaevskii and S. Stringari, *Bose-Einstein Condensation*, (Oxford University Press, Oxford, 2003).
- [37] M. H. Anderson, J. R. Ensher, M. R. Matthews, C. E. Wieman and E. A. Cornell, Science **269**, 198 (1995).
- [38] C. C. Bradley, C. A. Sackett, J. J. Tollett and R. G. Hulet, Phys. Rev. Lett. **75**, 1687 (1995).
- [39] K. B. Davis, M.-O. Mewes, M. R. Andrews, N. J. van Druten, D. S. Durfee, D. M. Kurn and W. Ketterle, Phys. Rev. Lett. **75**, 3969 (1995).
- [40] B. DeMarco and D.S. Jin, Science **285**, 1703 (1999).
- [41] A. G. Truscott, K. E. Strecker, W. I. McAlexander, G. B. Partridge, and R. G. Hulet, Science **291**, 2570 (2001).
- [42] K. M. O'Hara, S. L. Hemmer, M. E. Gehm, S. R. Granade and J. E. Thomas, Science **298**, 2179 (2002).
- [43] C. Chin, M. Bartenstein, A. Altmeyer, S. Riedl, S. Jochim, J. Hecker Denschlag, and R. Grimm, Science **305**, 1128 (2004).
- [44] M.W. Zwierlein, J.R. Abo-Shaeer, A. Schirotzek, C.H. Schunck, and W. Ketterle, Nature **435**, 1047-1051 (2005).
- [45] G. Modugno, M. Modugno, F. Riboli, G. Roati, and M. Inguscio, Phys. Rev. Lett. **89**, 190404 (2002).

- [46] S. Ospelkaus, C. Ospelkaus, L. Humbert, K. Sengstock, and K. Bongs, Phys. Rev. Lett. **97**, 120403 (2006).
- [47] K. Günter, T. Stöferle, H. Moritz, M. Köhl, and T. Esslinger, Phys. Rev. Lett. **96**, 180402 (2006).
- [48] J. J. Zirbel, K. K. Ni, S. Ospelkaus, J. P. D’Incao, C. E. Wieman, J. Ye, and D. S. Jin, Phys. Rev. Lett. **100**, 143201 (2008).
- [49] M. Theis, G. Thalhammer, K. Winkler, M. Hellwig, G. Ruff, R. Grimm, and J. Hecker Denschlag, Phys. Rev. Lett. **93**, 123001 (2004).
- [50] T. Köhler, K. Góral, and P. S. Julienne, Rev. Mod. Phys. **78**, 1311 (2006).
- [51] S. Sachdev, *Quantum Phase Transitions*, (Cambridge University Press, Cambridge, 2000).
- [52] R. H. Dicke, Phys. Rev. **93**, 99 (1954).
- [53] K. Hepp and E. H. Lieb, Ann. Phys. (N.Y.) **76**, 360 (1973); Phys. Rev. A **8**, 2517 (1973).
- [54] C. Emary and T. Brandes, Phys. Rev. Lett. **90**, 044101 (2003).
- [55] C. Emary and T. Brandes, Phys. Rev. A **69**, 053804 (2004).
- [56] C. F. Lee and N. F. Johnson, Phys. Rev. Lett. **93**, 083001 (2004).
- [57] Y. Li, Z. D. Wang, and C. P. Sun, Phys. Rev. A **74**, 023815 (2006).
- [58] D. Tolkunov and D. Solenov, Phys. Rev. B **75**, 024402 (2007).
- [59] H. J. Lipkin, N. Meshkov, and A. J. Glick, Nucl. Phys. **62**, 188, 199, 211 (1965); N. Meshkov, A. J. Glick, and H. J. Lipkin, *ibid.* **62**, 199 (1965); A. J. Glick, H. J. Lipkin, and N. Meshkov, *ibid.* **62**, 211 (1965).
- [60] J. Vidal, Phys. Rev. A **73**, 062318 (2006).
- [61] T. J. Osborne, and M. A. Nielsen, Phys. Rev. A **66**, 032110 (2002).
- [62] A. Osterloh, L. Amico, G. Falci, and R. Fazio, Nature **416**, 608 (2002).
- [63] G. Vidal, J. I. Latorre, E. Rico, and A. Kitaev, Phys. Rev. Lett. **90** 227902 (2003).
- [64] L. Amico, R. Fazio, A. Osterloh, and V. Vedral, arXiv:quant-ph/0703044v2, accepted to Rev. Mod. Phys. (2007).
- [65] A. Einstein, B. Podolsky, and N. Rosen, Phys. Rev. **47**, 777 (1935).
- [66] J. S. Bell, Physics **1**, 195 (1964).

- [67] M. A. Nielsen and I. L. Chang, *Quantum Computation and Quantum Information*, (Cambridge University Press, Cambridge, 2000).
- [68] S. Schneider and G. J. Milburn, Phys. Rev. A **65**, 042107 (2002).
- [69] A. J. Leggett, S. Chakravarty, A. T. Dorsey, M. P. A. Fisher, A. Garg, and W. Zwerger, Rev. Mod. Phys. **59**, 1 (1987).
- [70] A. Kapitulnik, N. Mason, S. A. Kivelson, and S. Chakravarty, Phys. Rev. B **63**, 125322 (2001).
- [71] P. Werner, K. Völker, M. Troyer, and S. Chakravarty, Phys. Rev. Lett. **94**, 047201 (2005).
- [72] M. A. Cazalilla, F. Sols, and F. Guinea, Phys. Rev. Lett. **97**, 076401 (2006).
- [73] L. Capriotti, A. Cuccoli, A. Fubini, V. Tognetti, and R. Vaia, Phys. Rev. Lett. **94**, 157001 (2005).
- [74] J. A. Hoyos and T. Vojta, Phys. Rev. B **74**, 140401 (2006).
- [75] L. F. Cugliandolo, D. R. Grempel, G. Lozano, and H. Lozza, Phys. Rev. B **70**, 024422 (2004).
- [76] R. Bonifacio and L. A. Lugiato, Phys. Rev. Lett. **40**, 1023 (1978).
- [77] P. D. Drummond and H. J. Carmichael, Opt. Commun. **27**, 160 (1978).
- [78] A. Beige, D. Braun, B. Tregenna, and P. L. Knight, Phys. Rev. Lett. **85**, 1762 (2000).
- [79] S. Bose, I. Fuentes-Guridi, P. L. Knight, and V. Vedral, Phys. Rev. Lett. **87**, 050401 (2001).
- [80] D. Braun, Phys. Rev. Lett. **89**, 277901 (2002).
- [81] M. S. Kim, J. Lee, D. Ahn, and P. L. Knight Phys. Rev. A **65**, 040101 (2002).
- [82] F. Benatti, R. Floreanini, and Marco Piani Phys. Rev. Lett. **91** 070402 (2003).
- [83] M. Bina, F. Casagrande, A. Lulli, and E. Solano, Phys. Rev. A **77**, 033839 (2008).
- [84] G. T. Foster, S. L. Mielke, and L. A. Orozco, Phys. Rev. A **61**, 053821 (2000).
- [85] F. Dimer, B. Estienne, A. S. Parkins, and H. J. Carmichael, Phys. Rev. A **75**, 013804 (2007).
- [86] D. Jaksch and P. Zoller, Ann. Phys. **315**, 52 (2005).

- [87] M. Lewenstein, A. Sanpera, V. Ahufinger, B. Damski, A. Sen, and U. Sen, Adv. Phys. **56**, 243 (2007).
- [88] D. Jaksch, C. Bruder, J. I. Cirac, C. W. Gardiner, and P. Zoller, Phys. Rev. Lett. **81**, 3108 (1998).
- [89] M. Greiner, O. Mandel, T. Esslinger, T. Hänsch, and I. Bloch, Nature **415**, 39 (2002).
- [90] M. Köhl, H. Moritz, T. Stöferle, K. Günter, T. Esslinger, Phys. Rev. Lett. **94**, 080303 (2005).
- [91] M. Lewenstein, L. Santos, M. A. Baranov, and H. Fehrmann, Phys. Rev. Lett. **92**, 050401 (2004).
- [92] T. Giamarchi, *Quantum Physics in One Dimension*, (Oxford University Press, Oxford, 2003).
- [93] B. Paredes, A. Widera, V. Murg, O. Mandel, S Fölling, I. Cirac, G. V. Shlyapnikov, T. W. Hänsch, and Immanuel Bloch, Nature **429**, 277 (2004).
- [94] H. Moritz, T. Stöferle, M. Köhl and T. Esslinger, Phys. Rev. Lett. **91**, 250402 (2003).
- [95] I. B. Spielman, W. D. Phillips, and J. V. Porto, Phys. Rev. Lett. **98**, 080404 (2007).
- [96] L. Santos, M. A. Baranov, J. I. Cirac, H. U. Everts, H. Fehrmann, and M. Lewenstein, Phys. Rev. Lett. **93**, 030601 (2004).
- [97] D. Jaksch, and P. Zoller, New. J. Phys. **5**, 56 (2003).
- [98] H. P. Büchler, M. Hermele, S. D. Huber, M. P. A. Fisher, and P. Zoller, Phys. Rev. Lett. **95**, 040402 (2005).
- [99] A. Micheli, G. K. Brennen, and P. Zoller, Nature Phys. **2**, 341 (2006).
- [100] P. W. Anderson, Phys. Rev. **109**, 1492 (1958).
- [101] P.A. Lee and R.V. Ramakrishnan, Rev. Mod. Phys. **57** 287 (1985).
- [102] D. Belitz, T. R. Kirkpatrick, Rev. Mod. Phys. **66**, 261 (1994).
- [103] Matthew P. A. Fisher and G. Grinstein, Phys. Rev. Lett. **64**, 587 (1990).
- [104] M. P. A. Fisher, P. B. Weichman, G. Grinstein, and D. S. Fisher, Phys. Rev. B **40**, 546 (1989).

- [105] M. Mézard, G. Parisi, and M. A. Virasoro, *Spin Glass Theory and Beyond*, (World Scientific, Singapore, 1987).
- [106] K. Binder and A. P. Young, *Rev. Mod. Phys.* **58**, 801 (1986).
- [107] S. F. Edwards and P. W. Anderson, *J. Phys. F: Met. Phys.* **5**, 965 (1975).
- [108] B. Damski, J. Zakrzewski, L. Santos, P. Zoller, and M. Lewenstein, *Phys. Rev. Lett.*, **91**, 080403 (2003).
- [109] A. Sanpera, A. Kantian, L. Sanchez-Palencia, J. Zakrzewski, and M. Lewenstein, *Phys. Rev. Lett.* **93** 040401 (2004).
- [110] U. Gavish and Yvan Castin, *Phys. Rev. Lett.* **95**, 020401 (2005).
- [111] J. E. Lye, L. Fallani, M. Modugno, D. S. Wiersma, C. Fort, and M. Inguscio, *Phys. Rev. Lett.* **95**, 070401 (2005).
- [112] D. Clément, A. F. Varón, M. Hugbart, J. A. Retter, P. Bouyer, L. Sanchez-Palencia, D.M. Gangardt, G. V. Shlyapnikov, and A. Aspect, *Phys. Rev. Lett.* **95**, 1700409 (2005).
- [113] T. Schulte, S. Drenkelforth, J. Kruse, W. Ertmer, J. Arlt, K. Sacha, J. Zakrzewski, and M. Lewenstein, *Phys. Rev. Lett.* **95**, 170411 (2005).
- [114] J. Billy, V. Josse, Z. Zuo, A. Bernard, B. Hambrecht, P. Lugan, D. Clément, L. Sanchez-Palencia, P. Bouyer, and Alain Aspect, *arXiv:0804.1621* (2008).
- [115] G. Roati, C. D’Errico, L. Fallani, M. Fattori, C. Fort, M. Zaccanti, G. Modugno, M. Modugno, and M. Inguscio, *arXiv:0804.2609* (2008).
- [116] L. Fallani, J. E. Lye, V. Guarrera, C. Fort, and M. Inguscio, *Phys. Rev. Lett.* **98**, 130404 (2007).
- [117] P. Vignolo, Z. Akdeniz, M. P. Tosi, *J. Phys. B* **36**, 4535 (2003).
- [118] B. Paredes, F. Verstraete, and J.I. Cirac, *Phys. Rev. Lett.* **95**, 140501 (2005).

Part I

Entanglement in Dissipative Collective Spin Systems

CHAPTER 1

ENTANGLEMENT IN QUANTUM PHASE TRANSITIONS

In this chapter we wish to give an introduction to the behavior of entanglement in the vicinity of the quantum phase transition (QPT) of a many-body system. For closed systems it is well established that the entanglement of the ground state displays criticality at the QPT [1] due to the presence of long-range quantum correlations in the system. Specifically, in the majority of systems considered the entanglement reaches a maximum at the QPT and is continuous (discontinuous) for a second-order (first-order) QPT. The scaling of the entanglement with finite system size has also been studied extensively and the emergence of universality at the QPT has also been observed.

Whilst entanglement of few particle systems subjected to dissipation has been extensively studied [2–4], much less is known about the behavior of entanglement in open quantum many-body systems [5, 6]. Thus in this part of the thesis (chapters 2 to 6) we study the behavior of entanglement in the open Lipkin-Meshkov-Glick (LMG) model [7] which is a paradigm for quantum many-body systems exhibiting a QPT. In chapters 2 and 3 we consider the cases of weak dissipation and study the behavior of the bi-partite entanglement which, as in the equivalent closed system, is found to peak at the critical point. Then, in chapter 6 we consider the opposite regime of strong dissipation in which a dissipative QPT occurs. In this situation the effects of dissipation become significant but surprisingly we still observe a characteristic peaking of the bipartite entanglement at the QPT.

In section 1.1 of this chapter we give a brief overview of some of the well known entanglement criticality features at the QPT of closed systems, focusing primarily on the results for the LMG model [7]. Then in section 1.2 we will consider a phase space description of many-body systems which can be used to interpret the extremal behavior of entanglement at the QPT.

1.1 Entanglement Criticality in Closed Systems

1.1.1 Entanglement

Entanglement expresses the presence of non-local quantum correlations in a system and its fundamental importance in understanding the behavior of many-body systems has been established. For pure states the amount of bipartite entanglement between two subsystems A and B is usually quantified by the von-Neumann entropy of entanglement [8],

$$S = -\text{Tr}\{\rho_A \log_2 \rho_A\}, \quad (1.1)$$

where $\rho_A = \text{Tr}_B\{\rho\}$ is the reduced density matrix of system A and $\rho = |\psi\rangle\langle\psi|$ with $|\psi\rangle$ the joint state of systems A and B . This measure takes the value zero for a separable state and a value of one for a maximally entangled state (e.g. a Bell state for two level systems). For mixed states the bipartite entanglement can be computed in a number of ways [9]; for the special case of a pair of spin-1/2 systems (a two level system), which we will be our primary interest later on, the bipartite entanglement can be quantified by the concurrence [10],

$$C = \max\{0, \sqrt{\lambda_1} - \sqrt{\lambda_2} - \sqrt{\lambda_3} - \sqrt{\lambda_4}\}, \quad (1.2)$$

where λ_i are the eigenvalues in descending order of the so-called “spin-flipped density matrix”

$$\tilde{\rho} = \rho_{12}(\sigma_{1y} \otimes \sigma_{2y})\rho_{12}^*(\sigma_{1y} \otimes \sigma_{2y}), \quad (1.3)$$

with ρ_{12} the density matrix of the two spins and σ_{iy} the Pauli matrices. The concurrence is zero for a separable state and attains the maximal value of one for the Bell states.

In many-body systems entanglement can arise either between certain subsystems or it can involve all particles simultaneously [9]. For example, if we consider a collection of spin-1/2 systems and imagine partitioning the system into two blocks, then we can quantify the bipartite entanglement between the blocks using the von-Neumann entropy of entanglement. If we consider on the other hand only two spins, by tracing out the remaining spins, the bipartite entanglement of the resulting reduced, mixed state can be quantified by the concurrence. Specifically, for the case of a symmetric spin state the concurrence of any two individual spins is equal and can be computed from the expectation values of the collective spin operators [11]. Whilst quantifying the entanglement between an arbitrary number of spins of a multi-spin system is difficult, for the special case of three spins a measure has recently been derived [12].

1.1.2 Criticality in quantum phase transitions

Quantum phase transitions arise in (interacting) many-body systems at zero temperature as the competition between fluctuations originating from different coherent processes drives the system between fundamentally different ground states as a control

parameter of the system is varied across a critical point [13]. The first studies of entanglement in QPTs focused on a one-dimensional chain of spin 1/2 systems with nearest neighbor interactions, specifically the so-called Ising and XY models [13] were considered. In these systems a QPT occurs as the interaction strength drives the system from the paramagnetic phase to the ferromagnetic phase [13]. Consequently it was shown that as the ground state changes dramatically in the vicinity of the critical point so does its corresponding entanglement. Specifically it was found that the pairwise entanglement, as quantified by the concurrence, peaks close to the QPT [14, 15], whilst the entanglement between two blocks of spins, quantified by the von-Neumann entropy of entanglement, was found to diverge at the critical coupling strength in the thermodynamic limit [16]. Moreover it was shown that the observed finite system size scaling of both the entanglement entropy and the derivative of the concurrence at the critical point exhibit universality¹ [15, 16].

Since then there have been countless studies reporting entanglement criticality in a variety of different systems that display a QPT [1]. For the case of pairwise entanglement the relationship between the non-analyticity of the ground state and the entanglement thereof has been established [17–19]. Recently much progress has also been made in understanding the criticality features of multi-particle entanglement at the QPT of a system [20].

1.1.3 Example: Lipkin-Meshkov-Glick model

In this section we present a summary of the entanglement results found in the LMG collective spin model. To this end let us first introduce the LMG model and briefly explain the quantum phase transition encountered. The LMG model [7] describes the collective interaction between N spin 1/2 systems according to the Hamiltonian

$$H_{\text{LMG}} = -2hJ_z - \frac{2\lambda}{N}(J_x^2 + \gamma J_y^2), \quad (1.4)$$

where h is the magnetic field, λ the interaction strength, $\gamma \in [0, 1]$ is an anisotropy parameter, and J_α , with $\alpha \in \{x, y, z, +, -\}$, are the angular momentum operators obeying $[J_z, J_\pm] = \pm J_\pm$ and $[J_+, J_-] = 2J_z$ ($\hbar = 1$). This Hamiltonian commutes with \mathbf{J}^2 , thus conserving the total angular momentum, and with $e^{i\pi J_z}$, corresponding to a parity (spin-flip) symmetry.

For the case of ferromagnetic interaction ($\lambda > 0$) the ground state lies in the maximal spin sector, $j = N/2$, and thus the effective Hilbert space dimension is reduced from 2^N to $N + 1$ with the basis given by the Dicke states $|j, m\rangle$ with $m \in [-j, -j + 1, \dots, j - 1, j]$. A quantum phase transition occurs for the critical coupling value of $\lambda_c \equiv h$ in the thermodynamic limit ($N \rightarrow \infty$), associated with a fundamental change

¹No dependence on the microscopic details of the system parameters (such as coupling strength and fields).

in the ground state. Below the transition ($\lambda < h$) the system is in the so-called normal phase, where the unique ground state corresponds to the collective spin being polarized in the direction of the magnetic field. Above the critical point ($\lambda > h$) the system enters the so-called broken phase, here the ground state becomes doubly degenerate due to the breaking of the parity symmetry, and the collective spin can now be oriented in one of two directions displaced from the z -axis (magnetic field direction). Note that for the case of isotropic interaction i.e. $\gamma = 1$ the Hamiltonian can be exactly solved due to the (additional) conservation of the z component of angular momentum ($[H_{\text{LMG}}, J_z] = 0$). We note that for finite system size the parity is conserved and the ground state remains unique in the broken phase.

We now consider the behavior of the pairwise entanglement, as quantified by the rescaled concurrence,² $C_R \equiv (N - 1)C$, of the ground state of the LMG model as the coupling strength is varied across the QPT. Initial numerical calculations of the concurrence [21] for finite system sized showed that the concurrence peaked at the critical point (see Fig. 1.1), whilst its derivative diverged at the critical point [21]. Subsequent analytical calculations, based on the Holstein Primakov representation of angular momentum operators and the continuous unitary transformation technique [22], focused on the thermodynamic limit and determined the scaling behavior of the concurrence with finite system size at the critical point.

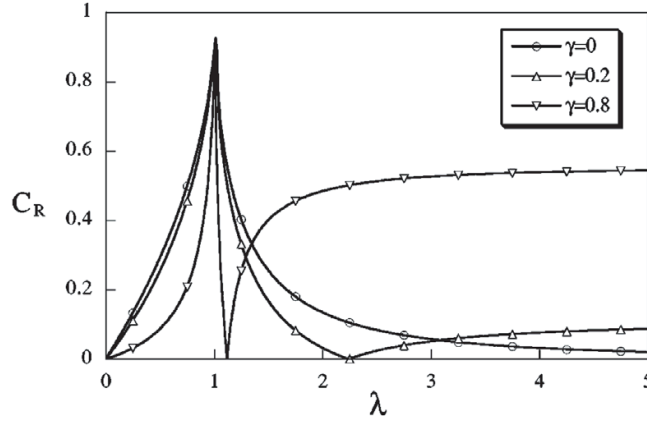


Figure 1.1. *Rescaled concurrence of the ground state as a function of λ for different values of γ , $N = 1000$, and $h = 1$. Figure reproduced with permission of J. Vidal from Ref. [21].*

We now focus on the special case of $\gamma = 0$ and relate the observed entanglement behavior directly to the ground state. In the normal phase ($\lambda < h$) where the magnetic field term of the Hamiltonian is dominant the entanglement is small since the ground state is close to the unentangled state $|j, j\rangle$. Similarly in the broken phase ($\lambda > h$) when

²Note that for the infinitely coordinated systems considered here, the rescaling is necessary to give the correct non-trivial entanglement behavior, since the concurrence itself scales inversely with the system size due to the infinite range interactions [21].

the interactions dominate the state again is expected to have little entanglement as it approaches an eigenstate of J_x (at finite N it approaches a superposition of positive and negative J_x eigenstates). However when the interaction and magnetic field are comparable, i.e. near the critical point, the state is generally a superposition of Dicke states which is of course highly entangled.

Next we consider the entanglement between two spin blocks of size L and $N - L$, as quantified by the von-Neumann entropy of entanglement, of the ground state in the LMG as a function of the coupling strength. Both numerical calculations for finite system size and analytical calculations in the thermodynamic limit show that the entanglement entropy diverges logarithmically at the critical point [23] (see Fig. 1.2). Similarly to the concurrence, in the normal phase ($h > \lambda$) the entanglement entropy is small, however, in the broken phase ($h < \lambda$) the entanglement entropy approaches a constant non-zero value, in contrast to the behavior of the concurrence.

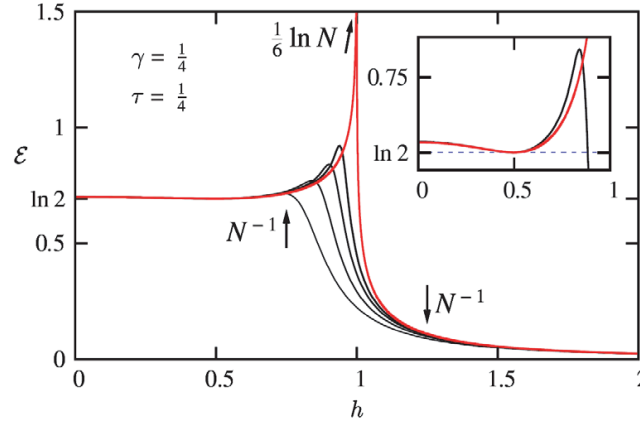


Figure 1.2. Entanglement entropy, denoted \mathcal{E} , as a function of the magnetic field, with fixed $\lambda = 1$, $\gamma = 1/4$, $\tau = 1/4$ where $\tau = N/L$, and $N = 32, 64, 128, 256$ (from numerics) and ∞ ($\mathcal{E}^{(0)}$). Arrows indicate the behavior of the finite-size correction in various regions. The inset is a zoom around $h = \sqrt{\gamma}$ where $\mathcal{E}^{(0)} = 0$, for $N = 64$ (black line) and ∞ (gray line). The expression for $\mathcal{E}^{(0)}$ is given in [23]. Figure reproduced with permission of J. Vidal from Ref. [23].

Let us now turn to the case of anti-ferromagnetic interaction ($\lambda < 0$) where a first order QPT occurs for a critical field strength of $h_c \equiv 0$ in the thermodynamic limit [24]. In the regime of weak interactions the ground state again corresponds to the collective spin being polarized in the direction of the magnetic field. In the opposite limit of strong interactions the Hamiltonian is minimized by a state in the small spin sector $j \ll N/2$, specifically at the critical point the ground state corresponds to a state of zero spin. For finite system size and $0 < h < h_{\text{SUSY}}$, where h_{SUSY} is the so-called supersymmetric point [24], the spin sector of the ground state is for even N $j = 0$ and for odd N $0 < j < N/2$. We note however that in the thermodynamic limit the

super-symmetric point approaches the critical field value, h_c , and thus a discontinuity in the ground state (from spin $j = N/2$ to spin $j = 0$) occurs corresponding to a first-order QPT. Correspondingly the pairwise entanglement is found to be maximal and discontinuous at the critical point [24] (see Fig. 1.3).

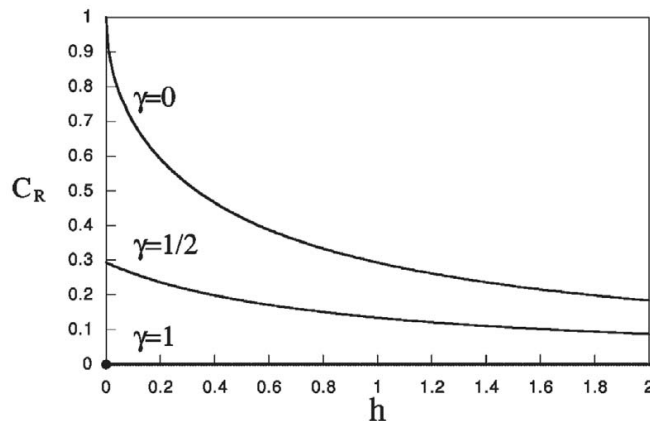


Figure 1.3. *Rescaled concurrence of the ground state as a function of the magnetic field for various anisotropy parameter γ and for $N = 10^3$ spins ($\lambda = -1$). Note that for any γ , one has $C_R = 0$ at zero field. Figure reproduced with permission of J. Vidal from Ref. [24].*

Finally we note that entanglement dynamics in the LMG model have also been studied in Ref. [25] for two different initially unentangled states. In particular, for the rescaled concurrence it was shown that for an initial state polarized in the x direction very little entanglement is ever produced, and for long times the rescaled concurrence always vanishes for any choice of system parameters. However, for a state initially polarized in the z direction it was shown that the rescaled concurrence is both significant and long-lived entanglement in the normal phase of the system (weak interaction).

1.2 Entanglement and Phase Space

In this section we pursue an explanation of the extremal behavior of entanglement at the critical point of a QPT by studying the ground state of the system in a phase space representation. Recently the phase space representation of many-body systems was considered by introducing generalized many-body coherent states for both the case of distinguishable and indistinguishable particles [26, 27]. The state of the system is most conveniently represented in phase space using the so-called Q -function (or Husimi function), defined as

$$Q(\xi) = \langle \xi | \rho | \xi \rangle, \quad (1.5)$$

where ρ is the density matrix describing the state of the system and $|\xi\rangle = |\xi_1\rangle \otimes |\xi_2\rangle \otimes \cdots \otimes |\xi_n\rangle$ are the many-body coherent states parameterized by the complex numbers ξ_i . We will consider the case of a pure state $|\psi\rangle$ which then gives $Q(\xi) = |\langle\xi|\psi\rangle|^2$.

Recall that coherent states closely resemble classical behavior and are represented by a localized distribution of the Q -function in phase space³. Now let us consider the so-called Rényi-Wehrl entropy of a state defined by [28]

$$S_{|\psi\rangle}^{(q)} \equiv \frac{1}{1-q} \ln M_{|\psi\rangle}^{(q)}, \quad (1.6)$$

where the moments of the Q -function are given by

$$M_{|\psi\rangle}^{(q)} = c \int d\mu(\xi) \{Q(\xi)\}^q, \quad (1.7)$$

with c a normalization constant and $d\mu(\xi)$ the Haar measure of the group [26, 28]. $S_{|\psi\rangle}^{(q)}$ is considered to be a measure of the effective volume that the Q -function occupies in phase space [28], and it has been conjectured (and in some special cases proven) that it should take a minimum value for coherent states. Thus it was suggested in Ref. [26] that large values of the Rényi-Wehrl entropy, associated with a delocalized Q -function, should indicate quantum correlated, i.e., entangled states. For the special case of a pair of qubits in a pure state it was shown that the moments of the Q -function can be directly related to the concurrence [26]. Furthermore, it was then shown that for pure states $S_{|\psi\rangle}^{(q)}$ is in fact a bipartite entanglement monotone (measure) [27].

Now that we understand the relationship between entanglement and the representation of a state in phase space, i.e., its Q -function, we can consider what happens in a QPT. In Ref. [29] it was shown that the QPT in a system can in fact be related to a bifurcation at the critical point of the fixed points of the corresponding semi-classical system. A bifurcation corresponds to a change in stability of the fixed points of a system as a “control” parameter is varied across a “critical” value. The typical situation encountered is schematically depicted in Fig. 1.4 corresponding to a supercritical pitchfork bifurcation: a single stable steady state becomes unstable and two new stable steady states emerge. Well away from the transition point the fixed points are well separated, whilst in the vicinity of the critical point they are more closely spaced and eventually merge at the critical point.

Importantly it was shown that the Q -function is expected to be concentrated around the locations of the classical counterpart fixed points. Applying this to a QPT with a pitchfork bifurcation of the semi-classical fixed point, we expect that well away from a QPT the Q -function is localized around the individual fixed points and thus has little entanglement⁴. However, in the vicinity of the critical point, where the fixed

³For the coherent states of the (quantum) harmonic oscillator, i.e. $|\alpha\rangle$, $Q(\alpha)$ is in fact Gaussian.

⁴Note that in the regime of two stable fixed points, $\lambda > \lambda_c$, quantum correlation associated with each individual fixed point is small (localized), however it is still possible that entanglement can be significant as a superposition may be formed.

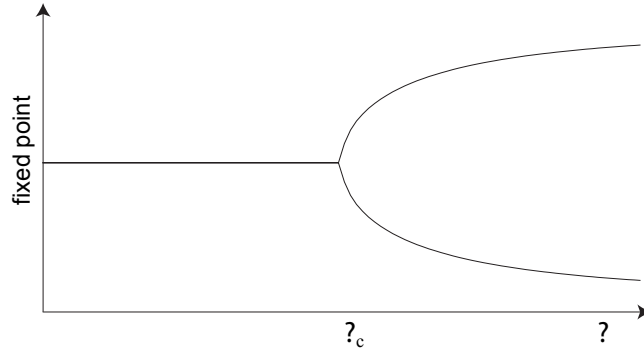


Figure 1.4. *A supercritical pitchfork bifurcation as encountered in the classical counterpart of certain QPTs. As the control parameter λ is varied across the critical value of λ_c the single stable steady present for $\lambda < \lambda_c$ becomes unstable whilst two new stable states emerge in the regime $\lambda > \lambda_c$.*

points lie close together, the Q -function can become delocalized as it spreads across the different fixed points and correspondingly substantial entanglement is present. At the critical point itself the Q -function is expected to achieve its maximum delocalization as the fixed points merge and hence the entanglement should be maximal at this point. This concludes our general discussion about the entanglement and phase space representation in QPT's, and we now proceed to give a specific example for the LMG model.

1.2.1 Example: Closed Lipkin-Meshkov-Glick model

In this section we study the Q -function of the ground state of the ferromagnetic LMG model and use this to interpret the entanglement behavior of the QPT. Since the LMG model describes identical (long-range) interaction between all particles, the correlation functions between any two particles, responsible for pairwise entanglement, is identical. Moreover, as already mentioned previously in the context of the concurrence, the two body correlation functions can in fact be related to correlation functions of the collective system [11]. Thus we will argue that the essential features of the many-body Q -function, such as its delocalization, are in fact captured by the Q -function of the collective system. We recall that the coherent states for a collective spin system are given by the atomic coherent states

$$|\eta\rangle = (1 + |\eta|^2)^{-j} \sum_{m=-j}^j \sqrt{\binom{N}{j+m}} \eta^{j+m} |j, m\rangle, \quad (1.8)$$

where $\eta = e^{i\phi} \tan \frac{\theta}{2}$, with θ and ϕ corresponding to spherical coordinates, and $|j, m\rangle$ are the Dicke states with $m \in [-j, -j+1, \dots, j-1, j]$ (for our system, $j = N/2$). Thus we

can now study the so-called spin Q -function of the ground state $|\psi\rangle$: $Q_s(\eta) \equiv |\langle\eta|\psi\rangle|^2$ (see previous discussion for general definition of the Q -function).

For the ferromagnetic LMG model an analysis of the stable fixed points of its classical counterpart shows that a super-critical pitchfork bifurcation, as illustrated in Fig. 1.4, occurs. For the open-LMG model the bifurcation is calculated in great detail in the following two chapters and since this situation is qualitatively analogous to the closed system we will not present explicit results here.

In Fig. 1.5 we plot Q_s for several different values of the coupling strength λ on the Bloch sphere. We can see that below the critical point ($\lambda < h$), $Q_s(\eta)$ is localized around the unique fixed point at the top of the Bloch sphere ($\theta = 0$) and consequently entanglement is small in this region. Close to the critical point $Q_s(\eta)$ becomes delocalized and significant entanglement is observed (see Fig. 1.1 for $\gamma = 0$). Above the critical point ($\lambda > h$) $Q_s(\eta)$ is now localized around the two new stable fixed points and again entanglement is small in this region.

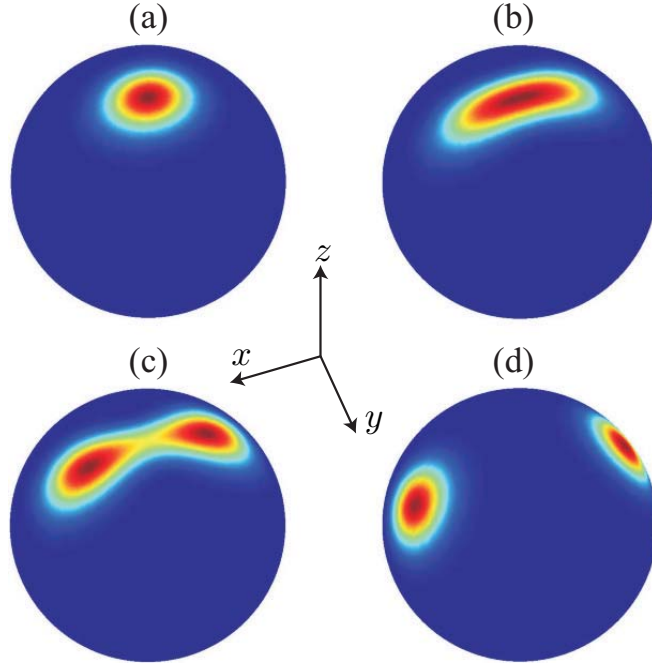


Figure 1.5. *Steady state spin Q -function, $Q_s(\eta)$, on the Bloch sphere for (a) $\lambda = 0.5$, (b) $\lambda = 1.1$, (c) $\lambda = 1.2025$, and (d) $\lambda = 1.75$, with $N = 50$, $h = 1$. Note that dark blue corresponds to the minimum value of zero of $Q_s(\eta)$ whilst dark red indicates the maximum value of $Q_s(\eta)$.*

1.2.2 Entanglement criticality in open systems

So far we have discussed in detail the behavior of entanglement at the QPT of a closed many-body system. In this final section we consider applying the ideas of the previous

section to an open system. For an open system the Q -function of the steady state of the system should be considered, i.e., $Q(\xi) = \langle \xi | \rho_{ss} | \xi \rangle$, where ρ_{ss} is the steady-state density matrix, which is of course in general a mixed state. However, if the dissipation in the open system is weak then we expect the system to exhibit primarily coherent behavior. Thus the Q -function of the steady state should exhibit similar behavior to the closed system case, i.e., localized at the fixed points well away from the transition and delocalized at the transition, and thus we would still expect that entanglement peaks at the QPT. Indeed for the open LMG model considered in the following two chapters we find precisely this behavior of the Q -function⁵ together with extremal behavior of the entanglement.

In the case of strong dissipation the QPT of a system will be modified drastically; specifically it is possible in this regime that the dissipation itself drives a quantum phase transition as competition between coherent and dissipative processes occur. In this case the above arguments cannot be applied as the state will generally be highly mixed. We note however, for the system studied in chapter ... that nonetheless a supercritical fixed point bifurcation occurs and consequently the entanglement is still observed to be maximal at the QPT. This seems to suggest that the explanation of entanglement in a QPT due to a delocalization of the Q -function still holds for dissipative cases. We note that this was already observed in [5], prior to the work on closed systems, and it seems that this could probably be proved now by generalizing the work of [26, 27, 29] to the case of open systems.

Bibliography

- [1] L. Amico, R. Fazio, A. Osterloh, and V. Vedral, arXiv:quant-ph/0703044v2, accepted to Rev. Mod. Phys. (2007).
- [2] M. Bina, F. Casagrande, A. Lulli, and E. Solano, Phys. Rev. A **77**, 033839 (2008).
- [3] F. Benatti, R. Floreanini, and Marco Piani Phys. Rev. Lett. **91** 070402 (2003).
- [4] M. S. Kim, J. Lee, D. Ahn, and P. L. Knight Phys. Rev. A **65**, 040101 (2002).
- [5] S. Schneider and G. J. Milburn, Phys. Rev. A **65**, 042107 (2002).
- [6] F. Dimer, B. Estienne, A. S. Parkins, and H. J. Carmichael, Phys. Rev. A **75**, 013804 (2007).
- [7] H. J. Lipkin, N. Meshkov, and A. J. Glick, Nucl. Phys. **62**, 188, 199, 211 (1965); N. Meshkov, A. J. Glick, and H. J. Lipkin, *ibid.* **62**, 199 (1965); A. J. Glick, H. J. Lipkin, and N. Meshkov, *ibid.* **62**, 211 (1965).

⁵As already mentioned in the previous section the fixed point structure of the open and closed system is the same, and dissipation can be considered as a modification to the closed system behavior

- [8] M. A. Nielsen and I. L. Chang, *Quantum Computation and Quantum Information*, (Cambridge University Press, Cambridge, 2000).
- [9] M. B. Plenio and S. Virmani, *Quant. Inf. Comp.* **7**, 1 (2007).
- [10] W. K. Wootters, *Quant. Inf. Comp.* **1**, 27 (2001).
- [11] X. Wang and K. Mølmer, *Eur. Phys. J. D* **18**, 385 (2002).
- [12] J. K. Korbicz, J. I. Cirac, and M. Lewenstein, *Phys. Rev. Lett.* **95**, 120502 (2005); *ibid.* **95**, 259901 (2005).
- [13] S. Sachdev, *Quantum Phase Transitions*, (Cambridge University Press, Cambridge, 2000).
- [14] T. J. Osborne, and M. A. Nielsen, *Phys. Rev. A* **66**, 032110 (2002).
- [15] A. Osterloh, L. Amico, G. Falci, and R. Fazio, *Nature* **416**, 608 (2002).
- [16] G. Vidal, J. I. Latorre, E. Rico, and A. Kitaev, *Phys. Rev. Lett.* **90** 227902 (2003).
- [17] L.-A. Wu, M. S. Sarandy, and D. A. Lidar, *Phys. Rev. Lett.* **93**, 250404 (2004).
L.-A. Wu, M. S. Sarandy, D. A. Lidar, and L. J. Sham, *Phys. Rev. A* **74** (2006).
- [18] H. L. Haselgrove, M. A. Nielsen, and T. J. Osborne, *Phys. Rev. A* **69**, 032303 (2004).
- [19] L. Campos Venuti, C. Degli Esposti Boschi, M. Roncaglia, and A. Scaramucci, *Phys. Rev. A* **73**, 010303 (2006).
- [20] T. R. de Oliveira, G. Rigolin, M. C. de Oliveira, and E. Miranda, *Phys. Rev. Lett.* **97**, 170401 (2006).
- [21] J. Vidal, G. Palacios, and R. Mosseri, *Phys. Rev. A* **69**, 022107 (2004).
- [22] S. Dusuel and J. Vidal, *Phys. Rev. B* **71**, 224420 (2005).
- [23] T. Barthel, S. Dusuel, and J. Vidal, *Phys. Rev. Lett.* **97**, 220402 (2006).
- [24] J. Vidal, R. Mosseri, and J. Dukelsky, *Phys. Rev. A*, **69**, 054101 (2004).
- [25] J. Vidal, G. Palacios, and C. Aslangul, *Phys. Rev. A* **70**, 062304 (2004).
- [26] A. Sugita, *J. Phys. A* **36**, 9081 (2003).
- [27] F. Mintert and K. Zyczkowski, *Phys. Rev. A* **69**, 022317 (2004).
- [28] S. Gnutzmann and K. Zyczkowski, *J. Phys. A* **34**, 10123 (2001).
- [29] A. P. Hines, R. H. McKenzie, and G. J. Milburn, *Phys. Rev. A* **71**, 042303 (2005).

CHAPTER 2

PUBLICATION

Dynamical quantum phase transitions in the dissipative Lipkin-Meshkov-Glick model with proposed realization in optical cavity QED

Physical Review Letters **100**, 040403 (2008)

S. Morrison^{1,2} and A. S. Parkins³

1) Institute for Theoretical Physics, University of Innsbruck, Innsbruck A-6020, Austria

2) Institute for Quantum Optics and Quantum Information of the Austrian Academy of Sciences, A-6020 Innsbruck, Austria

3) Department of Physics, University of Auckland, Private Bag 92019, Auckland, New Zealand

We present an optical cavity QED configuration that is described by a dissipative version of the Lipkin-Meshkov-Glick model of an infinitely coordinated spin system. This open quantum system exhibits both first- and second-order nonequilibrium quantum phase transitions as a single, effective field parameter is varied. Light emitted from the cavity offers measurable signatures of the critical behavior, including that of the spin-spin entanglement.

Remarkable advances with trapped, ultra-cold atomic gases have opened up exciting new avenues of research into strongly interacting many-body quantum systems [1]. Exquisite control of both motional and electronic degrees of freedom of cold atoms can enable one to “tailor” atom-atom interactions and thereby implement a variety of systems that exhibit, in particular, quantum critical phenomena, i.e., transitions between distinct quantum phases, driven by quantum fluctuations, in response to variations of an effective field or interaction strength around some critical value.

Recently, important insights into such transitions have been obtained from theoretical studies of the quantum entanglement properties of critical spin systems (see, e.g., [2–10]). Bipartite entanglement measures characterizing entanglement between a pair of spins (e.g., the concurrence) or between two blocks of spins (e.g., the entanglement entropy) can display marked critical behavior and scaling at quantum critical points. In this context, a simple but very useful example is the Lipkin-Meshkov-Glick (LMG) model [11], which is described by the Hamiltonian

$$H_{\text{LMG}} = -2hJ_z - (2\lambda/N)(J_x^2 + \gamma J_y^2), \quad (2.1)$$

where $\{J_x, J_y, J_z\}$ are collective angular momentum operators for N spin-1/2 particles, h and λ are effective magnetic field and spin-spin interaction strengths, respectively, and $\gamma \in [-1, 1]$ is an anisotropy parameter. This system, in which each spin interacts identically with every other spin, exhibits critical behavior at zero temperature; in particular, either first- or second-order equilibrium quantum phase transitions may occur, depending on the choice of λ and γ , as the ratio h/λ is varied across a critical value [6]. Notably, the second-order transition involves a change from a unique ground state (normal phase) to a pair of macroscopically displaced degenerate ground states (broken phase). Entanglement in the system displays the above-mentioned critical behavior, reaching, in particular, a pronounced maximum at the critical point [5–7].

Given these interesting and topical features of the LMG model, it follows that the physical realization of a system described by such a model would provide a valuable test bed for studies of quantum critical phenomena and entanglement. Here we propose an open-system (i.e., dissipative) version of the LMG model based on the collective interaction of an ensemble of atoms with laser fields and field modes of a high-finesse optical resonator. In the spirit of a recent proposal for realizing the Dicke model [12], our scheme employs Raman transitions between a pair of atomic ground states and the relevant energy scales (e.g., h , λ) are set by light shifts of the atomic levels and Raman transition rates and detunings.

The open nature of this system, a consequence of the external driving fields and cavity mode losses, introduces a number of important differences from, and, arguably, advantages over, the closed, Hamiltonian LMG system: (i) thermal equilibrium phase transitions are replaced by dynamical, nonequilibrium phase transitions, (ii) the cavity output fields offer quantitative measures of properties of the collective-spin system, including entanglement, in the critical regime, and (iii) it is possible to observe both first- and second-order quantum phase transitions as a *single effective field parameter*, h , is varied.

We consider N atoms coupled via electric dipole transitions to three laser fields and to a pair of independent (e.g., orthogonally-polarized) optical cavity modes. The atomic level and excitation scheme is shown in Fig. 2.1, together with a possible ring-cavity setup. At the location of the atoms, the cavity and laser fields are copropagating traveling waves, with sufficiently broad beam waists so as to ensure homogeneous atom-field couplings. These fields combine to drive Raman transitions between two stable

electronic ground states of the atoms, $|0\rangle$ and $|1\rangle$ (energies $\omega_0 = 0$ and ω_1 , respectively, with $\hbar = 1$) via the excited atomic states $|r\rangle$ and $|s\rangle$ (energies ω_r and ω_s). The laser fields have optical frequencies ω_{r0} , ω_{s0} , and ω_{r1} , and couple to the atomic transitions with Rabi frequencies Ω_{r0} , Ω_{s0} , and Ω_{r1} . Cavity field a , at frequency ω_a , couples to the transitions $|0\rangle \leftrightarrow |r\rangle$ and $|1\rangle \leftrightarrow |s\rangle$ with strengths g_{r0} and g_{s1} , respectively, while cavity field b , at frequency ω_b , couples to the transitions $|0\rangle \leftrightarrow |s\rangle$ and $|1\rangle \leftrightarrow |r\rangle$ with strengths g_{s0} and g_{r1} , respectively. As drawn in Fig. 2.1, the level scheme would apply, e.g., to ^6Li , with the ground magnetic substates $|F = 1/2, m = \pm 1/2\rangle$ as $|0\rangle$ and $|1\rangle$ and a magnetic field perpendicular to the cavity axis to provide a splitting ω_1 between these states. Modes a and b would be orthogonal, linearly-polarized cavity modes, with mode a polarized along the direction of the magnetic field.

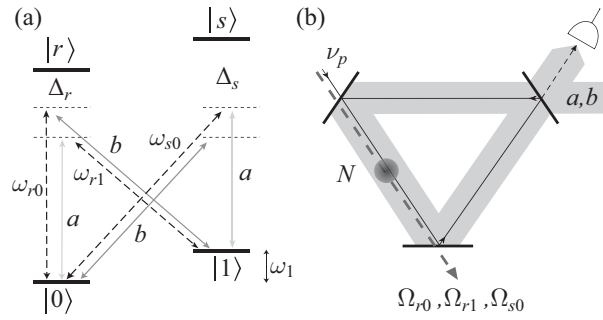


Figure 2.1. (a) Atomic level and excitation scheme. (b) Potential ring-cavity setup. The laser fields (dashed lines) are at frequencies that are not supported by the resonator, but can be injected through one of the resonator mirrors so as to be co-propagating with the cavity fields through the ensemble.

The atom-light detunings $\Delta_r = \omega_r - \omega_{r0}$ and $\Delta_s = \omega_s - \omega_{s0}$ are taken to be much larger than any dipole coupling strengths, atomic linewidths, or cavity loss rates. This enables us to adiabatically eliminate the states $|r\rangle$ and $|s\rangle$ from the dynamics and neglect the effects of atomic spontaneous emission. Additionally, as depicted in Fig. 2.1, we assume that only three distinct Raman transitions are of significance (i.e., resonant or roughly resonant); i.e., we retain only those Raman processes that cause a change in the electronic state of the atoms ($|0\rangle \rightarrow |1\rangle$ or $|1\rangle \rightarrow |0\rangle$) and also involve transfer of a photon from a laser field to a cavity mode or vice-versa. All other possible Raman processes are assumed to be far off-resonant and therefore negligible. Finally, taking the wave numbers of the laser and cavity fields to be essentially equal, and introducing the collective spin operators $J_z = \frac{1}{2} \sum_{j=1}^N (|1_j\rangle\langle 1_j| - |0_j\rangle\langle 0_j|)$, $J_+ = \sum_{j=1}^N |1_j\rangle\langle 0_j|$, and $J_- = (J_+)^\dagger$, we can derive a master equation for the cavity modes and ground-state atoms in the form

$$\dot{\rho}_g = -i[H_g, \rho_g] + \kappa_a D[a] \rho_g + \kappa_b D[b] \rho_g, \quad (2.2)$$

where $D[A]\rho = 2A\rho A^\dagger - A^\dagger A\rho - \rho A^\dagger A$, $\kappa_{a,b}$ are the cavity field decay rates, and

(omitting constant energy terms)

$$\begin{aligned}
 H_g = & \omega_0 J_z + \delta_a a^\dagger a + \delta_b b^\dagger b + 2\delta_a^- J_z a^\dagger a + 2\delta_b^- J_z b^\dagger b \\
 & + \frac{\lambda_a}{\sqrt{N}} J_x (a + a^\dagger) + \frac{\lambda_b}{\sqrt{N}} (J_- b + J_+ b^\dagger),
 \end{aligned} \tag{2.3}$$

with $J_x = (J_+ + J_-)/2$ and

$$\omega_0 = \frac{|\Omega_{r1}|^2}{4\Delta_r} - \frac{|\Omega_{r0}|^2}{4\Delta_r} - \frac{|\Omega_{s0}|^2}{4\Delta_s} + \omega_1 - \omega'_1, \tag{2.4a}$$

$$\delta_a = \omega_a + \omega'_1 - \omega_{s0} + N\delta_a^+, \tag{2.4b}$$

$$\delta_b = \omega_b + \omega'_1 - \omega_{r0} + N\delta_b^+, \tag{2.4c}$$

$$\delta_a^\pm = \frac{|g_{s1}|^2}{2\Delta_s} \pm \frac{|g_{r0}|^2}{2\Delta_r}, \quad \delta_b^\pm = \frac{|g_{r1}|^2}{2\Delta_r} \pm \frac{|g_{s0}|^2}{2\Delta_s}, \tag{2.4d}$$

$$\lambda_a = \frac{\sqrt{N}\Omega_{r1}^* g_{r0}}{\Delta_r} = \frac{\sqrt{N}\Omega_{s0}^* g_{s1}}{\Delta_s}, \quad \lambda_b = \frac{\sqrt{N}\Omega_{r0}^* g_{r1}}{2\Delta_r}, \tag{2.4e}$$

where $\omega'_1 = (\omega_{s0} - \omega_{r1})/2 \simeq \omega_1$, and we have assumed the two Raman transitions involving mode a to occur at the same rate λ_a .

We now assume $(\kappa_i^2 + \delta_i^2)^{1/2} \gg \lambda_a, \lambda_b, \omega_0$. In this limit, the cavity modes are only weakly or virtually excited and may also be adiabatically eliminated to yield the following master equation for the reduced density operator, ρ , of the collective atomic system alone:

$$\dot{\rho} = -i[H_{LMG}^{\gamma=0}, \rho] + \frac{\Gamma_a}{N} D[2J_x]\rho + \frac{\Gamma_b}{N} D[J_+]\rho, \tag{2.5}$$

with $h = -\omega_0/2$, $\lambda = 2\lambda_a^2\delta_a/(\kappa_a^2 + \delta_a^2)$, and $\Gamma_i = \lambda_i^2\kappa_i/(\kappa_i^2 + \delta_i^2)$ ($i = a, b$). Note that in deriving (2.5) we have also assumed that $\kappa_b \gg \delta_b \simeq 0$. If we then take $\delta_a \gg \kappa_a$ and $\Gamma_a \ll \Gamma_b$, then the role played by each cavity mode in relation to the atomic system is quite distinct. Specifically, mode a mediates the collective spin-spin interaction (of strength $\lambda \simeq \lambda_a^2/\delta_a$) associated with the Hamiltonian dynamics, whilst mode b mediates the collective atomic decay (with rate $\Gamma_b \simeq \lambda_b^2/\kappa_b$).

The equations of motion for the moments $\{\langle J_x \rangle, \langle J_y \rangle, \langle J_z \rangle\}$, derived from (2.5), do not form a closed set. However, factorizing the means of operator products and taking the limit $N \rightarrow \infty$ (i.e., neglecting quantum fluctuations), we obtain a closed set of semiclassical equations,

$$\dot{X} = 2hY - \Gamma_b ZX, \tag{2.6a}$$

$$\dot{Y} = -2hX + 2\lambda ZX - \Gamma_b ZY, \tag{2.6b}$$

$$\dot{Z} = -2\lambda XY + \Gamma_b(X^2 + Y^2), \tag{2.6c}$$

where $(X, Y, Z) \equiv (\langle J_x \rangle, \langle J_y \rangle, \langle J_z \rangle)/j$ with $j = N/2$, and $X^2 + Y^2 + Z^2 = 1$ (conservation of angular momentum). The stable steady-state solutions of (6) exhibit bifurcations at

two critical effective field strengths, $h_{\pm}^c = [\lambda \pm (\lambda^2 - \Gamma_b^2)^{1/2}]/2$ (we assume $\lambda > 0, \Gamma_b$). In particular, for $h < h_-^c$ and $h > h_+^c$ the stable steady-state solutions are $\{X_{ss} = Y_{ss} = 0, Z_{ss} = 1\}$, whereas for $h_-^c < h < h_+^c$ one finds

$$X_{ss} = \pm \sqrt{\frac{\Lambda^2 - 4h^2}{2\lambda\Lambda}}, \quad Y_{ss} = \frac{\Gamma_b}{\Lambda} X_{ss}, \quad Z_{ss} = \frac{2h}{\Lambda}, \quad (2.7)$$

where $\Lambda = \lambda + (\lambda^2 - \Gamma_b^2)^{1/2}$. Note that at both (supercritical pitchfork) bifurcations a detailed stability analysis [15] shows that a unique steady state becomes unstable and two new stable steady states emerge. These semiclassical solutions, together with numerical solutions of the finite- N master Eq. (2.5), are plotted in Fig. 2.2 as a function of h/λ (note that $\langle J_x \rangle = \langle J_y \rangle = 0$ for the finite- N calculations). The plots indicate both a first- and second-order phase transition *as a single parameter, h , is varied*. The first-order (second-order) transition, at $h = h_-^c$ ($h = h_+^c$), involves a discontinuous (continuous) bifurcation in X_{ss} and associated behavior in Z_{ss} . Note that in the purely Hamiltonian system second-order transitions occur at $\pm h_+^c$, but the first-order transition has no counterpart (for $\lambda > 0$) and arises here due to a dissipative instability. The behavior we observe bears some relation to critical points found in cooperative resonance fluorescence (see, e.g., [13]).

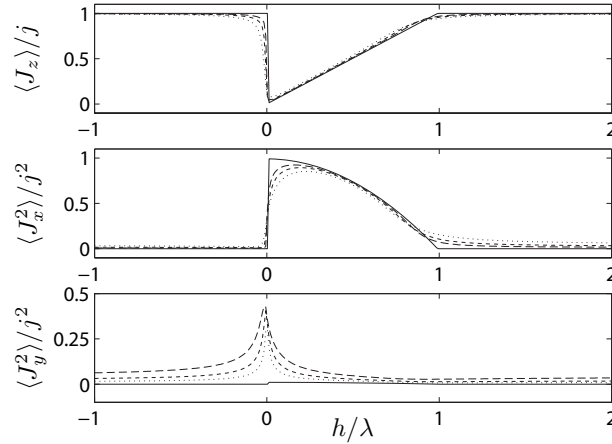


Figure 2.2. *Semiclassical (solid line) and finite- N steady-state inversion and second-order moments for $\Gamma_a/\lambda = 0.01$, $\Gamma_b/\lambda = 0.2$, and $N = 25$ (dotted line), 50 (short dashed line), 100 (long dashed line).*

In the large- N limit, quantum fluctuations can be included in the analysis as a first-order correction using a large- N expansion of the Holstein-Primakoff (HP) representation of angular momentum operators [14]. Applied in a coordinate system where the mean Bloch vector points along the positive z -axis, this takes the form $J_z = N/2 - c^\dagger c \simeq N/2$ and $J_+ = (N - c^\dagger c)^{1/2} c \simeq \sqrt{N} c$, where c (c^\dagger) is a bosonic annihilation (creation) operator. This linearization about the mean field state leads to a master equation of the general form

$$\dot{\rho} = -i[H_{\text{HP}}, \rho] + \Gamma_+ D[c^\dagger] \rho + \Gamma_- D[c] \rho + \{ \Upsilon (2c\rho c - c^2\rho - \rho c^2) + \text{H.c.} \}, \quad (2.8)$$

where H_{HP} is a quadratic in $\{c, c^\dagger\}$ and the coefficients are functions of $\{h, \lambda, \Gamma_a, \Gamma_b\}$ [15]. Equation(2.8) yields coupled, linear equations of motion for $\langle c \rangle$ and $\langle c^\dagger \rangle$, the eigenvalues of which display a sequence of bifurcations in both their real and imaginary parts as h is varied. The phase transitions are marked by the real part of one eigenvalue going to zero (i.e., critical slowing down) at $h = h_\pm^c$.

To examine this structure and dynamics, we consider the transmission of a (weak) probe laser field through the medium as a function of the probe frequency, i.e., we examine the frequency response of the system. A schematic of such a measurement setup is shown in Fig. 2.1(b). To compute the transmission spectrum we retain the two cavity modes in our model (i.e., we start from (2.2)), but again perform a linearization ($N \gg 1$) about the mean-field state. We consider the case in which the probe laser drives mode b , and the transmission spectrum $T_p(\nu_p)$ is defined as the coherent intensity, at probe frequency ν_p (in the rotating frame), in the output field from mode b .

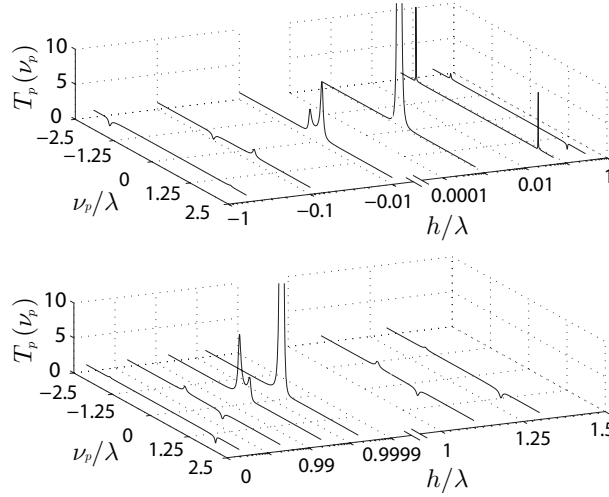


Figure 2.3. *Transmission spectra in the linearized regime, for $h/\lambda = \{-0.6, -0.1, -0.01, h_-^c/\lambda, 0.05, 0.3\}$ (top), and $\{0.5, 0.95, 0.995, h_+^c/\lambda, 1.1, 1.3\}$ (bottom), with microscopic parameters $\kappa_a/\delta_a = 0.02$, $\lambda_b/\lambda_a = 0.32$, $\kappa_b/\delta_a = 1$, $\delta_b = 0$, giving $\Gamma_a/\lambda = 0.01$, $\Gamma_b/\lambda = 0.05$. We set $\delta_{a,b}^- = 0$.*

In Fig. 2.3 we plot $T_p(\nu_p)$ (normalized by the maximum empty-cavity transmission) for a series of values of h around h_\pm^c . For the chosen parameters, the spectra consist of sharp “atomic” resonances superimposed on a much broader cavity mode resonance (i.e., $\kappa_b \gg \Gamma_b$). The locations and widths of the atomic resonances are determined by the imaginary and real parts of the above-mentioned eigenvalues, respectively. For $|h/\lambda| > 1$, the main atomic feature is a dip of width $2\Gamma_b$ at $\nu \simeq 2h$, corresponding to a cavity-mediated, collective spontaneous emission resonance. For $|h/\lambda| < 1$, spin-spin interactions play a more significant role and a pair of resonances at opposite frequencies feature in the spectrum. As $h \rightarrow h_\pm^c$ both from above and below these two features

merge continuously into a single peak, centered at $\nu_p = 0$, which ultimately diverges at $h = h_+^c$ in a pronounced signature of the second-order phase transition. The same merging and divergence is seen for the first-order transition, but only as $h \rightarrow h_-^c$ from below. For h very small (but $> h_-^c$), the spectrum consists of two sharp peaks of width $\sim \Gamma_b h / \lambda$ at $\nu_p \simeq \pm 2\lambda$. The transition is signaled by a discontinuous jump from this two-peaked spectrum to a single divergent peak at $\nu_p = 0$.

To analyze the entanglement properties of the system, we adopt a criterion for bipartite entanglement in collective spin systems which, for symmetric states, is both necessary and sufficient, and reads [16]

$$C_\varphi \equiv 1 - (4/N)\langle \Delta J_\varphi^2 \rangle - (4/N^2)\langle J_\varphi \rangle^2 > 0, \quad (2.9)$$

where $J_\varphi = \sin(\varphi)J_x + \cos(\varphi)J_y$. Here, we present numerical results for $C_R \equiv \max_\varphi C_\varphi$ (≥ 0), which, in fact, equals the rescaled concurrence $(N-1)C$, where C is the two-spin concurrence. In Fig. 2.4 we plot the steady-state value of C_R versus h/λ , computed from the linearized HP model and numerically from (2.5) for finite N . Both transitions are characterized by a sharp peak in the entanglement at the critical point [5–7], but they are distinguished by a discontinuity in C_R at $h = h_-^c$ (for $N \rightarrow \infty$) as opposed to a discontinuity in $\partial C_R / \partial h$ at $h = h_+^c$ [17]. The peaking of C_R at the critical points agrees with the conjecture of a general association between semiclassical bifurcations and maximal entanglement in dissipative, nonequilibrium many-body systems [18]. In the region where $C_R = 0$ the state approaches a mixture of maximally polarized states possessing large fluctuations (see Fig. 2.2). Note that, in the adiabatic regime considered, the cavity field operator $b(t) \propto J_+(t)$, and so collective spin correlations (and hence C_R) can be deduced from moments of the cavity output field, which may be measured by broadband homodyne detection.

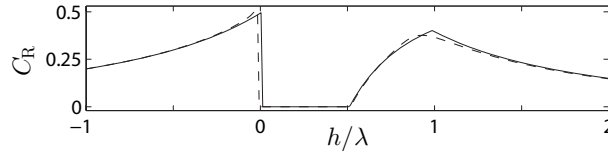


Figure 2.4. *Maximum entanglement C_R computed from the linearized HP ($N \rightarrow \infty$) model (solid) and from (2.5) for $N = 100$ (dashed), with $\Gamma_a/\lambda = 0.01$ and $\Gamma_b/\lambda = 0.2$.*

For an experimental realization, we have already mentioned ^6Li in a ring-cavity setup. A suitable system can also be designed using the ground states $|F = 1, m = \pm 1\rangle$ of ^{87}Rb and linearly-polarized cavity modes [15]. For specific parameter values, we consider recent experiments with cold atoms inside a high-finesse optical ring cavity [19], i.e., we take $g_{ij} \simeq 2\pi \cdot 100$ kHz and $\kappa_a \simeq 2\pi \cdot 25$ kHz. For $N \simeq 10^6$ atoms and a characteristic ratio $\Omega_{ij}/\Delta_i \simeq 0.0025$, we have $\lambda_a \simeq 2\pi \cdot 250$ kHz. With a Raman detuning $\delta_a \simeq 2\pi \cdot 2.5$ MHz, we then have $\lambda \simeq 2\lambda_a^2/\delta_a \simeq 2\pi \cdot 25$ kHz and $\Gamma_a \simeq \kappa_a(\lambda_a/\delta_a)^2 \simeq 2\pi \cdot 0.25$ kHz. Ground state magnetic level shifts of tens of MHz

would suffice to ensure distinct Raman channels. Mode b may be more strongly damped (i.e., the two cavity polarizations have different finesses), e.g., $\kappa_b \simeq 2\pi \cdot 250$ kHz, and, with $\lambda_b \simeq 2\pi \cdot 25$ kHz and $\delta_b \simeq 0$, we would then have $\Gamma_b \simeq \lambda_b^2/\kappa_b \simeq 2\pi \cdot 2.5$ kHz $\gg \Gamma_a$. Finally, the rate for single-atom spontaneous emission (neglected in our model) is estimated by $\Gamma_{\text{at}}\Omega_{ij}^2/(4\Delta_i^2) \lesssim 2\pi \cdot 0.01$ kHz $\ll \lambda, \Gamma_b$ for an atomic excited state decay rate $\Gamma_{\text{at}} = 2\pi \cdot 6$ MHz.

To conclude, we have proposed a feasible cavity QED system that is described by a dissipative LMG model and exhibits both first- and second-order nonequilibrium quantum phase transitions as a function of a single effective field parameter. Measurements on the cavity output light fields provide quantitative probes of the critical behavior. The system also offers opportunities for investigating phase transitions in response to variation of the strength of dissipation (i.e., Γ_b), for studying time-dependent behavior, such as entanglement dynamics, and for preparing very highly entangled states, which typically occur for short interaction times [15] and may in principle be “frozen” by switching off all optical fields.

The authors thank A. Daley and H. Carmichael for discussions and acknowledge support from the Austrian Science Foundation and from the Marsden Fund of the Royal Society of New Zealand.

Bibliography

- [1] I. Bloch, *Nature Phys.* **1**, 23 (2005).
- [2] A. Osterloh *et al.*, *Nature* **416**, 608 (2002).
- [3] T. J. Osborne and M. A. Nielsen, *Phys. Rev. A* **66**, 032110 (2002).
- [4] G. Vidal *et al.*, *Phys. Rev. Lett.* **90**, 227902 (2003).
- [5] J. Vidal, R. Mosseri, and J. Dukelsky, *Phys. Rev. A* **69**, 054101 (2004).
- [6] S. Dusuel and J. Vidal, *Phys. Rev. B* **71**, 224420 (2005)
- [7] J. Latorre *et al.*, *Phys. Rev. A* **71**, 064101 (2005).
- [8] R. G. Unanyan, C. Ionescu, and M. Fleischhauer, *Phys. Rev. A* **72**, 022326 (2005).
- [9] N. Lambert, C. Emary, and T. Brandes, *Phys. Rev. Lett.* **92**, 073602 (2004); *Phys. Rev. A* **71**, 053804 (2005).
- [10] J. Reslen, L. Quiroga, and N. F. Johnson, *Europhys. Lett.* **69**, 8 (2005).
- [11] H. J. Lipkin, N. Meshkov, and A. J. Glick, *Nucl. Phys.* **62**, 188 (1965).
- [12] F. Dimer *et al.*, *Phys. Rev. A* **75**, 013804 (2007).

- [13] R. Bonifacio and L. A. Lugiato, Opt. Commun. **19**, 172 (1976); P. D. Drummond and H. J. Carmichael, Opt. Commun. **27**, 160 (1978); H. J. Carmichael, J. Phys. B **13**, 3551 (1980).
- [14] T. Holstein and H. Primakoff, Phys. Rev. **58**, 1098 (1940).
- [15] S. Morrison and A. S. Parkins, arXiv:0711.2325
- [16] J. K. Korbicz, J. I. Cirac, and M. Lewenstein, Phys. Rev. Lett. **95**, 120502 (2005); *ibid.* **95**, 259901 (2005).
- [17] Note also that near h_+^c (h_-^c) the entanglement C_φ is maximized around $\varphi \simeq 0$ ($\varphi \simeq \pi/2$).
- [18] S. Schneider and G. J. Milburn, Phys. Rev. A **65**, 042107 (2002).
- [19] Ch. von Cube *et al.*, Fortschr. Phys. **54**, 726 (2006); J. Klinner *et. al*, Phys. Rev. Lett. **96**, 023002 (2006)

CHAPTER 3

PUBLICATION

Collective spin systems in dispersive optical cavity QED: Quantum phase transitions and entanglement

S. Morrison^{1,2,3} and A. S. Parkins³

1) Institute for Theoretical Physics, University of Innsbruck, Innsbruck A-6020, Austria

2) Institute for Quantum Optics and Quantum Information of the Austrian Academy of Sciences, A-6020 Innsbruck, Austria

3) Department of Physics, University of Auckland, Private Bag 92019, Auckland, New Zealand

We propose a cavity QED setup which implements a dissipative Lipkin-Meshkov-Glick model – an interacting collective spin system. By varying the external model parameters the system can be made to undergo both first- and second-order quantum phase transitions, which are signified by dramatic changes in cavity output field properties, such as the probe laser transmission spectrum. The steady state entanglement between pairs of atoms is shown to peak at the critical points and can be experimentally determined by suitable measurements on the cavity output field. The entanglement dynamics also exhibits pronounced variations in the vicinities of the phase transitions.

3.1 Introduction

The branch of atomic physics associated with ultracold atoms, ions, and molecules now provides a rich and exciting arena for investigations of strongly interacting, many-body quantum systems. Trapping and cooling techniques, coherent laser or microwave interactions, and applied magnetic fields enable exquisite control of both external (motional)

and internal (electronic) degrees of freedom of the particles, allowing one to “tailor” particle-particle interactions and thereby implement a broad range of systems that can be described accurately and transparently by idealized (but nontrivial) many-body Hamiltonians. An important example is the Hubbard model, realized with ultracold atoms in periodic optical lattices [1, 2], while realizations of other novel and significant lattice-spin models have been proposed, for example, with dipolar molecules in optical lattices [3] and with chains of trapped atomic ions [4]. The common, defining feature of these systems is the possibility for quantum critical phenomena, i.e., transitions between distinct quantum phases, in response to variations of an effective field or particle-particle interaction strength around some critical value.

The above-mentioned schemes generally provide many-body quantum systems that are subject to short-range (e.g., nearest-neighbor) interactions. Another interesting and commonly studied class of many-body systems are those possessing long-range, or even infinite-range, interactions, for which theoretical models typically allow exact solutions in the thermodynamic limit, or at least enable efficient numerical solution for large numbers of particles. A standard and classic example is the Lipkin-Meshkov-Glick (LMG) model [5], which was originally introduced in nuclear physics and is described by a Hamiltonian of the form

$$H_{\text{LMG}} = -2hJ_z - \frac{2\lambda}{N}(J_x^2 + \gamma J_y^2), \quad (3.1)$$

where $\{J_x, J_y, J_z\}$ are collective angular momentum operators for N spin-1/2 particles, h and λ are parameters giving the effective magnetic field and spin-spin interaction strengths, respectively, and $\gamma \in [-1, 1]$ is an anisotropy parameter. In this model, each spin interacts identically with every other spin and the nature of this interaction may be ferromagnetic ($\lambda > 0$) or antiferromagnetic ($\lambda < 0$). Significantly, the model exhibits critical behavior at zero temperature; in particular, either first- or second-order quantum phase transitions may occur (depending on the choice of λ and γ) as the ratio between λ and h is varied across a critical value.

This quantum critical behavior, combined with the relative simplicity of the model, has led to renewed theoretical interest in the LMG model from the point of view of studying entanglement properties of many-particle systems in relation to quantum phase transitions [6–8]. Bipartite entanglement measures characterizing entanglement between a pair of spins (e.g., the concurrence) or between two blocks of spins (e.g., the entanglement entropy) are relatively straightforward to compute for the LMG model and can display marked critical behavior and scaling at quantum critical points [9–15].

Given these interesting and very topical features of the LMG model, it follows that the physical realization of a system described accurately by such a model would provide a valuable test bed for studies of quantum critical phenomena and entanglement. However, the question naturally arises as to how realistic such an idealized model could be; the assumption of “infinite-range” interactions is obviously demanding and implies a very specialized system. Hamiltonians of the form (3.1) (with $\gamma = 0$) have appeared

recently in reduced two-mode models of atomic Bose-Einstein condensates undergoing tunnelling in double-well potentials or transitions between two internal atomic states [16, 17], and in models of a few trapped ions interacting with laser fields [18, 19], but emphasis in these works has been on unitary or adiabatic evolution from some initial atomic state to some final, prescribed (entangled) state, while flexibility of these systems with respect to parameters of the LMG model (i.e., λ , N , γ) appears limited.

Another possibility, furnished by the field of quantum optics, and for which long-range atom-atom interactions actually occur quite naturally, is cavity quantum electrodynamics (cavity QED) [20]. Here, one considers ensembles of atoms interacting, through an electronic transition, with a common electromagnetic field mode supported by an optical resonator. Through this common coupling, the field mode can effectively mediate interactions between atoms located at quite arbitrary and separate positions within the mode. So, in particular, the concept of an interaction “length” becomes redundant in this setting and a collective description of the atoms is appropriate.

In fact, that an ensemble of atoms coupled to a common field mode can be viewed as a many-body system of interacting spins was highlighted many years ago with the prediction of a thermal equilibrium phase transition in the celebrated Dicke model of N two-level atoms coupled to a single quantized field mode [21–25],

$$H = \omega a^\dagger a + \omega_0 J_z + \frac{\lambda}{\sqrt{N}}(a^\dagger + a)(J_+ + J_-), \quad (3.2)$$

where a is the annihilation operator for the field mode of frequency ω , ω_0 is the atomic transition frequency, and λ is the atom-field coupling strength (we set $\hbar = 1$). In particular, above a certain critical value of the coupling strength the system enters a so-called “superradiant” phase [26]. This phase transition persists at zero temperature [27, 28], with associated critical behavior of both the atom-field and atom-atom quantum entanglement [29–31]. The critical coupling strength at zero temperature is given by $\lambda_c = \sqrt{\omega\omega_0}/2$, which means that λ must be comparable to the field and/or atomic transition frequencies if the transition regime is to be reached. For atomic dipole transitions, this is typically not the case and, in fact, if it happened to be so, then the model (3.2) would be inadequate; in particular, the A^2 term [omitted from (3.2)] of the minimal coupling Hamiltonian should be included and doing so one actually finds that no phase transition exists [32].

However, a recent proposal for realizing the Dicke model quantum phase transition, based on Raman transitions between stable atomic ground states in an optical cavity QED setting [33], circumvents these issues by (i) implementing a system in which the relevant frequency and coupling scales are determined by light-induced frequency shifts and Raman transition rates, and (ii) utilizing an open-system dynamics (as opposed to a closed, Hamiltonian system) with input and output fields (i.e., external laser fields and cavity mode losses), thereby replacing a (fragile) thermal equilibrium phase transition with a (robust) dynamical, nonequilibrium phase transition. Furthermore, as shown in Ref. [33], the cavity output field offers a unique window on the system’s behavior and

properties, with, for example, fluorescence and quadrature-variance measurements providing dramatic signatures of criticality in the system, as well as quantitative measures of fluctuations and entanglement.

These features of the optical cavity QED system, combined with the observation that, in the dispersive limit $\omega \gg \{\omega_0, \lambda\}$, the cavity mode may be adiabatically eliminated and the Dicke Hamiltonian reduced to the form

$$H = \omega_0 J_z - \frac{4\lambda^2}{N\omega} J_x^2, \quad (3.3)$$

where $J_x = \frac{1}{2}(J_+ + J_-)$, motivate us to explore the possibilities for studying the LMG model in such a setting. In particular, by generalizing the configuration of Ref. [33] to two cavity field modes and operating in a dispersive regime (amounting to far-off-resonant Raman transitions), we find that it is possible to implement atomic spin systems that are described by the most general LMG model (3.1), and for which the Hamiltonian dynamics may still dominate over losses to the output cavity fields, thus enabling the clear realization of critical phenomena, including both first- and second-order dynamical quantum phase transitions. We find also that the cavity output fields can again be used to provide clear and detailed probes of properties of the atomic collective-spin system, including entanglement, in the critical regime.

We note that the present work bears some relation to studies of optical bistability and resonance fluorescence in cooperative atomic systems, which can also exhibit first- and second-order nonequilibrium phase transitions (see, for example, [34–38]). There, however, the dynamics explicitly includes (resonant) coherent driving of the atomic system by an external laser field (i.e., the Hamiltonian describing the system contains a driving term linear in J_x or J_y , rather than a direct spin-spin interaction term), and relatively little investigation has been made of the quantum entanglement associated with the critical behavior [39].

A more specific outline of our paper is as follows. In Sec. 3.2 we describe the microscopic model of atoms and light fields that realizes our effective spin system. In Sec. 3.3 we present some background to the LMG collective spin model and show how to engineer it using the general setup presented in Sec. 3.2. We conclude Sec. 3.3 with a brief overview of the methods of analysis to be used later in the paper. In Sec. 3.4 we describe a more specific, potential physical implementation of the system we have proposed, based on alkali metal atoms confined within a high-finesse ring cavity. In Sec. 3.5 we focus on the $\gamma = 0$ LMG model and focus on the second-order transition; we first present a linearized analysis of the system in the thermodynamic limit using the Holstein-Primakoff representation of spin operators. Using the input-output theory of quantum optics we relate the internal spin properties to the measurable cavity output field and determine the probe transmission spectrum as an example. The second part of Sec. 3.5 is concerned with the presence and behavior of atom-atom (or spin-spin) entanglement in the system, particularly across the quantum phase transition (QPT). We present results for both the steady-state entanglement and the entanglement dynamics,

using either exact numerical solutions for finite system size or analytical solutions in the thermodynamic limit. In Sec. 3.6 we essentially repeat the analysis of the previous section, but focus on a parameter regime where a first-order phase transition occurs in the $\gamma = 0$ LMG model as the effective magnetic field parameter, h , is varied. Finally, in Sec. 3.7 we conclude and briefly discuss possible extensions of the current work.

3.2 Theoretical Model

We consider a collection of N atoms coupled via electric dipole transitions to (at most) four laser fields and to a pair of orthogonally polarized optical cavity modes. The atomic level and excitation scheme is shown in Fig. 3.1. In particular, the atoms are assumed to possess two stable electronic ground states, labelled $|0\rangle$ and $|1\rangle$, at energies $(\hbar = 1) \omega_0 = 0$ and ω_1 , respectively. The laser and cavity fields combine to drive Raman transitions between $|0\rangle$ and $|1\rangle$, via the excited atomic states $|r\rangle$ and $|s\rangle$ (energies ω_r and ω_s , respectively). Specifically, the laser fields, at frequencies ω_{r0} , ω_{s0} , ω_{r1} , and ω_{s1} , couple to the dipole transitions $|0\rangle \leftrightarrow |r\rangle$, $|0\rangle \leftrightarrow |s\rangle$, $|1\rangle \leftrightarrow |r\rangle$, $|1\rangle \leftrightarrow |s\rangle$ with Rabi frequencies Ω_{r0} , Ω_{s0} , Ω_{r1} , and Ω_{s1} , respectively. Cavity field a , at frequency ω_a , couples to the transitions $|0\rangle \leftrightarrow |r\rangle$ and $|1\rangle \leftrightarrow |s\rangle$ with coupling strengths g_{r0} and g_{s1} , respectively, while cavity field b , at frequency ω_b , couples to the transitions $|0\rangle \leftrightarrow |s\rangle$ and $|1\rangle \leftrightarrow |r\rangle$ with coupling strengths g_{s0} and g_{r1} , respectively. All of the fields will be assumed to be far-off resonance with the electric dipole transitions to which they couple, meaning that the atomic states $|r\rangle$ and $|s\rangle$ are only virtually excited and can be eliminated from the dynamics. Finally, at the location of the atoms, the cavity and laser fields are taken to be travelling waves copropagating in the x direction, with sufficiently broad beam waists so as to ensure a homogeneous atom-field coupling.

3.2.1 Adiabatic elimination of atomic excited states

To facilitate adiabatic elimination of the atomic excited states we move to a rotating frame according to the unitary transformation $U(t) = e^{-iH_0 t}$, with

$$H_0 = (\omega_{s0} - \omega'_1) a^\dagger a + (\omega_{r0} - \omega'_1) b^\dagger b + \sum_{j=1}^N (\omega_{s0} |s_j\rangle\langle s_j| + \omega_{r0} |r_j\rangle\langle r_j| + \omega'_1 |1_j\rangle\langle 1_j|), \quad (3.4)$$

where ω'_1 is a frequency close (or possibly equal) to ω_1 . Next, as mentioned above, we assume large detunings of the light fields from the atomic excited states, i.e., we assume that $\Delta_r = \omega_r - \omega_{r0}$ and $\Delta_s = \omega_s - \omega_{s0}$ are much larger in magnitude than any other rates characterizing the system. This allows the atomic excited states to be adiabatically eliminated and also enables us to neglect the effects of atomic spontaneous emission.

Additionally, as depicted in Fig. 3.1, we assume that only four distinct Raman transitions are of significance (i.e., resonant or roughly resonant); in particular, in our

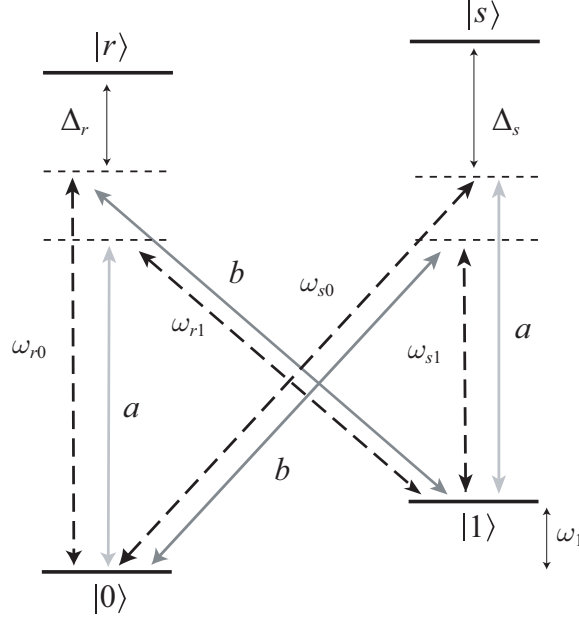


Figure 3.1. *Atomic level and excitation scheme for the general model.*

model we retain only those Raman processes that cause a change in the electronic state of the atoms ($|0\rangle \rightarrow |1\rangle$ or $|1\rangle \rightarrow |0\rangle$) and also involve transfer of a photon from a laser field into a cavity mode or vice versa. All other possible Raman processes are assumed to be far-off resonant and therefore negligible. Quantitatively, this requires, for example, that $|\omega_{r0} - \omega_a|$ and $|\omega_{r0} - (\omega_{r1} + \omega_1)|$ are sufficiently large, with, in particular, $|\omega_{r0} - \omega_a|, |\omega_{r0} - (\omega_{r1} + \omega_1)| \gg |\omega_a - (\omega_{r1} + \omega_1)|, |\omega_{r0} - (\omega_b + \omega_1)|$.

Retaining only the four dominant Raman processes simplifies the model considerably, and with a choice of laser frequencies such that $\omega_{s0} - \omega_{r1} = \omega_{r0} - \omega_{s1} = 2\omega'_1$ we are able to remove all explicit time dependence from the Hamiltonian describing our system. Employing the collective spin operators,

$$J_z = \frac{1}{2} \sum_{j=1}^N (|1_j\rangle\langle 1_j| - |0_j\rangle\langle 0_j|), \quad J_+ = \sum_{j=1}^N |1_j\rangle\langle 0_j|, \quad J_- = \sum_{j=1}^N |0_j\rangle\langle 1_j|, \quad (3.5)$$

and omitting constant energy terms, our effective Hamiltonian for the collective atomic system and cavity modes can be written in the form

$$\begin{aligned} H_g = & \omega_0 J_z + \delta_a a^\dagger a + \delta_b b^\dagger b + 2\delta_a^- J_z a^\dagger a + 2\delta_b^- J_z b^\dagger b \\ & + \frac{\lambda_a}{\sqrt{N}} (X_a a + X_a^\dagger a^\dagger) + \frac{\lambda_b}{\sqrt{N}} (X_b b + X_b^\dagger b^\dagger), \end{aligned} \quad (3.6)$$

where $X_i = \alpha_i J_+ + \beta_i J_-$ and the effective parameters are given in terms of the micro-

scopic parameters by

$$\omega_0 = \frac{1}{4} \left(\frac{|\Omega_{r1}|^2}{\Delta_r} + \frac{|\Omega_{s1}|^2}{\Delta_s} - \frac{|\Omega_{r0}|^2}{\Delta_r} - \frac{|\Omega_{s0}|^2}{\Delta_s} \right) + \omega_1 - \omega'_1, \quad (3.7a)$$

$$\delta_a = \omega_a - \omega_{s0} + \omega'_1 + N\delta_a^+, \quad (3.7b)$$

$$\delta_b = \omega_b - \omega_{r0} + \omega'_1 + N\delta_b^+, \quad (3.7c)$$

$$\delta_a^\pm = \frac{1}{2} \left(\frac{|g_{s1}|^2}{\Delta_s} \pm \frac{|g_{r0}|^2}{\Delta_r} \right), \quad (3.7d)$$

$$\delta_b^\pm = \frac{1}{2} \left(\frac{|g_{r1}|^2}{\Delta_r} \pm \frac{|g_{s0}|^2}{\Delta_s} \right), \quad (3.7e)$$

$$\lambda_a \alpha_a = \frac{\sqrt{N} \Omega_{r1}^* g_{r0}}{2\Delta_r}, \quad \lambda_a \beta_a = \frac{\sqrt{N} \Omega_{s0}^* g_{s1}}{2\Delta_s}, \quad (3.7f)$$

$$\lambda_b \alpha_b = \frac{\sqrt{N} \Omega_{s1}^* g_{s0}}{2\Delta_s}, \quad \lambda_b \beta_b = \frac{\sqrt{N} \Omega_{r0}^* g_{r1}}{2\Delta_r}. \quad (3.7g)$$

Note that the (dimensionless) factors $\{\alpha_{a,b}, \beta_{a,b}\} \in [-1, 1]$ have been introduced for convenience. Note also that for a characteristic level scheme as shown in Fig. 3.1, one might typically expect that $g_{s1} = g_{r0}$ and $g_{r1} = g_{s0}$, so assuming $\Delta_s \approx \Delta_r$ we would therefore also expect that $|\delta_{a,b}^-| \ll |\delta_{a,b}^+|$.

In summary, the master equation for the reduced density operator, ρ_g (i.e., with the atomic excited states eliminated and spontaneous emission neglected), is given by

$$\dot{\rho}_g = -i[H_g, \rho_g] + \kappa_a D[a]\rho_g + \kappa_b D[b]\rho_g, \quad (3.8)$$

where $D[A]\rho = 2A\rho A^\dagger - A^\dagger A\rho - \rho A^\dagger A$ and κ_i is the cavity field decay rate.

3.2.2 Adiabatic elimination of the cavity modes

We now consider the limit $\sqrt{\kappa_i^2 + \delta_i^2} \gg \lambda_a, \lambda_b, \omega_0$. In this limit, the cavity modes are only ever weakly or virtually excited and may also be adiabatically eliminated from the dynamics. Following the standard adiabatic elimination procedure [40], we derive the following master equation for the reduced density operator, ρ , of the collective atomic system alone:

$$\dot{\rho} = -i[H, \rho] + \Gamma_a D[X_a^\dagger]\rho + \Gamma_b D[X_b^\dagger]\rho, \quad (3.9)$$

with

$$H = \omega_0 J_z - \frac{\Lambda_a}{N} X_a X_a^\dagger - \frac{\Lambda_b}{N} X_b X_b^\dagger, \quad (3.10)$$

where the effective spin-spin interaction strengths and collective atomic dissipative rates are ($i \in \{a, b\}$)

$$\Lambda_i = \frac{\lambda_i^2 \delta_i}{\kappa_i^2 + \delta_i^2}, \quad (3.11a)$$

$$\Gamma_i = \frac{\lambda_i^2 \kappa_i}{\kappa_i^2 + \delta_i^2}. \quad (3.11b)$$

Note that both dispersive nonlinear terms [terms proportional to δ_a^- and δ_b^- in Eq. (3.6)] do not contribute in the adiabatic approximation since in this limit we assume a vacuum state for both cavity modes.

3.2.3 Cavity output fields and measurement

Taking a brief step backwards now to the atom-cavity Hamiltonian (3.6), and using the input-output theory of open quantum optical systems [40, 41], we can derive quantum Langevin equations for the cavity mode operators; in particular, for the mode b , we have (neglecting the term proportional to δ_b^-)

$$\dot{b} = -(\kappa_b + i\delta_b)b - i\lambda_b \frac{X_b^\dagger}{\sqrt{N}} + \sqrt{2\kappa_b} b_{\text{in}}(t), \quad (3.12)$$

where $b_{\text{in}}(t)$ describes the quantum noise input to the cavity mode (see Fig. 3.2) and satisfies the commutation relation $[b_{\text{in}}(t), b_{\text{in}}^\dagger(t')] = \delta(t - t')$. Equation (3.12) illustrates the linear relationship between the cavity operator and atomic operator X_b^\dagger . The adiabatic limit of the preceding subsection amounts, in the present context, to the assumption that $X_b(t)$ varies on a much slower time scale than $b(t)$ [and $b_{\text{in}}(t)$], so that we can write

$$b(t) \simeq -i \frac{\lambda_b}{\kappa_b + i\delta_b} \frac{X_b^\dagger(t)}{\sqrt{N}} + \frac{\sqrt{2\kappa_b}}{\kappa_b + i\delta_b} b_{\text{in}}(t). \quad (3.13)$$

The cavity output field is given by $b_{\text{out}}(t) = \sqrt{2\kappa_b} b(t) - b_{\text{in}}(t)$, so we in turn obtain a direct relationship between the dynamics of the (internal) collective atomic spin and the (external) cavity output field. Hence, spin-spin correlations of the form $\langle X_b X_b \rangle / N$ and $\langle X_b^\dagger X_b \rangle / N$ could be deduced from correlations of the cavity output field, which may be measured, for example, by performing broadband homodyne detection on the emitted light [42].

3.3 Collective (LMG) Spin Models

The LMG model, originally introduced in nuclear physics to model collective motion in nuclei [5], describes N interacting fermions distributed on two N -fold degenerate levels (denoted by \pm) separated by an energy δ . Denoting the fermion annihilation operator by $c_{j,\sigma}$, where $j \in \{1, \dots, N\}$ and $\sigma \in \{+, -\}$, the Hamiltonian for this system may be written as

$$H' = \frac{\delta}{2} \sum_{j,\sigma} \sigma c_{j,\sigma}^\dagger c_{j,\sigma} + \frac{V}{2} \sum_{j,j',\sigma} c_{j,\sigma}^\dagger c_{j',\sigma}^\dagger c_{j,-\sigma} c_{j',-\sigma} + \frac{W}{2} \sum_{j,j',\sigma} c_{j,\sigma}^\dagger c_{j',-\sigma}^\dagger c_{j,-\sigma} c_{j',\sigma}. \quad (3.14)$$

Introducing the collective spin operators, $J_z = \frac{1}{2} \sum_{j,\sigma} \sigma c_{j,\sigma}^\dagger c_{j,\sigma}$ and $J_\pm = \sum_j c_{j,\pm}^\dagger c_{j,\mp}$ allows us to reexpress the Hamiltonian as

$$H' = \delta J_z + \frac{V}{2}(J_+^2 + J_-^2) + \frac{W}{2}(J_+ J_- + J_- J_+). \quad (3.15)$$

This Hamiltonian commutes with \mathbf{J}^2 , thus conserving the total angular momentum, and with $e^{i\pi J_z}$, corresponding to a parity (spin-flip) symmetry [9]. It is straightforward to rewrite this Hamiltonian in terms of J_x and J_y , defined via $J_\pm = J_x \pm iJ_y$, giving the generalized LMG model,

$$H_{\text{LMG}} = -2hJ_z - \frac{2\lambda}{N}(J_x^2 + \gamma J_y^2), \quad (3.16)$$

where $\lambda = -(V + W)N/2$, $\gamma = (W - V)/(V + W)$ (we will only consider $\gamma \in [-1, 1]$), and $h = -\delta/2$.

This model is well known for its second-order symmetry breaking phase transition in the ferromagnetic regime ($\lambda > 0$) [13]. For small interaction strength the system is in the normal phase, where the ground state is unique and polarized in the direction of the magnetic field. As the interaction is increased above a critical value, λ_c , the system enters the broken phase, where the ground state becomes doubly degenerate and macroscopically displaced from its original configuration, thus breaking the parity symmetry. For the special case $\gamma = 1$ the Hamiltonian also commutes with J_z , thus enabling a direct analytic solution. All other cases $\gamma \neq 1$ lie in a separate universality class. In the antiferromagnetic regime, $\lambda < 0$, the model exhibits a first-order phase transition as the effective magnetic field h crosses $h_c = 0$ (provided $\gamma > 0$).

Using the setup described in the previous section we can implement the generalized LMG model for any γ by making appropriate choices of $\alpha_a, \beta_a, \alpha_b, \beta_b$ in the Hamiltonian (3.10). We now consider three specific cases of general interest.

3.3.1 Conventional $\gamma = -1$ LMG model

The $\gamma = -1$ LMG Hamiltonian may be implemented by choosing $\alpha_a = \alpha_b = \alpha$ and $\beta_a = -\beta_b = \beta$ (corresponding to $X_a = \alpha J_+ + \beta J_-$ and $X_b = \alpha J_+ - \beta J_-$), and setting $\Lambda_a = -\Lambda_b$ (note that the signs of $\Lambda_{a,b}$ are determined by the signs of the detunings $\delta_{a,b}$), so that

$$H = -2hJ_z - \frac{2\lambda}{N}(J_x^2 - J_y^2), \quad (3.17)$$

with $h = -\omega_0/2$ and $\lambda = 2\alpha\beta\Lambda_a$. This instance of the LMG model has been most widely studied for its phase transition properties. For the dissipative terms we assume, for simplicity, that $2\Gamma_a = 2\Gamma_b \equiv \Gamma$, so that the full master equation reduces to the form

$$\dot{\rho} = -i[H, \rho] + \frac{\Gamma_+}{N}D[J_+]\rho + \frac{\Gamma_-}{N}D[J_-]\rho, \quad (3.18)$$

where $\Gamma_+ = \Gamma\alpha^2$ and $\Gamma_- = \Gamma\beta^2$. The Hamiltonian dynamics can be expected to play a dominant role if $\delta_{a,b} \gg \kappa_{a,b}$ (which corresponds to $|\Lambda_{a,b}| \gg \Gamma_{a,b}$).

3.3.2 Isotropic $\gamma = 1$ LMG model

The isotropic $\gamma = 1$ LMG Hamiltonian may be obtained, for example, by choosing $\alpha_a = \beta_b = 1$ and $\alpha_b = \beta_a = 0$ (corresponding to $X_a = J_+$ and $X_b = J_-$), and setting $\Lambda_a = \Lambda_b \equiv \lambda$, which gives

$$H = -2hJ_z - \frac{2\lambda}{N}(J_x^2 + J_y^2), \quad (3.19)$$

where $h = -\omega_0/2$. The full master equation is

$$\dot{\rho} = -i[H, \rho] + \frac{\Gamma_a}{N}D[J_-]\rho + \frac{\Gamma_b}{N}D[J_+]\rho. \quad (3.20)$$

3.3.3 Simple $\gamma = 0$ LMG model

The $\gamma = 0$ LMG Hamiltonian, which will be focus of our attention in this paper, may be obtained by choosing $\alpha_a = \beta_a = \alpha$ (corresponding to $X_a = 2\alpha J_x$), and setting $\delta_b = 0$ (so that $\Lambda_b = 0$). This gives

$$H = -2hJ_z - \frac{2\lambda}{N}J_x^2, \quad (3.21)$$

where $\lambda = 2\alpha^2\Lambda_a$. While the Raman channels involving the cavity mode b could be omitted completely, here we retain one of them (for reasons to be discussed below), with the choice $\beta_b = \beta$, and $\alpha_b = 0$, corresponding to $X_b = \beta J_-$. Hence, the full master equation we consider is

$$\dot{\rho} = -i[H, \rho] + \frac{\Gamma_a}{N}D[2J_x]\rho + \frac{\Gamma_b}{N}D[J_+]\rho, \quad (3.22)$$

where the factor β^2 has been absorbed into Γ_b .

If we now consider the case where $|\Lambda_a| \gg \Gamma_a$ and $\Gamma_b \gg \Gamma_a$, then the role played by each cavity mode in relation to the atomic system is quite distinct. Specifically, cavity mode a mediates the collective spin-spin interaction required for the Hamiltonian dynamics (with coupling strength $\Lambda_a \simeq \lambda_a^2/\delta_a$), while cavity mode b effectively mediates the collective atomic decay (with rate $\Gamma_b = \lambda_b^2/\kappa_b$). Importantly, we note that $X_b = J_+$ implies a quite direct relationship between moments of the cavity mode operators b and b^\dagger and moments of the collective atomic spin operators J_\pm ; in particular, measurements of the output light field from cavity mode b will provide, rather directly and transparently, characteristic properties of the collective atomic spin.

In contrast, for the $\gamma = -1$ model the two cavity modes mediate the collective spin-spin interaction on an equal footing, i.e., $|\Lambda_a| = |\Lambda_b|$, while the operators X_a and X_b are linear combinations of J_+ and J_- , which leads to a somewhat less transparent (i.e, arguably less convenient) relationship between correlations of the cavity output fields

and atomic spin-spin correlations. Partially for this reason, we focus in this paper on the $\gamma = 0$ model, with a clear distinction between the effective roles of the two cavity modes and a potentially better suitability for measurements of the collective atomic spin properties.

3.3.4 Methods of analysis

To analyze the atomic-spin master equations presented in the preceding sections, we make use of both numerical and analytical techniques. For finite spin $j = N/2$, the master equations can be solved numerically for quite large N [43], owing to the linear scaling of the Hilbert space dimension, d , with the system size, i.e., $d = N + 1$. In what follows, we will typically present results of numerical simulations for $N \lesssim 100$.

For very large system sizes, $N \gg 1$, it is possible to linearize the quantum fluctuations around the mean spin state (i.e., around the “Bloch vector”). First we find this mean spin state by calculating the steady-state solutions of the semiclassical equations of motion for the components of the Bloch vector. After a suitable rotation (determined by the mean state) of the spin coordinate system, we use the Holstein-Primakoff (HP) representation of angular momentum operators [44, 45], which enables a systematic large- N expansion of the master equation, to which we then apply the limit $N \rightarrow \infty$. While all of the results obtained in the linearized regime are exact analytical results, in many cases the expressions obtained are too lengthy to give any useful information; in these cases we simply plot the relevant quantities.

3.4 Potential Experimental Implementation

For a possible experimental implementation of our scheme, we consider, as mentioned previously, an ensemble of atoms confined inside a high finesse ring cavity that supports two travelling-wave modes, a and b . The required laser fields, which are assumed to be at frequencies that are not supported by the resonator, are injected through one of the resonator mirrors so as to be copropagating with the cavity fields through the ensemble.

If we take ^6Li as the atomic species, then the atomic level scheme of Fig. 3.1 can be implemented directly with the two ground magnetic substates $|F = 1/2, m = \pm 1/2\rangle$ as $|0\rangle$ and $|1\rangle$, and with a magnetic field applied perpendicular to the cavity axis to provide a frequency splitting $2\omega_B$ between these two states. The modes a and b would be orthogonal, linearly polarized cavity modes, with, in particular, mode a polarized along the direction of the magnetic field. (Note that if the two modes happen to be very different in frequency due, for example, to birefringence in the cavity mirrors, then the magnetic field may not be necessary.)

Another possibility, illustrated in Fig. 3.2, might be a configuration based on the $F = 1 \leftrightarrow F' = 0$ transition of ^{87}Rb , in which the states $|0\rangle$ and $|1\rangle$ are the ground magnetic substates $|F = 1, m = \pm 1\rangle$, with frequency splitting $2\omega_B$ due to a magnetic field applied along the cavity axis. The modes a and b would be orthogonal, linearly polarized cavity modes, polarized perpendicular to the magnetic field. Note, however, that the modes would need to be sufficiently different in frequency (which could be imposed, for example, by cavity birefringence) in order that the Raman channels involving different modes are distinct.

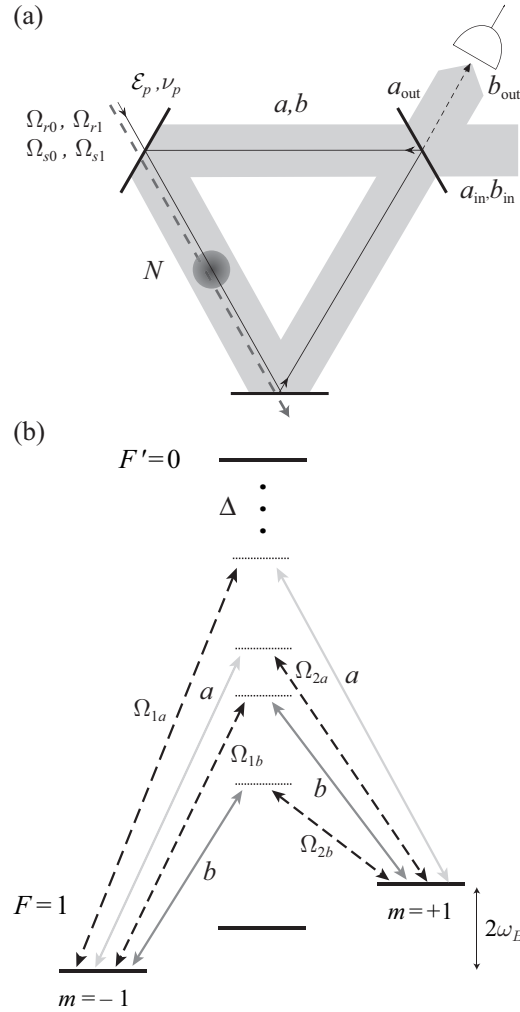


Figure 3.2. (a) Schematic of potential ring cavity system and setup for measurement of the output transmission spectrum of a weak probe laser field of amplitude \mathcal{E}_p and frequency ν_p . (b) Possible atomic level scheme as described in the text.

Alternatively, the modes a and b could be two entirely different (linearly polarized) longitudinal modes of the resonator, one quasis resonant with the $F = 1 \leftrightarrow F' = 0$ transition of the D2 line and the other quasis resonant with the $F = 1 \leftrightarrow F' = 1$ transition of the D1 line.

For specific parameter values, we consider experimental systems such as those realized recently in Ref. [46, 47], where cold atoms are held inside a high-finesse optical ring cavity. In particular, let us assume a single-atom–single-photon dipole coupling strength of $g/(2\pi) \simeq 100$ kHz and a cavity field decay rate of $\kappa_a/(2\pi) \simeq 25$ kHz. For $N \simeq 10^6$ atoms and a characteristic laser-Rabi-frequency-to-detuning ratio of $\Omega/\Delta \simeq 0.005$, we have $\lambda_a/(2\pi) \simeq 250$ kHz ($\alpha_a = 1$). If we assume a Raman detuning $\delta_a/(2\pi) \simeq 2.5$ MHz $\gg \lambda_a/(2\pi), \kappa_a/(2\pi)$, we then have, for example, $\Lambda_a \simeq \lambda_a^2/\delta_a \simeq 2\pi \times 25$ kHz and $\Gamma_a \simeq \Lambda_a(\kappa_a/\delta_a) \simeq 2\pi \times 0.25$ kHz. This illustrates that it should be possible to achieve a regime where the (coherent) Hamiltonian dynamics is dominant over the effective dissipation. Note also that, for these parameters, readily achievable ground state magnetic level shifts ($2\omega_B$) of tens of MHz would suffice to ensure distinct Raman channels.

The same parameter regime could obviously be chosen for cavity mode b , but if we consider the $\gamma = 0$ model as discussed in Sec. 3.3.3, then we might, for example, assume mode b to be more strongly damped (i.e., the two cavity polarizations have different finesses), e.g., $\kappa_b/(2\pi) \simeq 250$ kHz, and, with smaller Raman transition rate $\lambda_b/(2\pi) \simeq 25$ kHz and detuning $\delta_b/(2\pi) \simeq 0$, we would then have $\Gamma_b \simeq \lambda_b^2/\kappa_b \simeq 2\pi \times 2.5$ kHz $\gg \Gamma_a$. Given these considerations, in the next section, where we examine the second-order transition of the $\gamma = 0$ model, we will typically employ the set of normalized parameters $\{h = 1, \Gamma_a = 0.01, \Gamma_b = 0.2\}$, which give a critical coupling strength $\lambda_c \simeq 1$.

Finally, we note that the rate for single-atom spontaneous emission (neglected in our model) is estimated by $\Gamma_{\text{sp}}\Omega^2/(4\Delta^2) \lesssim 2\pi \times 0.04$ kHz $\ll \Lambda_a, \Gamma_{a,b}$, where an atomic excited state linewidth of $\Gamma_{\text{sp}}/(2\pi) = 6$ MHz has been assumed.

3.5 Second-Order Phase Transition

We focus first on the positive field case ($h > 0$) of the $\gamma = 0$ LMG model with ferromagnetic interactions ($\lambda > 0$), for which a second-order phase transition occurs as the magnitude of the interaction strength is varied [48]. This transition will turn out to be similar to the one recently studied in the dissipative Dicke model with resonant atom-cavity interactions (as considered in Ref. [33]). However, it should be noted that in the Dicke model the cavity field plays an intrinsic role in the dynamics and associated critical behavior, unlike in our present model where it has been adiabatically eliminated. Consequently atom-field entanglement is effectively negligible in the present context, while atom-atom entanglement is significant and will be the focus of our study.

In Sec. 3.5.1 we consider the spin master equation in a linearized regime, appropriate for $N \gg 1$, and determine the transmission spectrum of a weak probe laser. Spin-spin entanglement is studied in Sec. 3.5.2 both in the thermodynamic limit and for finite N ; specifically the behavior of the steady-state entanglement, as well as entanglement dynamics, is examined in the vicinity of the quantum phase transition.

3.5.1 Linearized model

In this section we study the master equation model (3.22) in the thermodynamic limit by linearizing the quantum fluctuations around the mean-field state. Note that the atom-cavity coupling strengths appearing in the effective coupling constants (3.7f) and (3.7g) scale as $1/\sqrt{V}$, where V is the cavity mode volume. The thermodynamic limit corresponds to $N \rightarrow \infty$ and $V \rightarrow \infty$ with $\varrho = N/V$, the atomic density in the cavity, constant. Since the thermodynamic limit does not alter the effective coupling strengths, which scale as $\sqrt{\varrho}$, we will henceforth refer to the thermodynamic limit as $N \rightarrow \infty$ [28].

Firstly, we present the semiclassical analysis which determines the mean-field state relevant for $N \gg 1$. We then expand the angular momentum operators around the semiclassical steady state using the Holstein-Primakoff representation, thus obtaining a linearized version of the master equation, the eigenvalues of which are subsequently analyzed. Finally, we calculate, for the linearized model, the transmitted amplitude of a weak probe laser through the atom-cavity system as a function of the probe frequency, i.e., the probe transmission spectrum. This physically measurable quantity probes the energy, or eigenvalue, structure of the system and, as we will see, provides clear signatures of the dynamical quantum phase transition.

Semiclassical equations of motion and steady-state solutions

The equations of motion for the expectation values of the spin components of the Bloch vector, $\langle J_x \rangle$, $\langle J_y \rangle$, and $\langle J_z \rangle$, are readily derived from the master equation (3.22), but do not form a closed set of equations. However, by factorizing all terms $\langle J_k J_l \rangle \rightarrow \langle J_k \rangle \langle J_l \rangle$ with $k, l \in \{x, y, z\}$, which corresponds to neglecting quantum fluctuations, we obtain a closed set of equations, which we call the semiclassical equations of motion from hereon. Introducing the notation $X = \langle J_x \rangle/j$, $Y = \langle J_y \rangle/j$, $Z = \langle J_z \rangle/j$, where $j = N/2$, the semiclassical equations of motion are found to be

$$\dot{X} = 2hY - \Gamma_b ZX, \quad (3.23a)$$

$$\dot{Y} = -2hX + 2\lambda ZX - \Gamma_b ZY, \quad (3.23b)$$

$$\dot{Z} = -2\lambda XY + \Gamma_b(X^2 + Y^2), \quad (3.23c)$$

with the constraint $X^2 + Y^2 + Z^2 = 1$ corresponding to conservation of angular momentum.

The steady-state solutions of these equations of motion exhibit a bifurcation at a critical coupling strength

$$\lambda_c \equiv h + \frac{\Gamma_b^2}{4h} \quad (3.24)$$

(note $\lambda_c > \{h, \Gamma_b\}$ for $\Gamma_b \neq 2h$). For $\lambda < \lambda_c$ the stable steady-state solutions are

$$Z_{ss} = 1, \quad X_{ss} = Y_{ss} = 0, \quad (3.25)$$

while for $\lambda > \lambda_c$ they become

$$Z_{ss} = \frac{2h}{\Lambda}, \quad (3.26a)$$

$$X_{ss} = \pm \sqrt{\frac{\Lambda^2 - 4h^2}{2\lambda\Lambda}}, \quad (3.26b)$$

$$Y_{ss} = \frac{\Gamma_b}{2h} X_{ss} Z_{ss}, \quad (3.26c)$$

where

$$\Lambda = \lambda + \sqrt{\lambda^2 - \Gamma_b^2}. \quad (3.27)$$

The bifurcation at λ_c is illustrated in Fig. 3.3, where, to facilitate a comparison between semiclassical and finite- N solutions (computed from numerical solution of the master equation), we plot the second-order moments $\langle J_x^2 \rangle$, $\langle J_y^2 \rangle$, and $\langle J_z^2 \rangle$ (since the finite- N master equation gives $\langle J_x \rangle = \langle J_y \rangle = 0$ for all λ). We note that the two approaches are already in reasonable agreement for $N \simeq 50$.

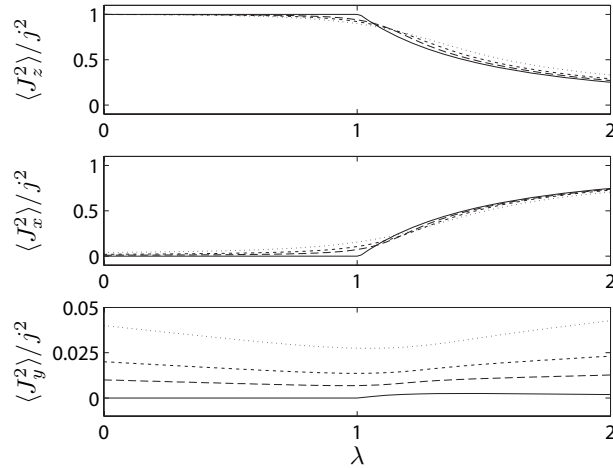


Figure 3.3. Semiclassical (solid line) and finite- N steady-state second-order moments for $h = 1$, $\Gamma_a = 0.01$, $\Gamma_b = 0.2$, and $N = 25$ (dotted), 50 (short dashed line), 100 (long dashed line).

Holstein-Primakoff representation

The quantum fluctuations that are neglected in the semiclassical analysis can be included in the limit $N \gg 1$ as a first-order correction. This is achieved by using the Holstein-Primakoff (HP) representation of the angular momentum operators [44, 45], which in the present context takes the form

$$J_z = \frac{N}{2} - c^\dagger c, \quad (3.28a)$$

$$J_+ = \sqrt{N} \sqrt{1 - \frac{c^\dagger c}{N}} c, \quad (3.28b)$$

$$J_- = \sqrt{N} c^\dagger \sqrt{1 - \frac{c^\dagger c}{N}}, \quad (3.28c)$$

where c and c^\dagger are bosonic annihilation and creation operators, respectively, satisfying $[c, c^\dagger] = 1$. In particular, if $N \gg 1$ and $\langle J_z \rangle \approx N/2$, i.e., $\langle c^\dagger c \rangle \ll N/2$ (so that the Bloch vector points essentially along the z axis), then the HP representation of J_+ and J_- can be reduced to $J_+ \simeq \sqrt{N} c$ and $J_- \simeq \sqrt{N} c^\dagger$, effectively linearizing the dynamics.

In the normal phase ($\lambda < \lambda_c$), this approach can be applied immediately since the steady-state solutions $X_{ss} = Y_{ss} = 0$. However, in the broken phase ($\lambda > \lambda_c$), the steady-state solutions $X_{ss}, Y_{ss} \neq 0$, i.e., the Bloch vector is rotated away from the z axis, and the HP representation is most conveniently applied with respect to the new orientation of the Bloch vector. We do this by first rewriting the semiclassical steady-state solutions in terms of spherical coordinates θ and ϕ as $Z_{ss} = \cos \theta$, $X_{ss} = \sin \theta \cos \phi$, and $Y_{ss} = \sin \theta \sin \phi$, and then applying a unitary rotation $R = \exp(i\hat{\mathbf{u}} \cdot \mathbf{J}\theta)$ around an axis $\hat{\mathbf{u}} = (-\sin \phi, \cos \phi, 0)$, so that the transformed operators $J'_l = R^\dagger J_l R$ describe quantum fluctuations around the semiclassical steady state. The HP representation (3.28a)-(3.28c) and subsequent large- N expansion is then applied to the operators $\{J'_l\}$.

The master equation obtained in this way may be written, for both phases, in the general form (omitting constant energy terms in the Hamiltonian)

$$\begin{aligned} \dot{\rho} = & -i[H_{\text{lin}}, \rho] + \Gamma_{+,k} D[c_k^\dagger] \rho + \Gamma_{-,k} D[c_k] \rho + \Gamma_{+,k}^s \left[2c_k \rho c_k + 2c_k^\dagger \rho c_k^\dagger - \{c_k^2 + (c_k^\dagger)^2, \rho\} \right] \\ & -i\Gamma_{-,k}^s \left[-2c_k \rho c_k + 2c_k^\dagger \rho c_k^\dagger - \{-c_k^2 + (c_k^\dagger)^2, \rho\} \right], \end{aligned} \quad (3.29)$$

with

$$H_{\text{lin}} = A_{1,k} c_k^\dagger c_k + A_{2,k} \left[c_k^2 + (c_k^\dagger)^2 \right] + iA_{3,k} \left[(c_k^\dagger)^2 - c_k^2 \right], \quad (3.30)$$

where $k \in \{<, >\}$ and $c_<$ ($c_>$) denotes the bosonic operator for the normal (broken)

phase. The coefficients in the normal phase are given by

$$A_{1,<} = 2h - \lambda, \quad (3.31a)$$

$$A_{2,<} = -\lambda/2, \quad (3.31b)$$

$$A_{3,<} = 0, \quad (3.31c)$$

$$\Gamma_{+,<} = \Gamma_a, \quad (3.31d)$$

$$\Gamma_{-,<} = \Gamma_a + \Gamma_b, \quad (3.31e)$$

$$\Gamma_{+,<}^s = \Gamma_a, \quad (3.31f)$$

$$\Gamma_{-,<}^s = 0, \quad (3.31g)$$

while in the broken phase they are given by

$$A_{1,>} = \frac{1}{2\Lambda} (-4h^2 - 3\Gamma_b^2 + 4\lambda\Lambda), \quad (3.32a)$$

$$A_{2,>} = \frac{1}{4\lambda\Lambda} \left((\Gamma_b^2 - 4h^2) \sqrt{\lambda^2 - \Gamma_b^2} - 4h\Gamma_b^2 \right), \quad (3.32b)$$

$$A_{3,>} = \frac{\Gamma_b}{4\lambda\Lambda} \left(-4h^2 + \Gamma_b^2 + 4h\sqrt{\lambda^2 - \Gamma_b^2} \right), \quad (3.32c)$$

$$\Gamma_{\pm,>} = \frac{\Gamma_a}{2\lambda\Lambda} (4h^2 + \Gamma_b^2) + \frac{\Gamma_b}{4\Lambda^2} (\mp 2h + \Lambda)^2, \quad (3.32d)$$

$$\Gamma_{+,>}^s = \frac{\Gamma_a}{2\lambda^2\Lambda} \left[(4h^2 - \Gamma_b^2) \sqrt{\lambda^2 - \Gamma_b^2} + 4h\Gamma_b^2 \right] + \frac{\Gamma_b}{4\lambda\Lambda^2} \sqrt{\lambda^2 - \Gamma_b^2} (4h\lambda_c - 2\lambda\Lambda), \quad (3.32e)$$

$$\Gamma_{-,>}^s = \frac{\Gamma_a\Gamma_b}{2\lambda^2\Lambda} (\Gamma_b^2 - 4h^2 + 4h\sqrt{\lambda^2 - \Gamma_b^2}) + \frac{\Gamma_b^2}{4\lambda\Lambda^2} (\Lambda^2 - 4h^2). \quad (3.32f)$$

Note that the Hamiltonian (3.30) does not contain any terms linear in c_k and c_k^\dagger , which is a consequence of the applied rotation, and also means that $\langle c_k \rangle_{ss} = \langle c_k^\dagger \rangle_{ss} = 0$.

While the coefficients for the broken phase are rather complicated, they do simplify considerably in the limit of very large λ ; in particular, for $\lambda \gg h, \Gamma_{a,b}$ one finds $A_{1,>} \simeq 2\lambda$, $A_{2,>} \simeq 0$, and $A_{3,>} \simeq 0$, while $\Gamma_{\pm,>} \simeq \Gamma_b/4$, $\Gamma_{+,>}^s \simeq -\Gamma_b/4$, and $\Gamma_{-,>}^s \simeq 0$. The master equation then corresponds to that of a simple quantized harmonic oscillator coupled to a somewhat unconventional (squeezed-type) reservoir [49].

Eigenvalue analysis

It is interesting to examine the eigenvalues associated with the linear set of equations of motion for the first-order moments $\langle c_k \rangle, \langle c_k^\dagger \rangle$, which may be expressed as $\dot{\vec{u}} = \mathbf{M}\vec{u}$, where $\vec{u} \equiv (\langle c_k \rangle, \langle c_k^\dagger \rangle)^T$ and \mathbf{M} is a 2×2 matrix. The real and imaginary parts of these eigenvalues are plotted in Fig. 3.4 for our characteristic set of numerical parameters. We note that except for the region near zero coupling strength the eigenvalues exhibit very similar behavior to that found in the dissipative Dicke model [33].

In the normal phase ($\lambda < \lambda_c$) the eigenvalues of \mathbf{M} are given by

$$\mu_{\pm} = -\Gamma_b \pm 2i\sqrt{h(h-\lambda)}, \quad (3.33)$$

the imaginary parts of which go to zero at the point $\lambda' = h < \lambda_c$, with a characteristic scaling of $\sqrt{\lambda' - \lambda}$. For $\lambda' < \lambda < \lambda_c$ the eigenvalues are real and distinct, with one going to zero at λ_c (i.e., critical slowing down) and the other to $-2\Gamma_b$.

In the broken phase ($\lambda > \lambda_c$) the eigenvalues of \mathbf{M} are given by

$$\mu_{\pm} = -\frac{2\Gamma_b h}{\Lambda} \pm \sqrt{2(2h^2 + \Gamma_b^2 - \lambda\Lambda)}. \quad (3.34)$$

In the region $\lambda > \lambda''$, where $\lambda'' = (\Gamma_b^2 + 2h^2)/\sqrt{4h\lambda_c}$, the eigenvalues are complex conjugate pairs with a real part that diminishes for $\lambda \gg \lambda_c$ like $-\Gamma_b h/\lambda$. Provided $\Gamma_b < \sqrt{2}h\sqrt{1+\sqrt{5}}$, then $\lambda'' > \lambda_c$ and the imaginary parts vanish as λ approaches λ'' from above with the scaling $\sqrt{\lambda - \lambda''}$ (which can be shown using a first-order Taylor series expansion about $\lambda = \lambda''$). The imaginary parts are zero in the interval $\lambda_c < \lambda < \lambda''$, while the real parts again approach 0 and $-2\Gamma_b$, respectively, as $\lambda \rightarrow \lambda_c$.

If $\Gamma_b > \sqrt{2}h\sqrt{1+\sqrt{5}}$ then $\lambda'' < \lambda_c$, and the eigenvalues are complex conjugate pairs immediately above the critical point. In this situation, the dissipation is stronger than the Hamiltonian dynamics; this is also an interesting regime, but not one that we will consider in the present paper.

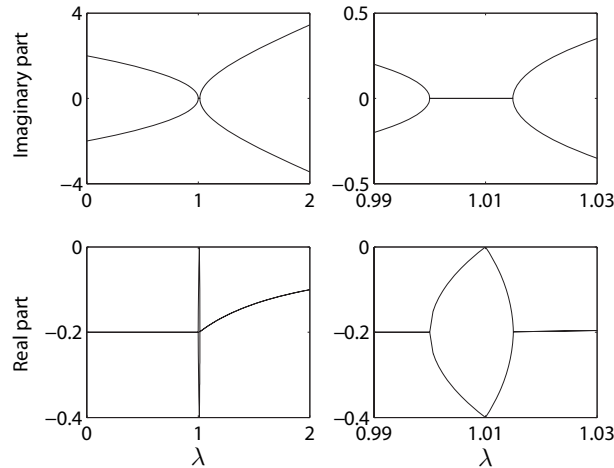


Figure 3.4. *Eigenvalues of the linearized equations of motion, μ_{\pm} , as given by Eqs. (3.33) and (3.34), for $h = 1$ and $\Gamma_b = 0.2$. The right-hand column gives a magnified view of the region around $\lambda_c = 1.01$.*

Probe transmission spectrum

A standard way to examine the structure and dynamics of an atomic system is to measure the transmission of a (weak) probe laser field through the medium as a function

of the probe frequency. This amounts simply to detecting the frequency response of the system to an applied field or “force”. A schematic diagram illustrating the setup for such a measurement in the present context is shown in Fig. 3.2 (a).

For our theoretical investigation of the transmission spectrum we retain the two cavity modes in our model and make use of the input-output theory of open quantum systems [40, 41]. In particular, our starting point is the atom-cavity Hamiltonian (3.6) and we again consider the limit $N \gg 1$, so that we can perform a linearization. To do this, we follow our previous working and determine the stable semiclassical steady-state amplitudes of the atom-cavity system from the semiclassical (i.e., factorized) equations of motion for the moments $\{\langle a \rangle, \langle b \rangle, \langle J_x \rangle, \langle J_y \rangle, \langle J_z \rangle\}$. Note that the steady-state cavity mode amplitudes in this approach can be expressed in terms of the atomic amplitudes as (neglecting terms proportional to $\delta_{a,b}^-$ and setting $\delta_b = 0$)

$$\frac{\langle a \rangle_{ss}}{\sqrt{N}} = \frac{-2i\lambda_a}{\kappa_a + i\delta_a} X_{ss}, \quad \frac{\langle b \rangle_{ss}}{\sqrt{N}} = \frac{\lambda_b}{\kappa_b} (Y_{ss} - iX_{ss}). \quad (3.35)$$

Using the HP representation of the atomic spin operators and linearizing about the semiclassical steady states as before leads to the following Hamiltonian for the normal and broken phases,

$$\begin{aligned} H_{g,\text{lin}} = & \delta_c c_k^\dagger c_k + \delta_a a_k^\dagger a_k + \delta_b b_k^\dagger b_k + (Ac_k + A^* c_k^\dagger)(a_k + a_k^\dagger) \\ & + (B_1 c_k + B_2 c_k^\dagger)b_k + (B_1^* c_k^\dagger + B_2^* c_k)b_k^\dagger, \end{aligned} \quad (3.36)$$

where $k \in \{<, >\}$, a_k and b_k denote the annihilation operators for the intracavity modes in the normal and broken phases, and the coefficients $\{\delta_c, A, B_1, B_2\}$ are given in Appendix 3.A.

Employing the quantum Langevin equations of the input-output theory of open quantum systems we can analytically solve for any cavity output correlations and spectra of interest [33]. Here, however, we focus simply on the amplitude of a probe laser field transmitted through the system and into the output field, as depicted in Fig. 3.2 (a). We consider only the case in which a probe laser of frequency ν_p (in the rotating frame) and amplitude \mathcal{E}_p drives cavity field mode b .

The analytical expression for the amplitude of the transmitted probe, $A_p(\nu)$, is rather complicated, but if we restrict ourselves to a frequency range where $|\nu| \ll \delta_a, \kappa_b$ (also with $\kappa_a \ll \delta_a$), then for $\lambda < \lambda_c$ the transmitted probe intensity is well approximated by

$$\begin{aligned} T_p(\nu) = & |A_p(\nu)|^2 \\ \simeq & \left| 1 - \frac{i\Gamma_b}{4\sqrt{h(h-\lambda)}} \left\{ \frac{(\sqrt{h} + \sqrt{h-\lambda})^2}{[\nu - 2\sqrt{h(h-\lambda)}] + i\Gamma_b} - \frac{(\sqrt{h} - \sqrt{h-\lambda})^2}{[\nu + 2\sqrt{h(h-\lambda)}] + i\Gamma_b} \right\} \right|^2, \end{aligned} \quad (3.37)$$

where we have normalized the intensity such that it takes a maximum value of unity for an empty cavity. This form for $T_p(\nu)$ highlights the presence of atomic resonances at the frequencies $\nu = \text{Im}(\mu_{\pm})$, superimposed on a broad background corresponding to the bare cavity mode resonance. Note that this is in contrast to the findings in the dissipative Dicke model [33] where the probe laser transmission spectrum exhibits strongly coupled atom-cavity resonances.

In Fig. 3.5 we plot the transmission spectrum [computed from the full theory – note that the approximate expression (3.37) is in good agreement for the parameters chosen] for a series of values of λ on either side or the transition. Note that we have chosen $\Gamma_b = 0.05$ here in order to highlight the main features of the spectrum more clearly. For $\lambda \ll \lambda_c$, we observe, at $\nu \simeq 2h$, a single sharp dip of width $2\Gamma_b$ in the envelope of cavity mode resonance, corresponding to a cavity-mediated collective atomic emission resonance ($\delta_c \simeq 2h$); at this λ , spin-spin interactions mediated by cavity mode a are small and have little effect on the spectrum.

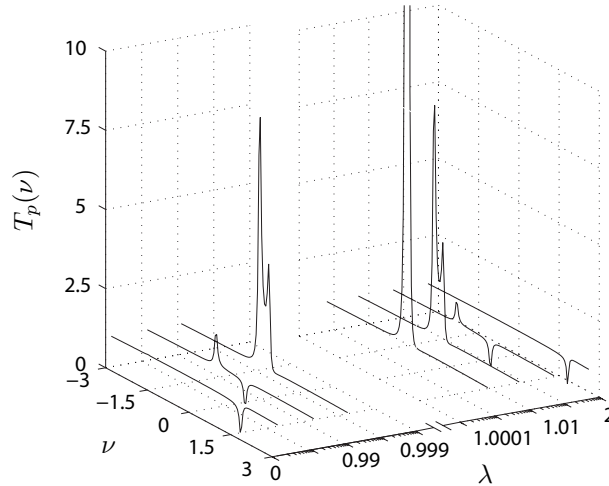


Figure 3.5. *Transmission spectrum in the linearized regime, for $\lambda = 0.3, 0.93, 0.992, 1.000625 (= \lambda_c), 1.005, 1.05, 1.5$, with microscopic parameters $\kappa_a = 0.3$, $\delta_a = 15$, and $\lambda_b = 0.87$, $\kappa_b = 15$, giving $\Gamma_b = 0.05$. We set $h = 1$ as usual. Note that λ_a is chosen to give the indicated λ for the given choice of κ_a and δ_a , viz. Eq. (3.11a) and recalling that $\lambda = 2\Lambda_a$, while Γ_a varies according to Eq. (3.11b), with $\Gamma_a = 0.01$ when $\lambda = \lambda_c$.*

As the interaction strength λ is increased, this dip moves to smaller frequencies and reduces in depth (eventually inverting), while a peak emerges at the corresponding negative frequency. The positions and widths of these features reflect the real and imaginary parts, respectively, of the eigenvalue structure of the system, while their “intensities” also relate to the populations of the energy levels. At $\lambda = h$ the two peaks merge into a single peak centered at $\nu = 0$, with a height $T_p(0) \simeq (h/\Gamma_b)^2$. Then, as $\lambda \rightarrow \lambda_c$, this peak diverges (corresponding to eigenvalue $\mu_- \rightarrow 0$) in a pronounced

signature of the phase transition. A similar divergence in the probe laser transmission spectrum is found in the dissipative Dicke model [33].

Just above the critical point, two peaks reappear in the spectrum and move apart with increasing λ , as shown in Fig. 3.5. The negative frequency peak diminishes in strength, while the peak at positive frequency inverts to a dip, which narrows and moves to increasingly larger frequencies. In fact, for $\lambda \gg 1$, its position is approximated by 2λ and its width by $2\Gamma_b h/\lambda$.

3.5.2 Entanglement

Entanglement criteria

Recently a criterion for bipartite entanglement in collective spin systems was derived [50], and the connection to spin squeezing established. For the case of symmetric states the criterion is both necessary and sufficient, and reads

$$C_\varphi \equiv 1 - \frac{4}{N} \langle \Delta J_\varphi^2 \rangle - \frac{4}{N^2} \langle J_\varphi \rangle^2 > 0, \quad (3.38)$$

where $J_\varphi = \sin(\varphi)J_x + \cos(\varphi)J_y$. In this work, we will use the magnitude of C_φ as a quantitative measure of the entanglement in the system. Note that for finite N , and also in the linearized analysis, we have $\langle J_\varphi \rangle = 0$ [since there are no linear driving terms in the effective Hamiltonians (3.21) and (3.30)], and thus $C_\varphi = 1 - (4/N) \langle J_\varphi^2 \rangle$. Note also that $C_{\varphi=0} \equiv C_y$, which was shown to be equivalent to the concurrence, C [51], in nondissipative LMG models [9].

We also compute the rescaled concurrence, $C_R = (N-1)C$, which is the relevant (nonvanishing) quantity to study for infinitely coordinated collective spin systems in the thermodynamic limit [15, 29]. It is possible to show that for the system considered here, C_R may be written as [52]

$$C_R = \begin{cases} 2\max\{0, C_1\} & \text{if } E < F \\ 2\max\{0, C_2\} & \text{if } E \geq F \end{cases}$$

where

$$C_1 = \frac{|\langle J_+^2 \rangle|}{N} - \frac{\langle J_x^2 \rangle + \langle J_y^2 \rangle}{N} + \frac{1}{2}, \quad (3.39)$$

$$C_2 = \frac{N}{4} - \frac{\langle J_z^2 \rangle}{N} - \frac{\sqrt{[(N(N-2) + 4\langle J_z^2 \rangle)]^2 - [4(N-1)\langle J_z \rangle]^2}}{4N}, \quad (3.40)$$

and

$$E = \frac{N}{2} - \frac{2\langle J_z^2 \rangle}{N}, \quad (3.41)$$

$$F = \frac{\sqrt{[(N(N-2) + 4\langle J_z^2 \rangle)]^2 - [4(N-1)\langle J_z \rangle]^2}}{4N} + \frac{|\langle J_+^2 \rangle|}{N}. \quad (3.42)$$

As pointed out in Sec. 3.2.3, the spin variances required to compute the entanglement measures described above can in principle be determined from appropriate measurements performed on the cavity output field.

Steady-state entanglement

For finite N we numerically solve the master equation for the steady-state density matrix and then compute the operator averages required to determine C_φ and C_R . In Fig. 3.6 we plot $\max\{0, C_\varphi\}$ as a function of λ and φ for $N = 100$. We see that below the critical point, $\lambda < \lambda_c$, entanglement is present for a broad range of angles φ . However, as the critical point is approached the range of angles φ which gives nonzero entanglement, $C_\varphi > 0$, becomes increasingly narrow. Once above the transition, $\lambda > \lambda_c$, the region of finite C_φ continues to narrow until it eventually disappears altogether.

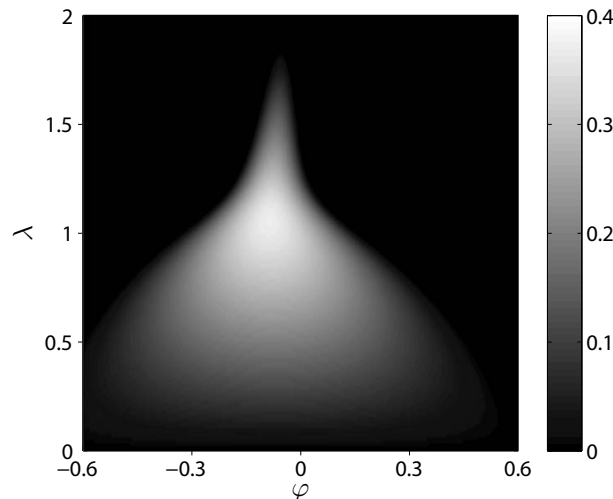


Figure 3.6. Entanglement measure $\max\{0, C_\varphi\}$ for $N = 100$, $h = 1$, $\Gamma_a = 0.01$, and $\Gamma_b = 0.2$.

To help interpret the behavior of C_φ , we make use of a phase space representation of the atomic state that employs the spin coherent states, which are defined by [52]

$$|\eta\rangle = (1 + |\eta|^2)^{-j} \sum_{m=-j}^j \sqrt{\binom{N}{j+m}} \eta^{j+m} |j, m\rangle_j, \quad (3.43)$$

where $\eta = e^{i\phi} \tan \frac{\theta}{2}$, with θ and ϕ corresponding to spherical coordinates, and $|j, m\rangle$ are the Dicke states with $m \in [-j, -j+1, \dots, j-1, j]$ (for our system, $j = N/2$). Using these states we can define the spin Q -function,

$$Q_s(\eta) = \langle \eta | \rho | \eta \rangle. \quad (3.44)$$

Fig. 3.7 displays $Q_s(\eta)$ on the surface of the Bloch sphere for $N = 50$ and for a series of interaction strengths λ . Below the critical point, $Q_s(\eta)$ is single-peaked and centered around the top of the Bloch sphere ($\theta = 0$), with little obvious angular dependence. Correspondingly, the entanglement measure C_φ is finite over a rather broad range of φ , with a maximum close to $\varphi = 0$ (i.e., near C_y). Note that this slight shift of the optimum away from $\varphi = 0$ is a consequence of the dissipation (Γ_b) in the system.

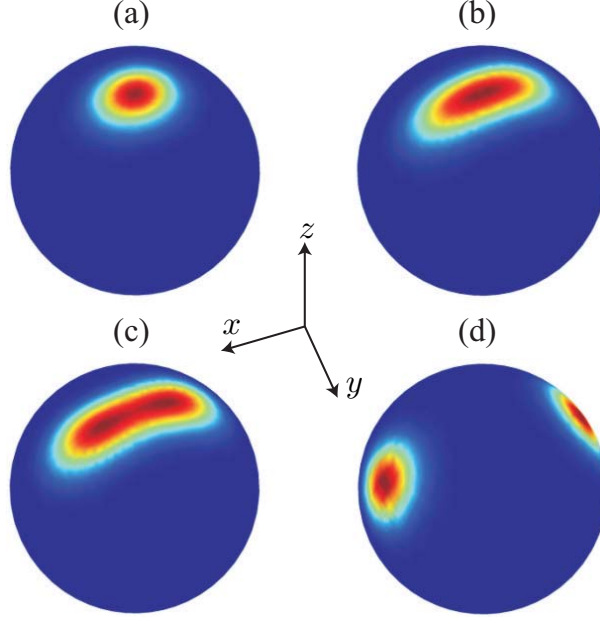


Figure 3.7. (Color online) Steady-state spin Q -function, $Q_s(\eta)$, on the Bloch sphere for (a) $\lambda = 0.5$, (b) $\lambda = 1.01$, (c) $\lambda = 1.1$, and (d) $\lambda = 2$, with $N = 50$, $h = 1$, $\Gamma_a = 0.01$, and $\Gamma_b = 0.2$. Note that dark blue corresponds to the minimum value of zero of $Q_s(\eta)$ while dark red indicates the maximum value of $Q_s(\eta)$.

As λ increases towards the critical point, $Q_s(\eta)$ becomes increasingly elongated along a direction close to the x axis, until, at the transition, it splits into two peaks located approximately at the two semiclassical steady-state amplitudes (3.26b) and (3.26c). These peaks continue to move apart in phase space as the interaction strength is increased further; eventually both peaks will lie in the equatorial plane corresponding to $\theta = \pi/2$ and $\phi = 0, \pi$. Correspondingly, the range of φ over which C_φ remains finite becomes increasingly narrow and is focussed around an axis perpendicular to that along which the two peaks lie. This narrowing of the “width” of C_φ can be explained by noting that, since $\langle J_\varphi \rangle = 0$, we have $C_\varphi = 1 - (4/N) \langle [\sin(\varphi) J_x + \cos(\varphi) J_y]^2 \rangle$. For increasing interaction strength $\lambda > \lambda_c$, $\langle J_x^2 \rangle$ becomes of order $j^2 = N^2/4$ (see Fig. 3.3), and so the optimal choice of φ becomes more critical. In fact, one can show for $\lambda > \lambda_c$ that the range of φ over which $\max\{0, C_\varphi\} > 0$ scales as $1/\sqrt{N}$.

Next, we consider the rescaled concurrence, C_R , as a function of the interaction strength λ . In fact, one finds that

$$C_R = \max_{\varphi} C_{\varphi}, \quad (3.45)$$

i.e., C_R is simply the optimal value of the quantity C_{φ} just considered. In Fig. 3.8 we plot C_R versus λ and observe that the entanglement reaches a maximum for λ close to λ_c [at finite N the critical point is slightly shifted from λ_c as given in Eq. (3.24)]. This peaking of the entanglement at the quantum phase transition has been conjectured and demonstrated theoretically for the equivalent closed (nondissipative) spin models [12, 14, 15]. Our results confirm that this behavior can persist in steady state in our nonequilibrium, open-system version of these models, and can in principle be measured within our proposed setup.

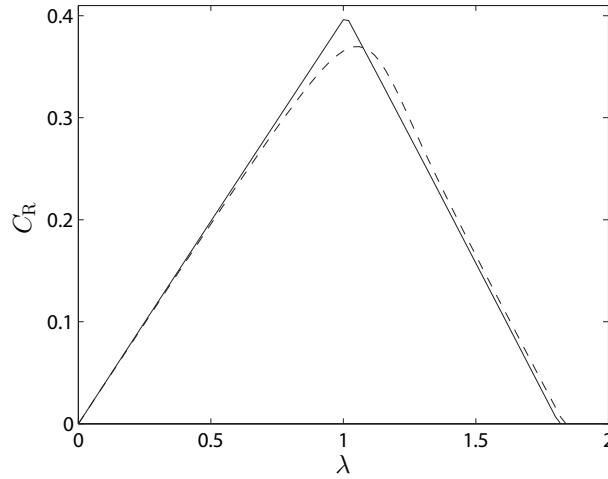


Figure 3.8. Rescaled concurrence C_R for $N = 100$ (dashed line) and in the thermodynamic limit (solid line) with $h = 1$, $\Gamma_a = 0.01$, and $\Gamma_b = 0.2$.

In the linearized treatment ($N \gg 1$) of the HP representation, we can write $J_{\varphi} \approx (\sqrt{N}/2)\chi_{\varphi}$, where $\chi_{\varphi} = i(-c_k e^{i\varphi} + c_k^{\dagger} e^{-i\varphi})$. Noting that $\langle c_k \rangle = 0$, the entanglement measure C_{φ} can be expressed as

$$C_{\varphi}^{\text{HP}} = 1 - \langle \chi_{\varphi}^2 \rangle = \left(e^{2i\varphi} \langle c_k^2 \rangle + e^{-2i\varphi} \langle (c_k^{\dagger})^2 \rangle - 2 \langle c_k^{\dagger} c_k \rangle \right), \quad (3.46)$$

while the rescaled concurrence is C_R is given by

$$C_R^{\text{HP}} = \begin{cases} 2\max\{0, \mathcal{C}_1^{\text{HP}}\} & \text{if } E^{\text{HP}} < F^{\text{HP}} \\ 2\max\{0, \mathcal{C}_2^{\text{HP}}\} & \text{if } E^{\text{HP}} \geq F^{\text{HP}} \end{cases}$$

where

$$\mathcal{C}_1^{\text{HP}} = |\langle c_k^2 \rangle| - \langle c_k^{\dagger} c_k \rangle, \quad (3.47)$$

$$\mathcal{C}_2^{\text{HP}} = \langle c_k^{\dagger} c_k \rangle - \sqrt{\langle (c_k^{\dagger} c_k)^2 \rangle - \langle c_k^{\dagger} c_k \rangle}, \quad (3.48)$$

and

$$E^{\text{HP}} = 2\langle c_k^\dagger c_k \rangle, \quad (3.49)$$

$$F^{\text{HP}} = \sqrt{\langle (c_k^\dagger c_k)^2 \rangle - \langle c_k^\dagger c_k \rangle + |\langle c_k^2 \rangle|}. \quad (3.50)$$

Using the linearized master equation (3.29), we can derive a closed set of equations for the second-order moments $\langle c_k^\dagger c_k \rangle$, $\langle c_k^2 \rangle$, and $\langle (c_k^\dagger)^2 \rangle$, from which we may determine the steady-state solutions analytically. Note that the fourth-order moment appearing in F^{HP} can be expressed in terms of second-order moments, since the states we are dealing with in this linearized approximation are necessarily Gaussian.

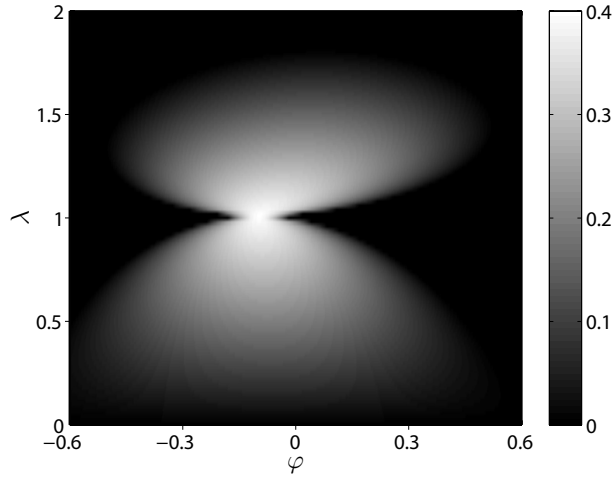


Figure 3.9. Entanglement measure $\max\{0, C_\varphi\}$ in the thermodynamic limit for $h = 1$, $\Gamma_a = 0.01$, and $\Gamma_b = 0.2$. Above the critical point, the system is linearized about only one of the two semiclassical steady-state amplitudes; hence the less-sensitive dependence of $\max\{0, C_\varphi\}$ on φ for $\lambda > \lambda_c$ as compared with the finite- N results.

In Fig. 3.9 we plot C_φ as a function of φ and λ , as determined from the linearized HP representation. The behavior below the critical point ($\lambda < \lambda_c$) is very similar to the finite- N case. However, the behavior above the critical point ($\lambda > \lambda_c$) is very different. Here, the sensitivity of C_φ to φ , for $\lambda > \lambda_c$, is much less critical because the linearized model describes only the fluctuations around one of the two semiclassical steady-state amplitudes (i.e., around one of the two lobes appearing in the spin Q -function for $\lambda > \lambda_c$).

Note that we can obtain plots of $\max\{0, C_\varphi\}$ similar to Fig. 3.6 for the region $\lambda > \lambda_c$, but determined from the linearized HP model (with a finite value of N), by making a rotation back to the original coordinate system and then setting, by hand, $\langle \chi_\varphi \rangle = 0$, to mimic an equal, incoherent mixture of the states associated with the two semiclassical amplitudes.

Finally, returning to Fig. 3.8, we have plotted C_R as a function of λ , computed from the HP model in the thermodynamic limit. Again, C_R corresponds to the value of C_φ optimized over φ , and, since the optimal φ corresponds to an axis perpendicular to the (above-transition) splitting of the semiclassical amplitudes, we expect, and indeed find, good agreement with the finite- N results over the full range of λ .

If we make the simplifying assumption that $\Gamma_a \simeq 0$, then, for $\lambda < \lambda_c$ one can show that $E^{\text{HP}} < F^{\text{HP}}$ and

$$C_R^{\text{HP}} \simeq \frac{\lambda(\sqrt{4h(\lambda_c - \lambda)} + \lambda^2 - \lambda)}{4h(\lambda_c - \lambda)} \quad (3.51)$$

$$\simeq \frac{1}{2} - \frac{1}{2} \frac{h(\lambda_c - \lambda)}{\lambda_c^2} \quad \text{for } \lambda_c - \lambda \ll \lambda. \quad (3.52)$$

This shows reasonable agreement with the plot, but reaches a maximum value of 0.5 at the critical point.

Entanglement dynamics

We now consider the dynamics of the entanglement; starting from an initially unentangled state, we examine the time evolution of the state and its entanglement as quantified by $C_R(t)$. The initial state is taken as the $\lambda = 0$ ground state, i.e., the state with all atomic spins pointing up (which is a convenient state to prepare in an experiment). As in the previous section, we compute the entanglement both numerically for finite N and analytically for $N \gg 1$ in the linearized approximation.

In Fig. 3.10 we plot $C_R(t)$ versus λ and time t for $N = 100$. At long times we recover the results of the previous section, but at short times the behavior as a function of λ is quite different; the entanglement rises to a high value and remains at that value for increasing interaction strength λ . This behavior can be attributed to the Hamiltonian dynamics, which dominate the dissipation at short times and can create highly entangled states. The potential of such Hamiltonian dynamics for generating such highly entangled states has been proposed previously, for example, in Refs. [17, 18]. Note, however, that the presence of the term $-2hJ_z$ in our system Hamiltonian tends to make the generated states more complicated and less straightforward to interpret. Although the focus of this paper is on the quantum phase transition, it is clear that with a slight modification the scheme also has interesting potential for the controlled generation of specific, highly entangled multiatom states (e.g., Greenberger-Horne-Zeilinger states). In connection with this, an important aspect of our implementation should be highlighted here: because both the effective interaction and dissipation of the spins is controlled by the optical laser fields, we can in principle “freeze” the state of the atomic system at any time by simply turning these fields off.

In the linearized regime, $N \gg 1$, we solve the equations of motion for the second-order moments, $\langle c_k^\dagger c_k \rangle$, $\langle c_k^2 \rangle$, and $\langle (c_k^\dagger)^2 \rangle$, with the initial conditions $\langle c_k^\dagger(0)c_k(0) \rangle = 0$,

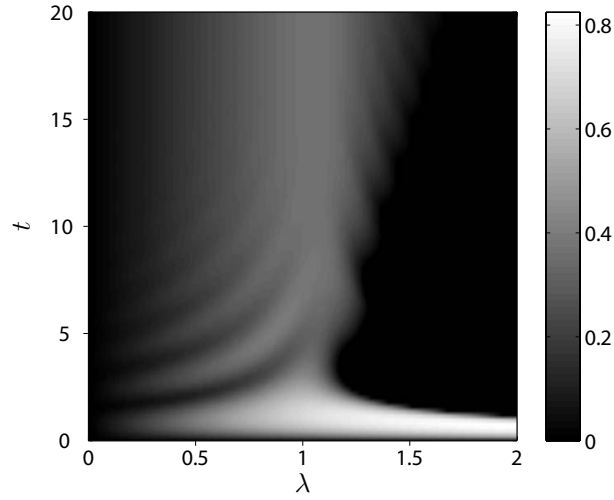


Figure 3.10. *Rescaled concurrence $C_R(t)$ as a function of λ and t for $N = 100$, $h = 1$, $\Gamma_a = 0.01$, and $\Gamma_b = 0.2$.*

$\langle c_k^\dagger(0)^2 \rangle = \langle c_k(0)^2 \rangle = 0$. The results for $C_R(t)$ are shown in Fig. 3.11. Below the critical point the behavior is similar to that observed for finite N . However, above the critical point, where the dynamics is linearized about only one of the two allowed semiclassical steady-state amplitudes, the rescaled concurrence is, as expected, quite different, owing to the more limited range of entangled states that the linearized (Gaussian) theory can accommodate.

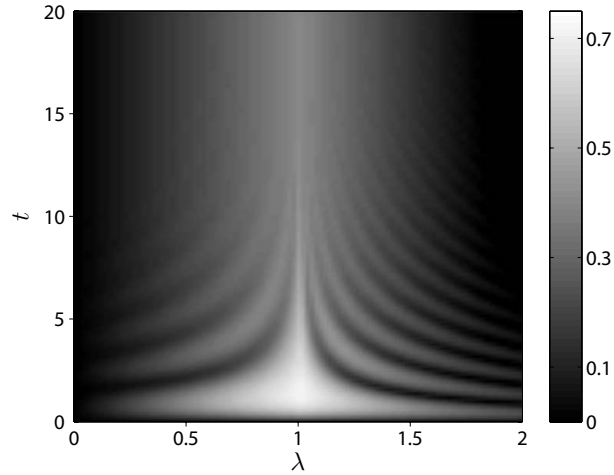


Figure 3.11. *Rescaled concurrence $C_R(t)$ as a function of λ and t in the thermodynamic limit, with $h = 1$, $\Gamma_a = 0.01$, and $\Gamma_b = 0.2$. Above the critical point the dynamics is linearized around one of the two possible semiclassical steady-state amplitudes.*

3.6 First-Order Phase Transition

We now turn to the case of a fixed, positive interaction strength ($\lambda > 0$) of the $\gamma = 0$ model (Sec. 3.3.3) with variable effective field h . In the absence of dissipation this model exhibits two second-order transitions as h is varied, one occurring at positive h (the transition discussed in the previous section) and the other, equivalent transition occurring at negative h . However, in this section we show that with the addition of dissipation this model actually exhibits a first-order phase transition near $h \simeq 0$ (note that in the absence of dissipation no such transition exists). As in the previous section, we begin with a study of the linearized spin master equation, including an eigenvalue analysis and calculation of the probe transmission spectrum, after which we focus again on the entanglement properties of the system. For numerical calculations we will typically employ the set of normalized parameters $\{\lambda = 1, \Gamma_a = 0.01, \Gamma_b = 0.2\}$, which correspond to a critical effective field strength $h_c \simeq 0$.

3.6.1 Linearized model

As before, we consider the thermodynamic limit and linearize the master equation (3.22) about the mean-field state. To do so, we first find the semiclassical steady-state solutions and then expand the angular momentum operators around these mean-field solutions using the Holstein-Primakoff representation.

Semiclassical steady-state solutions

From the (factorized) semiclassical equations of motion for X , Y , and Z , Eqs. (3.23a)-(3.23c) we again obtain the stable steady-state solutions. These exhibit discontinuities at the critical field strengths

$$h_c = \frac{1}{2} \left(\lambda - \sqrt{\lambda^2 - \Gamma_b^2} \right), \quad (3.53)$$

and $h = 0$. For $h < 0$ the stable steady-state solutions are given by Eq. (3.25), while for $h_c < h < (\lambda + \sqrt{\lambda^2 - \Gamma_b^2})/2$ [54] the stable steady states are given by Eqs. (3.26a)-(3.26c). While outside the region $0 < h < h_c$ the stable steady states are unique, inside the region $0 < h < h_c$ both steady-state solutions (3.25) and (3.26a)-(3.26c) are in fact stable. However, for the characteristic parameters we consider here this region is very small ($h_c \simeq 0.01$). Moreover, we have verified (from a linearized analysis) that the steady-state solution (3.25) is more stable in the region $0 < h < h_c$ and thus we will only consider this solution in that region. Note that for larger values of the dissipation, Γ_b , this region becomes more pronounced (in this case all stable steady states should be considered [53]), but this is beyond the regime we wish to consider here.

The relevant stable steady-state solutions Z_{ss} , X_{ss} and Y_{ss} are plotted in Fig. 3.12, together with results from numerical solutions of the master equation for a range of

values of N up to 100 (at which agreement between the two approaches is already quite good). The discontinuous jump of Z_{ss} at $h_c \simeq 0$ signifies the first-order phase transition. Note that for the case $\lambda < 0$ the same first order transition occurs except that it is shifted to $-h_c$ (i.e., in Fig. 3.12 all curves are flipped about $h = 0$).

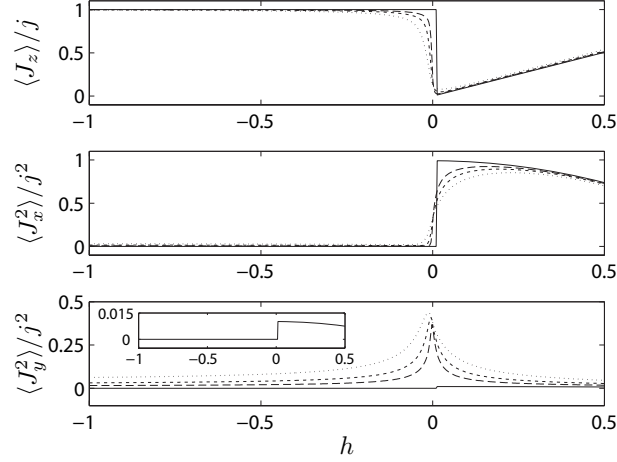


Figure 3.12. *Semiclassical (solid line) and finite- N steady-state solutions for $\lambda = 1$, $\Gamma_a = 0.01$, $\Gamma_b = 0.2$, and $N = 25$ (dotted), 50 (short dashed line), 100 (long dashed line). Note the inset in the bottom panel is a magnified plot of the semiclassical solution of $\langle J_y^2 \rangle / j^2$.*

Holstein-Primakoff representation

Here, we again include the quantum fluctuations for $N \gg 1$ as a first-order correction by linearizing the spin operators around the semiclassical steady state via the HP representation. For $h < h_c$ (normal phase) the linearized master equation is identical to Eq. (3.29) with $k = <$, while for $h > h_c$ (broken phase) the linearized master equation is also identical to Eq. (3.29) but with $k = >$.

Eigenvalue analysis

The eigenvalues of the linearized system, i.e., of the matrix \mathbf{M} , where $\dot{\vec{u}} = \mathbf{M}\vec{u}$ and $\vec{u} \equiv (\langle c \rangle, \langle c^\dagger \rangle)^T$, for $h < h_c$ are given by Eq. (3.33) while for $h > h_c$ they are given by Eq. (3.34). In Fig. 3.13 the real and imaginary parts of the eigenvalues are plotted for our characteristic set of parameters. In the normal phase ($h < h_c$) we see that the imaginary parts go to zero at the point $h' = 0 < h_c$. In the region $h' < h < h_c$ both eigenvalues are real and distinct, with one going to zero at h_c and the other going to $-2\Gamma_b$. This behavior is the same as that found for the second-order transition of the earlier section. However, immediately above the transition, $h > h_c$, the eigenvalues become complex conjugate pairs with a nonzero real part that diminishes for $h \gg h_c$.

like $-\Gamma_b h/\lambda$. This discontinuous jump of the eigenvalues is an additional signature of the first-order phase transition.

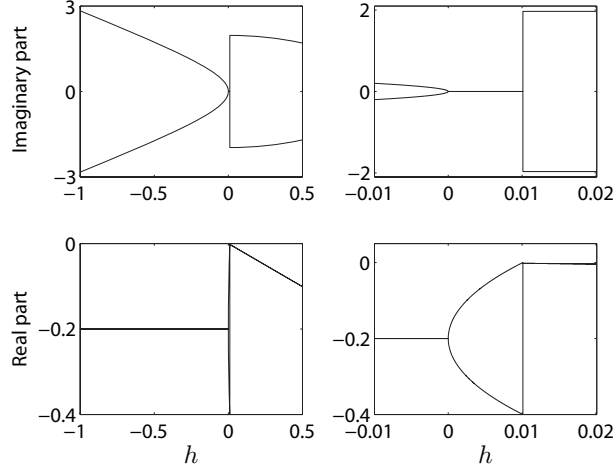


Figure 3.13. *Eigenvalues of the linearized equations of motion, μ_{\pm} , as given by Eqs. (3.33) and (3.34), for $\lambda = 1$, and $\Gamma_b = 0.2$. The right-hand column gives a magnified view of the region around $h_c = 0.0101$.*

Transmission spectrum

We determine the probe transmission spectrum in the linearized regime following exactly the same calculations as outlined in Sec. 3.5.1. The linearized Hamiltonian describing the full atom-cavity system is easily obtained; for $h < h_c$ it is given by Eq. (3.36) with $\theta = 0$ and $\phi = 0$, while for $h > h_c$ it is also given by Eq. (3.36), but with θ and ϕ given according to the semiclassical solutions Eqs. (3.26a)-(3.26c) as explained in Sec. 3.5.1.

Restricting ourselves again to a frequency range where $|\nu| \ll |\delta_a|, \kappa_b$ (also with $\kappa_a \ll |\delta_a|$), then as previously an approximate expression for the transmitted probe intensity can be derived in the normal phase for $h < h_c$ and takes exactly the same form as Eq. (3.37).

In Fig. 3.14 we plot the transmission spectrum for a series of values of h across the critical point h_c . In the normal phase ($h < h_c$), we observe the same behavior as in the normal phase of the system in the previous section ($\lambda < \lambda_c$), except that the orientations of the peaks and dips have inverted in accordance with the change of sign of the field ($h < 0$). The central peak diverges as the critical point is approached from below in the normal phase, again signifying the phenomenon of critical slowing down in the vicinity of the phase transition. However, immediately above the critical point, the spectrum splits discontinuously into two sharp peaks of width $\sim \Gamma_b h/\lambda$, located at frequencies $\nu \simeq \pm 2\lambda$. This jump from a single divergent peak at $\nu = 0$ to a two-peaked spectrum offers a pronounced, observable signature of the first-order transition.

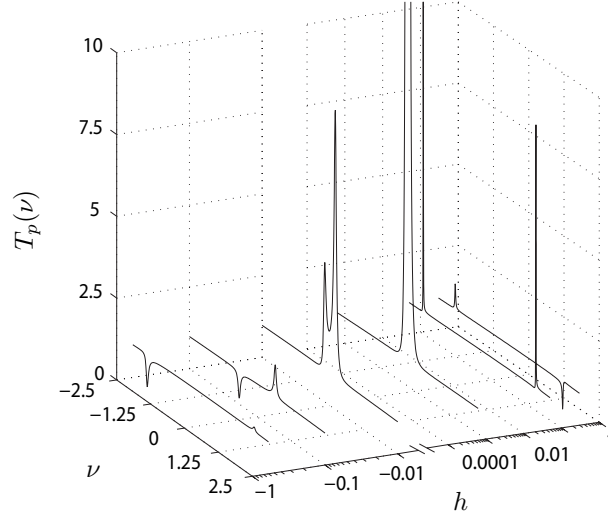


Figure 3.14. *Transmission spectra in the linearized regime, for $h = -0.6, -0.1, -0.01, 6.25 \times 10^{-4} (= h_c), 0.05, 0.3$, with microscopic parameters $\kappa_a = 0.3$, $\delta_a = 15$, $\lambda_a = 2.7$, $\lambda_b = 0.87$, and $\kappa_b = 15$, giving $\lambda = 1$, $\Gamma_a = 0.01$ and $\Gamma_b = 0.05$.*

3.6.2 Entanglement

Steady-state entanglement

We compute, as before, the entanglement measures C_φ and C_R , both numerically for finite N and analytically for $N \gg 1$ in the linearized regime. Fig. 3.15 shows a plot of C_φ as a function of h and φ for $N = 100$. We see that, well away from the critical point, substantial entanglement is present over a broad range of angles φ . As the critical point is approached from below, significant entanglement persists, but for a somewhat narrower range of angles φ . However, immediately above the critical point the entanglement drops suddenly to zero for all values of φ .

To help understand these results we again utilize the atomic coherent state representation and study the spin Q -function $Q_s(\eta)$. In Fig. 3.16 we plot $Q_s(\eta)$ on the Bloch sphere for a series of values of h in the vicinity of the first-order transition. Well below the critical point, in the normal phase, $Q_s(\eta)$ is a single peaked function with little angular dependence. Correspondingly, C_φ is nonzero over a broad range of φ , with a maximum close to $\varphi = \pi/2$ (i.e., near C_x). Again, note that this slight shift of the optimum away from $\varphi = \pi/2$ is a consequence of the dissipation (Γ_b) in the system.

As h increases towards the critical point, $Q_s(\eta)$ becomes increasingly stretched along the y axis. As the critical point is traversed $Q_s(\eta)$ rapidly rotates around from the y axis towards the x axis, and splits into the familiar two-lobed structure associated with the two semiclassical steady-state amplitudes of the broken phase. At the same time as the critical point is approached, the range of φ over which C_φ remains finite narrows

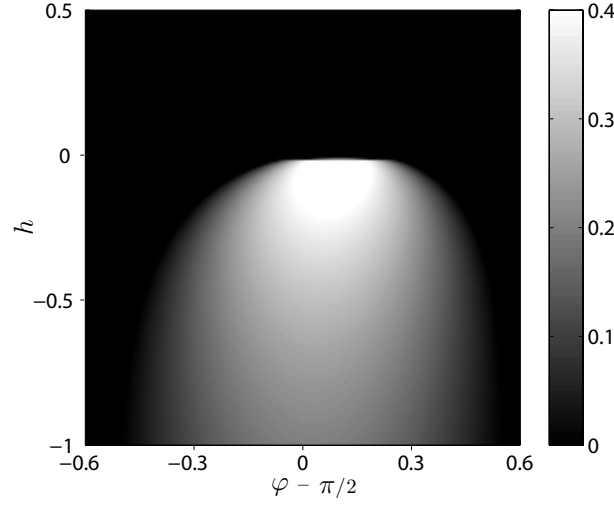


Figure 3.15. Entanglement measure $\max\{0, C_\varphi\}$ as a function of h and φ for $N = 100$, $\lambda = 1$, $\Gamma_a = 0.01$, and $\Gamma_b = 0.2$.

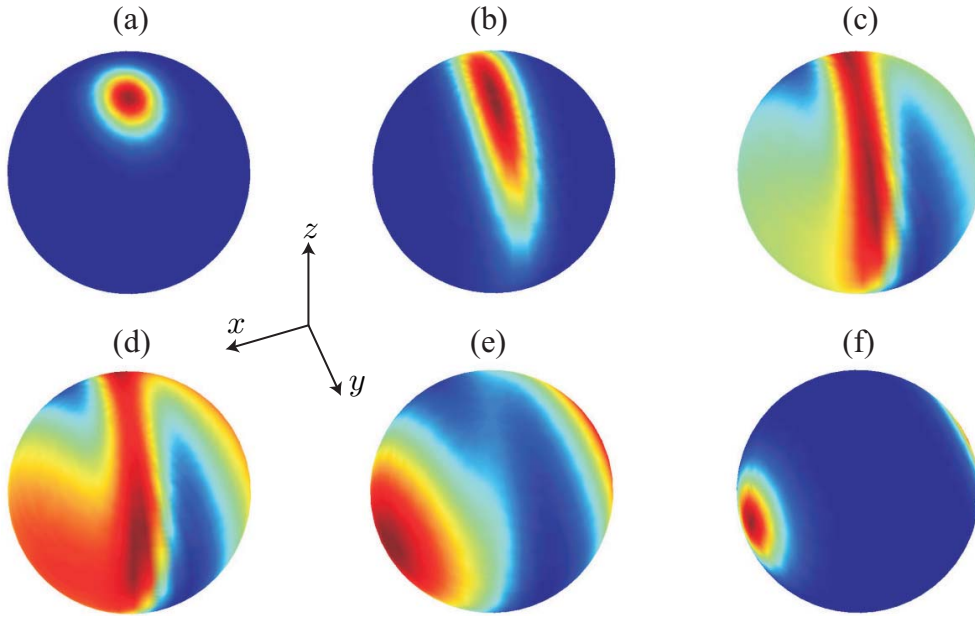


Figure 3.16. (Color online) Steady-state spin Q -function, $Q_s(\eta)$, on the Bloch sphere for (a) $h = -0.5$, (b) $h = -0.01$, (c) $h = 2.5 \times 10^{-3}$, (d) $h = 5 \times 10^{-3}$, (e) $h = 0.015$, and (f) $h = 0.15$, with $N = 50$, $\lambda = 1$, $\Gamma_a = 0.01$, and $\Gamma_b = 0.2$. Note that dark blue corresponds to the minimum value of zero of $Q_s(\eta)$ while dark red indicates the maximum value of $Q_s(\eta)$.

and immediately above the critical point it drops abruptly to zero for all choices of φ . This behavior is akin to the behavior we observed for large interaction strength in the regime of the previous section, where $\langle J_x^2 \rangle$ becomes of order $j^2 = N^2/4$ (see Fig. 3.12), which severely restricts the range of φ for which $C_\varphi > 0$. Note that at larger values of h than displayed in Fig. 3.15, the entanglement, C_φ , once again becomes nonzero (centered around $\varphi \approx 0$) coinciding with the broken phase behavior of the second-order transition discussed in the previous section.

In Fig. 3.17 we plot the rescaled concurrence C_R as a function of the effective field strength h and again find that close to the critical point, h_c , the entanglement reaches its peak value. Although the equivalent closed system would not feature a maximum in the entanglement near h_c (due to the complete absence of a phase transition), this result is in agreement with a conjecture concerning entanglement in open systems at quantum critical points [39].

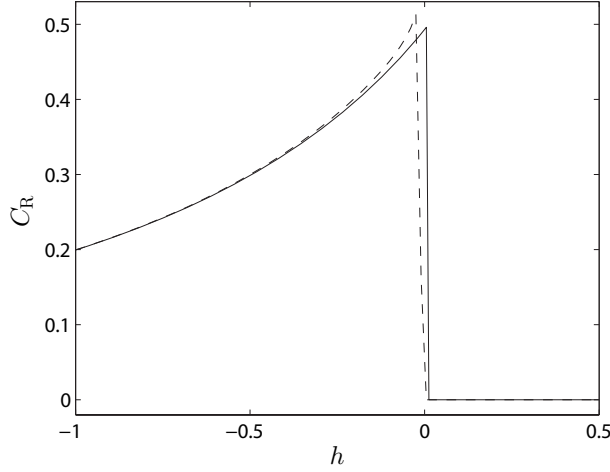


Figure 3.17. Rescaled concurrence C_R versus h for $N = 100$ (dashed line) and in the thermodynamic limit (solid line) with $\lambda = 1$, $\Gamma_a = 0.01$, and $\Gamma_b = 0.2$.

In the linearized treatment ($N \gg 1$) we obtain very similar plots of C_φ to those of finite N (Fig. 3.15) and for C_R the result is shown in Fig. 3.17. In the limit where we consider $\Gamma_a \simeq 0$ we can again obtain an approximate expression for the rescaled concurrence (for $h \leq h_c$) given, in this instance, by

$$C_R^{\text{HP}} \simeq \frac{\lambda(\sqrt{(h - \Lambda/2)(h - h_c)} + \lambda^2 - \lambda)}{4(h - \Lambda/2)(h - h_c)} \quad (3.54)$$

$$\simeq \frac{1}{2} - \frac{1}{2} \frac{h_c - h}{\lambda} \quad \text{for } h_c - h \ll \lambda. \quad (3.55)$$

This again has a maximum value of 0.5 at the critical point, and, for large $|h|$, drops off like $1/|h|$, in reasonable agreement with the plots.

Entanglement dynamics

Finally, in Fig. 3.18 for $N = 100$ we illustrate the time-dependent behavior of the rescaled concurrence, $C_R(t)$, for varying h , given an initial (unentangled) state with all spins up. Once again, we observe an interesting oscillatory behavior of $C_R(t)$, with, in particular, highly entangled states generated by the Hamiltonian dynamics at short times (for almost all values of h), before dissipation has had time to play a significant role. For the linearized regime ($N \gg 1$) a similar plot of $C_R(t)$ can be obtained which agrees well with the finite N result for $h < h_c$ but shows zero entanglement for almost all values of $h > h_c$ because of the restricted linearization around only one of the two permitted semiclassical steady-state amplitudes.

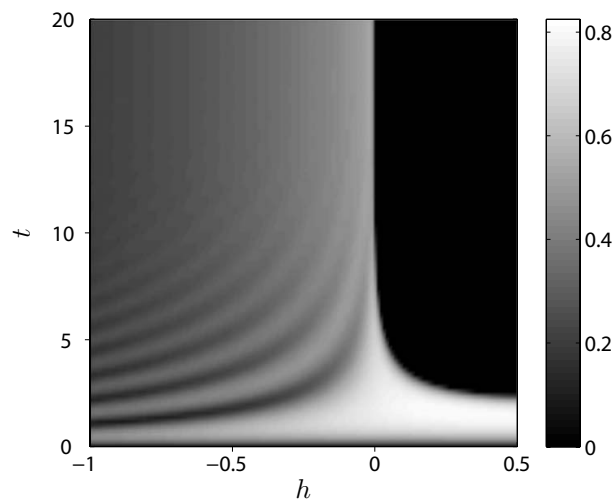


Figure 3.18. *Rescaled concurrence $C_R(t)$ for $N = 100$, with $\lambda = 1$, $\Gamma_a = 0.01$, and $\Gamma_b = 0.2$.*

3.7 Conclusions

We have proposed in this paper a feasible cavity QED setup, consisting of a collective atomic pseudospin and two quantized cavity modes, which realizes a dissipative version of the LMG model in which the interacting spin system displays both first- and second-order nonequilibrium quantum phase transitions. The lossy cavity's output light fields can be utilized to monitor the system as the model parameters are varied; specifically, we showed that the transmission spectra vary dramatically in the vicinity of the transition, with features that are characteristic of the criticality. A further important result is the steady-state entanglement criticality at the QPT and the possibility of directly observing this via homodyne detection of the cavity output fields. In particular, the entanglement can be quantified rather directly in terms of measurable atomic quadrature variances. We also observed an important sensitivity of the entanglement measure

to the quadrature phase angle in the critical regimes, which we were able to interpret by employing an atomic phase space distribution. Finally, we have considered how entanglement evolves in this system, observing not only the criticality at the QPT at long times (corresponding to the steady state), but also a rich transient behavior at shorter times.

For future studies, it is clear that the system we have proposed offers a variety of opportunities, such as (i) investigating phase transitions in response to variation of the strength of dissipation (i.e., Γ_b), (ii) examining a system of multiple (separately addressable) atomic pseudospins all coupled to the same quantized cavity modes, which would permit the study of entanglement between different spin blocks [14], (iii) controlled preparation of robust (insensitive to noise/environment), highly entangled states by evolution from an initial product state [17, 18], (iv) measurement of more general atomic spin correlations and their evolution with time, which can also provide signatures of criticality in QPT's [55], (v) extending our system to accommodate more complex spin models, e.g., by adding additional lasers to the setup explained in Sec. 3.2 to realize the so-called “two-field model” [15], and (vi) imposing some spatial variation on the cavity mode to provide, for example, short ranged interactions, which could be uniform or quasirandom.

Acknowledgements

The authors thank A. Daley and H. Carmichael for discussions and acknowledge support from the Austrian Science Foundation and from the Marsden Fund of the Royal Society of New Zealand.

3.A Coefficients of the Atom-Cavity Hamiltonian in the Linearized Regime

In Sec. 3.5.1 we gave the general form of the linearized Hamiltonian of the joint atom-cavity system, Eq. (3.36). The coefficients of this Hamiltonian in terms of the system parameters, $h, \lambda_a, \lambda_b, \Gamma_b$ and the angles θ, ϕ from Sec. 3.5.1 are

$$\delta_c = 2h \cos \theta + 2 \sin \theta [2\lambda X_{ss} \cos \phi - \Gamma_b(Y_{ss} \cos \phi - X_{ss} \sin \phi)], \quad (3.56)$$

$$A = \frac{\lambda_a}{2} [(1 + \cos \theta) + (1 - \cos \theta)(\sin \phi + i \cos \phi)^2], \quad (3.57)$$

$$B_1 = \frac{\lambda_b}{2} [(1 - \cos \theta)(\sin \phi + i \cos \phi)^2], \quad (3.58)$$

$$B_2 = \frac{\lambda_b}{2} (1 + \cos \theta). \quad (3.59)$$

Note that for $\lambda < \lambda_c$ one has $\theta = 0$ and $\phi = 0$, giving the simplified expressions $\delta_c = 2h$, $A = \lambda_a$, $B_1 = 0$, and $B_2 = \lambda_b$. Similar to Sec. 3.5.1, we can also derive simplified expressions in the limit $\lambda \gg \lambda_c$, i.e., for $\lambda \rightarrow \infty$, one has $\delta_c = 4\lambda_a$, $A = 0$, $B_1 = -\lambda_b/2$, and $B_2 = \lambda_b/2$.

Bibliography

- [1] For recent reviews, see D. Jaksch and P. Zoller, Ann. Phys. (N.Y.) **315**, 52 (2005), and I. Bloch, Nature Phys. **1**, 23 (2005).
- [2] M. Greiner, O. Mandel, T. Esslinger, T. Hänsch, and I. Bloch, Nature **415**, 39 (2002).
- [3] A. Micheli, G. K. Brennen, and P. Zoller, Nature Phys. **2**, 341 (2006).
- [4] D. Porras and J. I. Cirac, Phys. Rev. Lett. **92**, 207901 (2004).
- [5] H. J. Lipkin, N. Meshkov, and A. J. Glick, Nucl. Phys. **62**, 188, 199, 211 (1965); N. Meshkov, A. J. Glick, and H. J. Lipkin, *ibid.* **62**, 199 (1965); A. J. Glick, H. J. Lipkin, and N. Meshkov, *ibid.* **62**, 211 (1965).
- [6] A. Osterloh *et al.*, Nature **416**, 608 (2002).
- [7] T. J. Osborne and M. A. Nielsen, Phys. Rev. A **66**, 032110 (2002).
- [8] G. Vidal, J.I. Latorre, E. Rico, and A. Kitaev, Phys. Rev. Lett. **90**, 227902 (2003).
- [9] J. Vidal, G. Palacios, and R. Mosseri, Phys. Rev. A **69**, 022107 (2004).
- [10] J. Vidal, R. Mosseri, and J. Dukelsky, Phys. Rev. A **69**, 054101 (2004).
- [11] J. Vidal, G. Palacios, and C. Aslangul, Phys. Rev. A **70**, 062304 (2004).
- [12] J. I. Latorre, R. Orús, E. Rico, and J. Vidal, Phys. Rev. A **71**, 064101 (2005).
- [13] S. Dusuel and J. Vidal, Phys. Rev. B **71**, 224420 (2005).
- [14] T. Barthel, S. Dusuel, and J. Vidal, Phys. Rev. Lett. **97**, 220402 (2006).
- [15] J. Vidal, Phys. Rev. A **73**, 062318 (2006).
- [16] G. J. Milburn, J. Corney, E. M. Wright, and D. F. Walls, Phys. Rev. A **55**, 4318 (1997).
- [17] A. Micheli, D. Jaksch, J. I. Cirac, and P. Zoller, Phys. Rev. A **67**, 013607 (2003).
- [18] K. Mølmer and A. Sørensen, Phys. Rev. Lett. **82**, 1835 (1999).

- [19] R. G. Unanyan, M. Fleischhauer, N. V. Vitanov, and K. Bergmann, Phys. Rev. A **66**, 042101 (2002); R. G. Unanyan and M. Fleischhauer, Phys. Rev. Lett. **90**, 133601 (2003).
- [20] P. Berman, ed., *Cavity Quantum Electrodynamics* (Academic Press, Boston, 1994).
- [21] K. Hepp and E. H. Lieb, Ann. Phys. (N.Y.) **76**, 360 (1973); Phys. Rev. A **8**, 2517 (1973).
- [22] Y. K. Wang and F. T. Hioe, Phys. Rev. A **7**, 831 (1973).
- [23] F.T. Hioe, Phys. Rev. A **8**, 1440 (1973).
- [24] H. J. Carmichael, C. W. Gardiner, and D. F. Walls, Phys. Lett. A **46**, 47 (1973).
- [25] G. Cromer Duncan, Phys. Rev. A **9**, 418 (1974).
- [26] R. H. Dicke, Phys. Rev. **93**, 99 (1954).
- [27] C. Emary and T. Brandes, Phys. Rev. Lett. **90**, 044101 (2003).
- [28] C. Emary and T. Brandes, Phys. Rev. E **67**, 066203 (2003).
- [29] N. Lambert, C. Emary, and T. Brandes, Phys. Rev. Lett. **92**, 073602 (2004).
- [30] N. Lambert, C. Emary, and T. Brandes, Phys. Rev. A **71**, 053804 (2005).
- [31] J. Reslen, L. Quiroga, and N. F. Johnson, Europhys. Lett. **69**, 8 (2005).
- [32] K. Rzażewski, K. Wódkiewicz, and W. Żacowicz, Phys. Rev. Lett. **35**, 432 (1975).
- [33] F. Dimer, B. Estienne, A. S. Parkins, and H. J. Carmichael, Phys. Rev. A **75**, 013804 (2007).
- [34] R. Bonifacio and L. A. Lugiato, Opt. Commun. **19**, 172 (1976); Phys. Rev. Lett. **40**, 1023 (1978); Phys. Rev. A **18**, 1129 (1978).
- [35] P. D. Drummond and H. J. Carmichael, Opt. Commun. **27**, 160 (1978).
- [36] D. F. Walls, P. D. Drummond, S. S. Hassan, and H. J. Carmichael, Prog. Theor. Phys. Suppl. **64**, 307 (1978).
- [37] P. D. Drummond, Phys. Rev. A **22**, 1179 (1980).
- [38] H. J. Carmichael, J. Phys. B **13**, 3551 (1980).
- [39] S. Schneider and G. J. Milburn, Phys. Rev. A **65**, 042107 (2002).
- [40] C. W. Gardiner and P. Zoller, *Quantum Noise* (Springer-Verlag, Berlin, 1992).

- [41] M. J. Collett and C. W. Gardiner, Phys. Rev. A **30**, 1386 (1984); C. W. Gardiner and M. J. Collett, *ibid.* **31**, 3761 (1985).
- [42] H. M. Wiseman and G. J. Milburn, Phys. Rev. A **47**, 642 (1993).
- [43] For numerical solutions of the atomic collective-spin master equation we make use of: S. M. Tan, *Quantum Optics and Computation Toolbox for Matlab*, available at <http://www.qo.phy.auckland.ac.nz/qotoolbox.html>.
- [44] T. Holstein and H. Primakoff, Phys. Rev. **58**, 1098 (1940).
- [45] E. Ressayre and A. Tallet, Phys. Rev. A **11**, 981 (1975).
- [46] Ch. von Cube, S. Slama, M. Kohler, C. Zimmermann, and Ph. W. Courteille, Fortschr. Phys. **54**, 726 (2006).
- [47] J. Klinner, M. Lindholdt, B. Nagorny, and A. Hemmerich, Phys. Rev. Lett. **96**, 023002 (2006).
- [48] Note that for the case $h < 0$ an analogous second-order transition occurs at $-\lambda_c$.
- [49] D. F. Walls and G. J. Milburn, *Quantum Optics* (Springer-Verlag, Berlin, 1994).
- [50] J. K. Korbicz, J. I. Cirac, and M. Lewenstein, Phys. Rev. Lett. **95**, 120502 (2005); *ibid.* **95**, 259901 (2005).
- [51] W. K. Wootters, Quant. Inf. Comp. **1**, 27 (2001).
- [52] X. Wang and K. Mølmer, Eur. Phys. J. D **18**, 385 (2002).
- [53] S. Morrison and A. S. Parkins (unpublished)
- [54] Note that at $(\lambda + \sqrt{\lambda^2 - \Gamma_b^2})/2$ a second order phase transition analogous to the one already presented in Sec. 3.5 occurs, and thus for the first order transition we will focus on $h \ll (\lambda + \sqrt{\lambda^2 - \Gamma_b^2})/2$.
- [55] A. Das, K. Sengupta, D. Sen, and B. K. Chakrabarti, Phys. Rev. B **74**, 144423 (2006).

CHAPTER 4

MICROSCOPIC CAVITY QED SYSTEM

In this chapter we present the detailed microscopic model of the atom-cavity system used to derive the effective spin-cavity model (and subsequently the collective spin system) we studied in the previous two chapters. The system we consider consists of a cloud of atoms confined inside a cavity and illuminated by several laser fields. The description considered here includes both the ground and excited states of the atoms, and the corresponding electric dipole transitions between them mediated via the lasers and cavity light fields. First in section 4.1 we introduce the system of atoms, whilst in section 4.2 we briefly discuss the dissipative cavity system. Then in section 4.3 we describe the coupling of all atoms to the laser fields and cavity modes, which finally leads us to the full microscopic atom-cavity system in section 4.4

4.1 Atomic System

We begin by considering the description of the internal degrees of freedom of the atomic system¹. We assume large enough inter-atomic separations such that (i) no (e.g., s-wave) scattering occurs between atoms, (ii) the wave functions of the atoms do not overlap (no symmetrization required), and (iii) dipole-dipole interactions between atoms can be neglected. Specifically we assume that each of the N atoms possesses a pair of stable electronic ground states which we denote $|0\rangle$ and $|1\rangle$, with energies ($\hbar = 1$) $\omega_0 = 0$ and ω_1 , respectively. Furthermore we consider two atomic excited atomic states $|r\rangle$ and $|s\rangle$, with energies ω_r and ω_s , respectively, associated with the two ground states (see Fig. 3.1). With all these considerations the Hamiltonian describing the atoms is then given by

$$H_{\text{at}} = \sum_{j=1}^N (\omega_s |s_j\rangle\langle s_j| + \omega_r |r_j\rangle\langle r_j| + \omega_1 |1_j\rangle\langle 1_j|). \quad (4.1)$$

¹We assume that all relevant properties of the system, such as atom-cavity and atom-laser coupling strengths, do not depend on the motion of the atoms and thus we will not consider external degrees of freedom.

We will consider a regime where independent spontaneous emission² of each atom, associated with a decay from either of the two excited states into one of the two ground states, can in fact be neglected. This corresponds to a situation where the single-photon transitions coupling the ground and excited states (described in section 4.3) are far off resonance, and the excited states, $|r\rangle$, $|s\rangle$, are only virtually excited.

4.2 Cavity System

Next we consider a high- Q optical resonator supporting two orthogonal cavity modes, assuming that all other modes are far-detuned from the frequencies of interest and can thus be neglected. Each field mode of the cavity is quantized and described by bosonic annihilation and creation operators, a (b) and a^\dagger (b^\dagger), of a harmonic oscillator with frequency ω_a (ω_b). The Hamiltonian of the cavity system is then given by

$$H_c = \omega_a a^\dagger a + \omega_b b^\dagger b. \quad (4.2)$$

The loss of photons out of each cavity mode is described by the Liouvillian term

$$\mathcal{L}_c \rho_m = \kappa_a (2a\rho_m a^\dagger - a^\dagger a \rho_m - \rho_m a^\dagger a) + \kappa_b (2b\rho_m b^\dagger - b^\dagger b \rho_m - \rho_m b^\dagger b), \quad (4.3)$$

where κ_a and κ_b are the cavity field decay rates for cavity modes a and b respectively, and ρ_m denotes the microscopic density operator.

4.3 Atom, Laser and Cavity Coupling

We now consider the coupling of the ground and excited states of the atoms by the laser fields and cavity modes. In fact we will focus on the case where the laser and cavity fields combine to drive Raman transitions between $|0\rangle$ and $|1\rangle$, via the excited atomic states $|r\rangle$ and $|s\rangle$ (as schematically depicted in Fig.). At the position of each of the j atoms, denoted x_j , the cavity and laser fields are taken to be travelling waves copropagating in the x direction, with sufficiently broad beam waists so as to ensure a homogeneous atom-field coupling.

Specifically, the laser fields, at frequencies ω_{r0} , ω_{s0} , ω_{r1} , and ω_{s1} , couple to the dipole transitions $|0\rangle \leftrightarrow |r\rangle$, $|0\rangle \leftrightarrow |s\rangle$, $|1\rangle \leftrightarrow |r\rangle$, $|1\rangle \leftrightarrow |s\rangle$ with Rabi frequencies Ω_{r0} , Ω_{s0} , Ω_{r1} , and Ω_{s1} , respectively. The corresponding Hamiltonian describing the laser mediated dipole transitions in the rotating wave approximation reads

$$H_{\text{las}} = \frac{1}{2} \sum_{j=1}^N (\Omega_{r0} e^{-i(\omega_{r0}t - k_{r0}x_j)} |r_j\rangle\langle 0_j| + \Omega_{s1} e^{-i(\omega_{s1}t - k_{s1}x_j)} |s_j\rangle\langle 1_j| + \Omega_{r1} e^{-i(\omega_{r1}t - k_{r1}x_j)} |r_j\rangle\langle 1_j| + \Omega_{s0} e^{-i(\omega_{s0}t - k_{s0}x_j)} |s_j\rangle\langle 0_j| + \text{H.c.}), \quad (4.4)$$

²Note that we expect no collective spontaneous emission effects because the atoms are situated far apart so that emitted photons are immediately lost to the environment and are unable to re-excite another atom.

where k_{mn} ($m \in \{r, s\}$, $n \in \{0, 1\}$) denote the wave numbers of the laser fields.

The cavity field a couples to the transitions $|0\rangle \leftrightarrow |r\rangle$ and $|1\rangle \leftrightarrow |s\rangle$ with coupling strengths g_{r0} and g_{s1} , respectively, while cavity field b , couples to the transitions $|0\rangle \leftrightarrow |s\rangle$ and $|1\rangle \leftrightarrow |r\rangle$ with coupling strengths g_{s0} and g_{r1} , respectively. The corresponding Hamiltonian describing the cavity mediated dipole transitions in the rotating wave approximation reads

$$H_{\text{int}} = \sum_{j=1}^N \left\{ (g_{r0}|r_j\rangle\langle 0_j| + g_{s1}|s_j\rangle\langle 1_j|) a e^{ik_a x_j} + (g_{r1}|r_j\rangle\langle 1_j| + g_{s0}|s_j\rangle\langle 0_j|) b e^{ik_b x_j} + \text{H.c.} \right\}, \quad (4.5)$$

where $\{k_a, k_b\}$ denote the wave numbers of the cavity fields. Note that the wave numbers of all the laser and cavity fields will be assumed to be essentially equal.

4.4 Microscopic Atom-Cavity Model

Finally the microscopic master equation describing the total atom-cavity system, including dissipation, is given by

$$\dot{\rho}_{\text{m}} = -i[H_{\text{m}}, \rho_{\text{m}}] + \mathcal{L}_{\text{c}}\rho_{\text{m}}, \quad (4.6)$$

where

$$H_{\text{m}} = H_{\text{at}} + H_{\text{c}} + H_{\text{las}} + H_{\text{int}}. \quad (4.7)$$

This master equation is in fact the starting point for the derivation of the effective spin-cavity system in section 3.2.1, where the atomic excited states have been adiabatically eliminated.

CHAPTER 5

ADIABATIC ELIMINATION OF THE CAVITY MODES

In this chapter we give a more detailed description of the adiabatic elimination of the cavity modes, which was used in the previous two chapters to obtain an effective collective spin system from the total coupled atom-cavity system. We consider a situation where the dynamics of both cavity modes occurs on a much faster time scale than that of the spin system, either due to strong losses or large effective frequency (detuning) of the cavity modes, and thus adiabatically follows the dynamics of the collective spin. It is then possible to seek a description of a reduced system involving only the collective spin by calculating the effect of the (weak) coupling to the cavity mode via perturbation theory and using the Born-Markov approximation [1–3]. We begin by giving the formal reduced system master equation in terms of the total atom-cavity system in section 5.1. In the following section 5.2 we show (i) why the non-linear dispersive terms do not contribute after the adiabatic elimination and (ii) why the adiabatic elimination of each cavity mode can be considered separately. After these two simplifications, in section 5.3 we sketch the technical aspects of the adiabatic elimination based on the correlation functions of the cavity modes (and the Born-Markov approximation).

5.1 Reduced System

Our starting point for the adiabatic elimination of the cavity modes is the master equation of the atom-cavity system (see section 3.2.1)

$$\dot{\rho}_g = -i[H_0 + H_1 + H_{\text{int}}, \rho_g] + \mathcal{L}_c \rho_g, \quad (5.1)$$

where

$$\mathcal{L}_c \rho_g = \kappa_a(2a\rho_g a^\dagger - a^\dagger a \rho_g - \rho_g a^\dagger a) + \kappa_b(2b\rho_g b^\dagger - b^\dagger b \rho_g - \rho_g b^\dagger b), \quad (5.2)$$

$$H_0 = \omega_0 J_z + \delta_a a^\dagger a + \delta_b b^\dagger b, \quad (5.3)$$

$$H_1 = 2\delta_a^- J_z a^\dagger a + 2\delta_b^- J_z b^\dagger b, \quad (5.4)$$

$$H_{\text{int}} = \frac{\lambda_a}{\sqrt{N}}(X_a a + X_a^\dagger a^\dagger) + \frac{\lambda_b}{\sqrt{N}}(X_b b + X_b^\dagger b^\dagger). \quad (5.5)$$

We now pursue a description of the atomic system alone, i.e., of $\rho_s \equiv \text{Tr}_c\{\rho_g\}$ where Tr_c indicates the trace over both cavity modes. This will be meaningful whenever the cavity mode dynamics occur on a much faster time scale than the spin system dynamics. For the open cavity system considered here this can occur either because the cavity detuning or dissipation strength are large compared to the atomic system energy scales, i.e., $\delta_i, \kappa_i \gg \omega_0, \lambda_i$. Then using the Born-Markov approximation we derive to second order (in the interaction strength) the following master equation for reduced atomic/collective spin density operator in the interaction picture ¹

$$\dot{\tilde{\rho}}_s(t) = - \int_0^t \text{Tr}_c \left\{ [(\tilde{H}_{\text{int}}(t) + H_1), e^{(t-t')\mathcal{L}_c}[(\tilde{H}_{\text{int}}(t') + H_1), \tilde{\rho}_s(t) \otimes \rho_c]] \right\} dt', \quad (5.6)$$

where $\tilde{\rho}_s(t) = U(t)^\dagger \rho_s(t) U(t)$ and $\tilde{H}_{\text{int}}(t) = U^\dagger(t) H_{\text{int}} U(t)$ with $U(t) = e^{-itH_0}$; note that $\tilde{H}_1(t) = U^\dagger(t) H_1 U(t) = H_1$. ρ_c denotes the total cavity mode density matrix given by $\rho_c = \rho_a \otimes \rho_b$ where $\rho_{a,b}$ are the density matrices for the individual cavity modes a, b , respectively. In what follows we assume a vacuum for each of the cavity modes, i.e., $\rho_{a,b} = |0\rangle_{a,b}\langle 0|_{a,b}$ where $|n\rangle_{a,b}$ are the Fock states for the cavity modes a, b . This assumption is a consequence of the large cavity detuning or dissipation, which ensures that the cavity modes are only ever very weakly (or virtually) excited.

5.2 Dispersive and Cross-Cavity Terms

First we show in more detail why the non-linear terms of H_1 do not contribute provided we consider a vacuum state for both cavity modes as explained above. First we see that the term $e^{(t-t')\mathcal{L}_c}[H_1, \tilde{\rho}_s \otimes \rho_c] = 0$ because $H_1 \rho_c = 0 = \rho_c H_1$. To see that the term $H_1 e^{(t-t')\mathcal{L}_c}[\tilde{H}_{\text{int}}, \tilde{\rho}_s \otimes \rho_c]$ also vanishes we note that $H_1 e^{(t-t')\mathcal{L}_c} A_c \rho_c$, where $A_c \in \{a, a^\dagger, b, b^\dagger\}$ always contains an odd number of bosonic operators (annihilation or creation) and therefore when the trace is performed with ρ_c being a vacuum state the result will always be zero.

Next we explain why the adiabatic elimination of each cavity mode may be performed independently provided we again consider a vacuum state for both cavity modes. We note that when the double commutator is expanded we obtain (i) terms only containing operators of cavity mode a or b and (ii) terms containing operators of both cavity mode a and b . Since the two cavity modes are orthogonal any expectation values involving both cavity modes factorize i.e. $\text{Tr}_c\{A_a A_b \rho_c\} = \text{Tr}_a\{A_a \rho_a\} \text{Tr}_b\{A_b \rho_b\}$ (where $A_a \in \{a, a^\dagger\}$ and $A_b \in \{b, b^\dagger\}$) and since we assumed a vacuum state for each cavity mode these terms give zero contribution.

¹This is derived using the method of projectors and the Laplace transform and is in fact a generalization of the result presented in [1]

5.3 Cavity Correlation Functions and Born-Markov Approximation

Thus we can express the master equation now as

$$\dot{\tilde{\rho}}_s(t) = - \int_0^t \sum_{i \in \{a,b\}} \text{Tr}_i \left\{ [H_i(t), e^{(t-t')\mathcal{L}_c} [H_i(t'), \tilde{\rho}_s(t) \otimes \rho_i]] \right\} dt', \quad (5.7)$$

where for convenience we have defined $H_a(t) = \frac{\lambda_a}{\sqrt{N}}(X_a(t)e^{-i\delta_a t}a + X_a(t)^\dagger e^{i\delta_a t}a^\dagger)$ and $H_b(t) = \frac{\lambda_b}{\sqrt{N}}(X_b(t)e^{-i\delta_b t}b + X_b(t)^\dagger e^{i\delta_b t}b^\dagger)$ with $X_i(t) = e^{-i\omega_0 t}X_i$. Upon expanding the above double commutator we only consider terms containing an annihilation *and* creation operator as all other combinations give zero contribution for a vacuum state. Thus we need only consider the four different non-trivial correlation functions that occur; for cavity mode a they are given by

$$\begin{aligned} \text{Tr}_a \{ a e^{(t-t')\mathcal{L}_c} (a^\dagger \rho_c) \} &= e^{-\kappa_a(t-t')} = \text{Tr}_a \{ a^\dagger e^{(t-t')\mathcal{L}_c} (\rho_c a) \} \\ \text{Tr}_a \{ a^\dagger e^{(t-t')\mathcal{L}_c} (a \rho_c) \} &= 0 = \text{Tr}_a \{ a e^{(t-t')\mathcal{L}_c} (\rho_c a^\dagger) \}. \end{aligned}$$

Identical results are obtained for cavity mode b with $a \rightarrow b$ in every term of the above equations.

Substituting the above results for the correlation functions into the reduced master equation (5.7) gives

$$\begin{aligned} \dot{\tilde{\rho}}_s(t) = & - \int_0^t \sum_{i \in \{a,b\}} \frac{\lambda_i^2}{N} \left\{ e^{-(t-t')(\delta_i + \kappa_i)} [X_i(t), X_i^\dagger(t') \tilde{\rho}_s(t)] \right. \\ & \left. - e^{-(t-t')(-i\delta_i + \kappa_i)} [X_i^\dagger(t), \tilde{\rho}_s(t) X_i(t')] \right\} dt'. \end{aligned} \quad (5.8)$$

To be consistent with the Markov approximation we must set $X_i^\dagger(t') \rightarrow X_i^\dagger(t)$ and $X_i(t') \rightarrow X_i(t)$ since $X_i(t)$ are system operators which change on the slow time scale according to $\tilde{\rho}_s(t)$. Then we can explicitly perform the integration, making the usual assumption of fast decaying correlations (setting $t \rightarrow \infty$), which gives the result

$$\int_0^t e^{-(\kappa_i \pm i\delta_i)(t-t')} dt' = \frac{1}{\kappa_i \pm i\delta_i} (1 - e^{-(\kappa_i \pm i\delta_i)t}) \xrightarrow{t \rightarrow \infty} \frac{1}{\kappa_i \pm i\delta_i}. \quad (5.9)$$

Using this result in Eq. (5.8) and transforming the resulting master equation back from the interaction picture gives the result Eq. (3.9) in section 3.2.2.

Bibliography

- [1] C. W. Gardiner and P. Zoller, *Quantum Noise* (Springer-Verlag, Berlin, 1992).
- [2] H. J. Carmichael, *Methods in Quantum Optics 2* (Springer-Verlag, Berlin, 2007).
- [3] J. I. Cirac, R. Blatt, P. Zoller, and W. D. Phillips, Phys. Rev. A, **46** 2668 (1992).

CHAPTER 6

PUBLICATION

Dissipation-driven quantum phase transitions in collective spin systems

arXiv:0805.1256 (2008)

S. Morrison^{1,2} and A. S. Parkins³

1) Institute for Theoretical Physics, University of Innsbruck, Innsbruck A-6020, Austria

2) Institute for Quantum Optics and Quantum Information of the Austrian Academy of Sciences, A-6020 Innsbruck, Austria

3) Department of Physics, University of Auckland, Private Bag 92019, Auckland, New Zealand

We consider two different collective spin systems subjected to strong dissipation – on the same scale as interaction strengths and external fields – and show that either continuous or discontinuous dissipative quantum phase transitions can occur as the dissipation strength is varied. First, we consider a well known model of cooperative resonance fluorescence that can exhibit a second-order quantum phase transition, and analyze the entanglement properties near the critical point. Next, we examine a dissipative version of the Lipkin-Meshkov-Glick interacting collective spin model, where we find that either first- or second-order quantum phase transitions can occur, depending only on the ratio of the interaction and external field parameters. We give detailed results and interpretation for the steady-state entanglement in the vicinity of the critical point, where it reaches a maximum. For the first-order transition we find that the semiclassical steady states exhibit a region of bistability and we show that homodyne spectra of the system provide a clear signature of this behavior.

6.1 Introduction

The field of ultracold quantum gases has recently made remarkable progress toward the implementation of (fully) tunable interacting many-body quantum systems [1]. Specifically, the degree of control in experiments allows for a precise variation of system parameters, for example interaction strengths and effective fields, such that the systems can be made to undergo transitions between different quantum phases [2].

Of particular interest are microscopic, interacting many-body systems, which have been widely studied in the context of closed systems, where quantum phase transitions (QPTs) arise due to the competition between fluctuations originating from different coherent processes in a system (e.g. tunneling versus interaction in the Bose-Hubbard Model) [3, 4]. Although individual systems subjected to dissipation on the same scale as their characteristic frequency have been extensively studied [5], the effects of dissipation on interacting many-body systems are less well-known. Recently a collective spin system with weak dissipation was studied in the context of a nonequilibrium QPT [6]. It was shown that the well known second-order phase transition found in the equivalent closed system persists, with weak dissipation being responsible only for minor modifications to the system properties. However, in addition, a first-order phase transition was shown to occur exclusively due to the presence of dissipation, i.e., this phase transition is absent in the equivalent closed system case. For both types of transition, the spin-spin entanglement was shown to exhibit pronounced signatures of the criticality.

Given these nontrivial results for the case of weak dissipation, it is then naturally interesting to consider the regime of strong dissipation, i.e., dissipative rates on the same scale as the interaction strengths and external fields. In this regime marked differences are expected in comparison to the closed system case, and, specifically, new types of QPTs, driven by the dissipation, are expected to emerge [7–13]. In this work we consider two models of open collective spin systems where a QPT arises solely due to a competition between fluctuations associated with Hamiltonian (coherent) dynamics and with dissipative processes. In addition to studying elementary characteristics of the phase transitions, we also study entanglement criticality and find that pronounced maxima in entanglement measures occur at the QPT. A further interesting feature that arises in the present work is that, for the second model considered, the nature of the phase transition, i.e., whether it is continuous or discontinuous, is governed by the *ratio* of the spin-spin interaction strength to the effective (“magnetic”) field. This behavior is in strong contrast to the equivalent nondissipative models, where the character of the phase transition is governed by the nature of the interaction, i.e., by whether it is “ferromagnetic” or “anti-ferromagnetic”. We also find in the latter model that within a semiclassical analysis a region of bistability arises for the first-order QPT; in the fully quantum mechanical system with finite atom number, N , signatures of this bistability can be identified in an atomic phase space distribution and in homodyne spectra. We note that bistable behavior and first-order nonequilibrium phase transitions have also been found in studies of optical bistability and resonance fluorescence of cooperative

atomic systems [11, 14, 15]. However, unlike these systems, our second model involves direct spin-spin interaction terms and does not feature coherent driving of the collective atomic spin.

A brief outline of the paper is as follows. First, in Sec. 6.2 we briefly examine the cooperative resonance fluorescence model, which exhibits a second-order QPT as the dissipation strength is varied, and consider the steady-state entanglement. Then, in Sec. 6.3 we focus on the dissipative Lipkin-Meshkov-Glick (LMG) model in a parameter regime where a second-order dissipation-driven QPT arises. Specifically we first present a semiclassical analysis of the phase transition and then consider the steady-state entanglement behavior across the phase transition. Next in Sec. 6.4 we present a similar analysis for a different parameter regime where a first-order dissipation-driven QPT occurs in the LMG model which in fact exhibits bistable behavior in the semiclassical steady states that can be further elucidated by considering homodyne spectra for finite N . Finally in Sec. 6.5 we will summarize our findings and give a brief outlook.

6.2 Cooperative Resonance Fluorescence Model

We consider here a model for cooperative resonance fluorescence as studied in [11–13], which describes a collection of N two-level atoms that are resonantly driven by a classical laser field and undergo collective spontaneous emission. This system can be described by the following (zero-temperature) master equation,

$$\dot{\rho} = -i[\Omega J_x, \rho] + \frac{\gamma}{N} (2J_- \rho J_+ - J_+ J_- \rho - \rho J_+ J_-), \quad (6.1)$$

where Ω is the strength of the coherent driving field and γ is the collective spontaneous emission rate (i.e., γ is proportional to the atomic density) [16]. The angular momentum operators are defined in terms of the individual two level operators by $J_z = (1/2) \sum_i \sigma_z^{(i)}$, $J_{\pm} = \sum_i \sigma_{\pm}^{(i)}$, with $\sigma_{\alpha}^{(i)}$ the Pauli matrices for atomic spin i , and $J_x = (1/2)(J_+ + J_-)$, $J_y = (-i/2)(J_+ - J_-)$. We note that this master equation possesses the exact steady-state solution [17, 18],

$$\rho_{\text{ss}} = \tilde{J}_-^{-1} \tilde{J}_+^{-1}, \quad (6.2)$$

where $\tilde{J}_{\pm} = J_{\pm} \mp i\Omega N/(2\gamma)$.

For a potential experimental realization of this system, we have in mind an ensemble of atoms coupled collectively to an optical (quantized) cavity mode and laser fields, which together drive Raman transitions between a pair of stable atomic ground states in a Λ -type configuration (similar to the setups described in [6] and [19]). In particular, a pair of laser fields drive a resonant Raman transition between the atomic ground states to provide the coherent driving term in Eq. (6.1), while the cavity mode and another laser field drive a second, distinct Raman transition. In the (“bad cavity”)

limit where the cavity field decay rate is much larger than the Raman transition rates, the cavity mode dynamics adiabatically follows the atomic dynamics and can therefore be eliminated from the model [6], yielding the dissipative term proportional to γ in Eq. (6.1), with γ the effective (cavity-mediated) collective atomic spontaneous emission rate. Also note that in such a setup the dissipative term automatically scales with a factor of $1/N$ (in contrast to earlier studies [13]), which allows the thermodynamic limit to be identified more readily and ensures that the critical point is independent of the system size N in this limit.

In Sec. 6.2.1 we first study the steady-state solutions of the cooperative resonance fluorescence model. Then in Sec. 6.2.2 we determine and analyze the steady-state entanglement present in the system.

6.2.1 Steady-states

From the above master equation we derive the following semiclassical equations of motion for the components of the Bloch vector, $X = \langle J_x \rangle / j$, $Y = \langle J_y \rangle / j$, and $Z = \langle J_z \rangle / j$ (see [6] and [19] for similar derivations)

$$\dot{X} = \gamma ZX, \quad (6.3a)$$

$$\dot{Y} = -\Omega Z + \gamma ZY, \quad (6.3b)$$

$$\dot{Z} = \Omega Y - \gamma(X^2 + Y^2), \quad (6.3c)$$

with the constraint $X^2 + Y^2 + Z^2 = 1$ corresponding to conservation of angular momentum. For $\gamma > \gamma_c \equiv \Omega$, the stable steady-state solutions are given by

$$Z_{ss} = -\sqrt{1 - \Omega^2/\gamma^2}, \quad (6.4a)$$

$$X_{ss} = 0, \quad (6.4b)$$

$$Y_{ss} = \Omega/\gamma. \quad (6.4c)$$

When $\gamma < \gamma_c$ one finds that *no* (semiclassical) steady-state solutions exists. However, the (finite- N) master equation has a stable steady-state solution for all γ , as given by Eq. (6.2), which indicates that quantum fluctuations play a crucial role in determining the state of this model. This was extensively discussed in earlier works [11, 12], where an effective description for $N \gg 1$ was developed and the steady-state Bloch vector components for $\gamma < \gamma_c$ were shown to be

$$Z_{ss} = 0, \quad (6.5a)$$

$$X_{ss} = 0, \quad (6.5b)$$

$$Y_{ss} = \frac{\Omega}{\gamma} - \frac{\sqrt{1 - (\Omega/\gamma)^2}}{\sin^{-1}(\gamma/\Omega)}. \quad (6.5c)$$

In Fig. 6.1 we plot the nonvanishing steady-state Bloch vector components, as given by the above expressions, together with finite- N solutions (computed from numerical solution of the master equation [20]) for comparison. We see that there is good agreement for sufficiently large values of N (in fact, the two approaches are already in reasonable agreement for $N \simeq 100$). Also, in Fig. 6.2 we plot finite- N solutions for the steady-state second-order moments, $\langle J_x^2 \rangle / j^2$, $\langle J_y^2 \rangle / j^2$, and $\langle J_z^2 \rangle / j^2$.

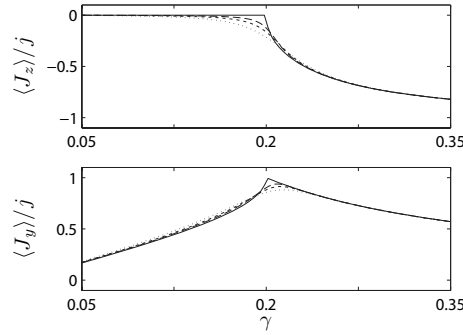


Figure 6.1. Semiclassical and asymptotic solutions (solid line), and finite- N steady-state moments for $\Omega = 0.2$, and $N = 25$ (dotted line), 50 (short dashed line), 100 (long dashed line).

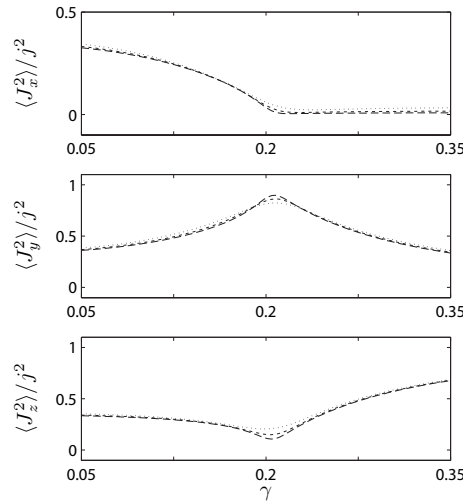


Figure 6.2. Finite- N steady-state second-order moments for $\Omega = 0.2$, and $N = 25$ (dotted line), 50 (short dashed line), 100 (long dashed line).

6.2.2 Entanglement

We consider bipartite entanglement between individual atomic spins, as quantified by the rescaled concurrence, $C_R = (N - 1)C$, with C the concurrence [21], and by the phase-dependent measure $\max\{0, C_\varphi\}$ [22], where

$$C_\varphi \equiv 1 - \frac{4}{N} \langle \Delta J_\varphi^2 \rangle - \frac{4}{N^2} \langle J_\varphi \rangle^2, \quad (6.6)$$

with $J_\varphi = \sin(\varphi)J_x + \cos(\varphi)J_y$. Note that in Ref. [6] the rescaled concurrence was found to be related to C_φ through the relation $C_R = \max_\varphi C_\varphi$. For our proposed realization of the model, the latter entanglement measure can in principle be determined from appropriate (quadrature variance) measurements performed on the cavity output field as explained in [6]. In the present model we find that the relation $C_R = \max_\varphi C_\varphi$ also holds, which then, indirectly, enables a measurement of the rescaled concurrence.

In Fig. 6.3 we plot the rescaled concurrence as a function of the dissipation strength γ for $N = 100$ as calculated numerically from the master equation (6.1). We can see that the entanglement peaks close to the critical point and then very rapidly diminishes to zero below the critical point, in agreement with a previous study [13]. This behavior can be understood by considering the entanglement measure $\max\{0, C_\varphi\}$ as a function of the phase φ and the dissipation strength γ . We find that above the transition, $\gamma > \gamma_c$, C_φ is nonzero for a broad range of φ around $\varphi = \pi/2$. However, below the transition C_φ is zero for all φ and γ as both the mean values and fluctuations of the components of the Bloch vector, i.e., $\langle J_\alpha \rangle^2/j^2$ and $\langle J_\alpha^2 \rangle/j^2$, scale as $j^2 = N^2/4$ (see Fig. 6.1 and Fig. 6.2). By using the exact steady-state solution, given in Eq. (6.2), we are able to calculate the rescaled concurrence for large values of N . However, in the limit of large γ we run into numerical difficulties and thus we will consider here only the behavior near the critical point. In the inset of Fig. 6.3 we show the behavior of $\max(C_R)$ as a function of N in the vicinity of the critical point (since at finite N the critical point depends upon N it would be meaningless to consider a fixed value of γ). We see that $\max(C_R)$ continues to increase with N and appears to approach the asymptotic value of 1 (viz. the corresponding thermodynamic limit value, see below) with an approximately logarithmic scaling in N .

In the present context it is also useful to consider a phase space representation of the steady state as given by the spin Q -function,

$$Q_s(\eta) = \langle \eta | \rho | \eta \rangle, \quad (6.7)$$

where $|\eta\rangle$ are the atomic coherent states defined by

$$|\eta\rangle = (1 + |\eta|^2)^{-j} \sum_{m=-j}^j \sqrt{\binom{N}{j+m}} \eta^{j+m} |j, m\rangle_j, \quad (6.8)$$

with $\eta = e^{i\phi} \tan \frac{\theta}{2}$, where θ and ϕ correspond to spherical coordinates, and $|j, m\rangle$ are the Dicke states with $m \in [-j, -j+1, \dots, j-1, j]$ (for our system, $j = N/2$).

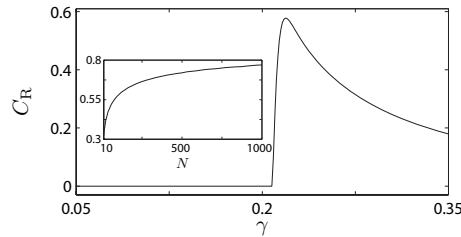


Figure 6.3. *Rescaled concurrence C_R for $N = 100$ and $\Omega = 0.2$. Inset: Asymptotic behavior of $\max(C_R)$ as a function of N for $\Omega = 0.2$ in the vicinity of the critical point.*

In Fig. 6.4 the spin Q -function, $Q_s(\eta)$, is shown on the Bloch sphere for four different values of γ . We see that above the transition point $Q_s(\eta)$ is a symmetric, single-peaked function centered at the corresponding semiclassical amplitude. As the critical point is approached $Q_s(\eta)$ stretches and moves down to the equatorial plane. However, once below the transition point $Q_s(\eta)$ remains centered at $\theta = \pi/2$ for all γ and merely continues to spread out in size as the fluctuations increase. Eventually, as $\gamma \rightarrow 0$, $Q_s(\eta)$ covers the entire Bloch sphere, in agreement with the fluctuations becoming evenly distributed in the x , y and z directions (see Fig. 6.2).

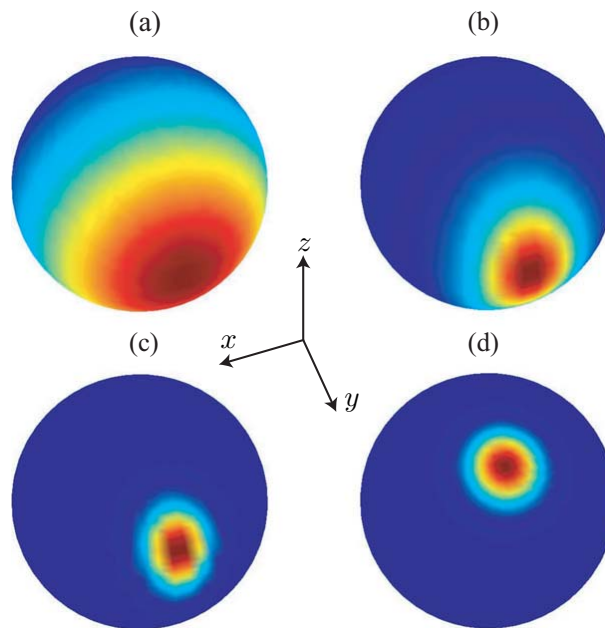


Figure 6.4. *(Color online) Steady-state spin Q -function, $Q_s(\eta)$, on the Bloch sphere for (a) $\gamma = 0.05$, (b) $\gamma = 0.15$, (c) $\gamma = 0.225$, (d) $\gamma = 0.5$, with $N = 50$ and $\Omega = 0.2$. Note that dark blue corresponds to the minimum value of zero of $Q_s(\eta)$ while dark red indicates the maximum value of $Q_s(\eta)$.*

Next, we consider the thermodynamic limit by linearizing the quantum fluctuations around the steady-state solution using the Holstein-Primakov (HP) representation [23]. We note that, as follows from the above discussion of the steady-state representation in phase space, the linearization is only possible for $\gamma > \gamma_c$, since below the critical point the state can no longer be described in terms of fluctuations centered around a semiclassical steady-state solution on the Bloch sphere. However, above the critical point we can easily obtain the linearized master equation by expanding the angular momentum operators around the semiclassical steady-state solution using the HP representation [23], which gives

$$\begin{aligned} \dot{\rho} = & \frac{\gamma}{4} \left(1 - \sqrt{1 - \frac{\Omega}{\gamma}}\right)^2 D[c^\dagger]\rho + \frac{\gamma}{4} \left(1 + \sqrt{1 - \frac{\Omega}{\gamma}}\right)^2 D[c]\rho \\ & + \frac{\Omega^2}{4\gamma} (2c\rho c + 2c^\dagger\rho c^\dagger - \{c^2 + (c^\dagger)^2, \rho\}), \end{aligned} \quad (6.9)$$

where c and c^\dagger are bosonic annihilation and creation operators, respectively. Using this master equation, it is straightforward to compute the rescaled concurrence analytically and we find

$$C_R = 1 - \sqrt{1 - \Omega^2/\gamma^2}. \quad (6.10)$$

Away from the critical point this is in good agreement with the results shown for $N = 100$ in Fig. 6.3, whilst near the critical point the agreement between the finite- N and linearized results improves with increasing system size N , as shown in the inset of Fig. 6.3.

6.3 Second-Order Transition in Dissipative LMG Model

We now turn to the dissipative LMG model, first studied in [6], which describes a collection of N interacting two-level systems in the presence of (collective) dissipation. Specifically, as shown in [6], by considering an ensemble of atoms coupled collectively to optical cavity and coherent laser fields, with suitably tailored Raman transitions between a pair of atomic ground states, one may realize a dynamics described by the master equation

$$\dot{\rho} = -i[H_{\text{LMG}}, \rho] + \frac{\Gamma_a}{N} D[2J_x]\rho + \frac{\Gamma_b}{N} D[J_+]\rho, \quad (6.11)$$

where Γ_a and Γ_b are tunable dissipation strengths, and the Hamiltonian is given by

$$H_{\text{LMG}} = -2hJ_z - \frac{2\lambda}{N} J_x^2, \quad (6.12)$$

with h and λ tunable effective field and interaction strengths, respectively. Note that we have expressed the dissipative terms in the above master equation (6.11) using the convention $D[A]\rho = 2A\rho A^\dagger - A^\dagger A\rho - \rho A^\dagger A$.

In this section we will study this model in the regime $\lambda < 2h$, where a second-order phase transition occurs. In Sec. 6.3.1 we analyze the steady states and nonlinear dynamics of the semiclassical equations of motion. Then in Sec. 6.3.2 we determine the steady-state entanglement in the system.

6.3.1 Semiclassical analysis

Steady-state solutions

The semiclassical equations of motion for the components of the Bloch vector, $X = \langle J_x \rangle / j$, $Y = \langle J_y \rangle / j$, $Z = \langle J_z \rangle / j$, where $j = N/2$, derived from the above master equation, are given by [6]

$$\dot{X} = 2hY - \Gamma_b ZX, \quad (6.13a)$$

$$\dot{Y} = -2hX + 2\lambda ZX - \Gamma_b ZY, \quad (6.13b)$$

$$\dot{Z} = -2\lambda XY + \Gamma_b(X^2 + Y^2), \quad (6.13c)$$

with the constraint $X^2 + Y^2 + Z^2 = 1$ corresponding to conservation of angular momentum.

The steady-state solutions of these equations of motion exhibit a bifurcation at a critical dissipation strength

$$\Gamma_b^c \equiv 2\sqrt{h(\lambda - h)}, \quad (6.14)$$

provided $\lambda > h$; also note that $\Gamma_b^c < \lambda$. For $\Gamma_b > \Gamma_b^c$ the stable steady-state solutions are

$$Z_{ss} = 1, \quad X_{ss} = Y_{ss} = 0, \quad (6.15)$$

whilst for $\Gamma_b < \Gamma_b^c$ they become

$$Z_{ss} = \frac{2h}{\Lambda}, \quad (6.16a)$$

$$X_{ss} = \pm \sqrt{\frac{\Lambda^2 - 4h^2}{2\lambda\Lambda}}, \quad (6.16b)$$

$$Y_{ss} = \frac{\Gamma_b}{2h} X_{ss} Z_{ss}, \quad (6.16c)$$

where

$$\Lambda = \lambda + \sqrt{\lambda^2 - \Gamma_b^2}. \quad (6.17)$$

From these expressions we can see that, in the present regime of $\lambda \leq 2h$, all the semiclassical steady-state solutions vary continuously across the phase transition corresponding to a second-order phase transition. In Fig. 6.5 we illustrate this bifurcation, where, to facilitate a comparison between semiclassical and finite- N solutions (computed from numerical solution of the master equation), we plot the second-order moments $\langle J_x^2 \rangle$ and $\langle J_y^2 \rangle$ (since the finite- N master equation gives $\langle J_x \rangle = \langle J_y \rangle = 0$ for all λ), and $\langle J_z \rangle$. We note that the two approaches are in reasonable qualitative agreement; we expect improved quantitative agreement for increasing N , but unfortunately we are computationally restricted from considering much larger system sizes. This should be compared to the results of the model in the previous Sec. 6.2, i.e., Fig. 6.1, where the convergence between finite- N and asymptotic results was much better. Note that since $\lambda \sim h$ a significant inversion of X_{ss} or Z_{ss} (as observed for the second-order transition presented in [6]) does not occur here for $\Gamma_b < \Gamma_b^c$.

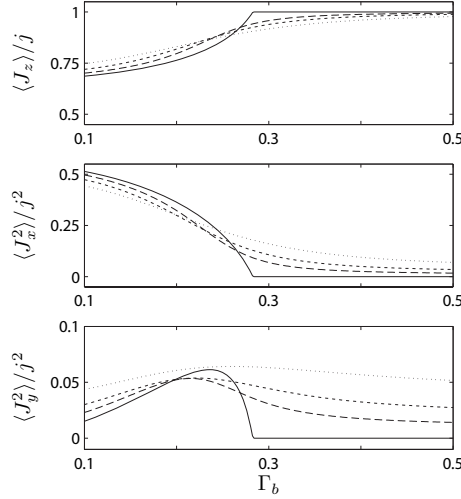


Figure 6.5. *Semiclassical (solid line) and finite- N steady-state second-order moments for $h = 0.2$, $\lambda = 0.3$, and $\Gamma_b^c = 0.28$, and $N = 25$ (dotted line), 50 (short dashed line), 100 (long dashed line).*

Next let us briefly consider the detailed stability analysis of the steady-state solutions, which can be readily determined by linearizing the above nonlinear equations of motions (6.13a)-(6.13c) around the steady-state solutions. The resulting linearized equations of motion can be expressed as $(\dot{X}, \dot{Y}, \dot{Z})^T = \mathbf{M}(X, Y, Z)^T + C$, where C is a (constant) three component vector, and we will consider the nontrivial eigenvalues, μ_{\pm} , of the 3×3 matrix \mathbf{M} (a trivial zero eigenvalue is always present due to the constant of the motion). Above the critical point, $\Gamma_b > \Gamma_b^c$, the eigenvalues of \mathbf{M} are purely real and given by

$$\mu_{\pm} = -\Gamma_b \pm \Gamma_b^c. \quad (6.18)$$

From this we see that the eigenvalues scale linearly with the dissipation (in contrast to the studies of our previous model [6]) with μ_+ going to zero at the critical point.

Below the critical point, $\Gamma_b < \Gamma_b^c$, the eigenvalues of \mathbf{M} are given by

$$\mu_{\pm} = -\frac{2\Gamma_b h}{\lambda + \sqrt{\lambda^2 - \Gamma_b^2}} \pm \sqrt{4h^2 + 2\Gamma_b^2 - 2\lambda^2 - 2\lambda\sqrt{\lambda^2 - \Gamma_b^2}}. \quad (6.19)$$

In the region $\Gamma_b'' < \Gamma_b < \Gamma_b^c$, where

$$\Gamma_b'' = \sqrt{\frac{\lambda^2 - 4h^2}{2} + \frac{\lambda}{2}\sqrt{\lambda^2 + 8h^2}}, \quad (6.20)$$

the eigenvalues are also purely real, with μ_+ going to zero at the critical point, whilst in the region $\Gamma_b < \Gamma_b'' < \Gamma_b^c$ they become complex conjugate pairs, with an imaginary part that goes to zero as $\sqrt{\Gamma_b'' - \Gamma_b}$. For our characteristic parameters of $h = 0.2$ and $\lambda = 0.3$ we find that $\Gamma_b'' = 0.25$ and $\Gamma_b^c = 0.28$, hence $\Gamma_b'' < \Gamma_b^c$. We note from the above expression that for the case $\lambda < 2h$ considered here, the eigenvalues vary smoothly across the critical point, as expected for a second-order phase transition.

Time-dependent solutions

Let us now consider numerical, time-dependent solutions of the semiclassical equations of motion, i.e., of Eqs. (6.13a)-(6.13a). We have calculated the evolution of the Bloch components $X(t)$, $Y(t)$, and $Z(t)$ numerically for a uniform distribution of different initial states on the Bloch sphere. The resulting trajectories $\{X(t), Y(t), Z(t)\}$ are mapped from the Bloch sphere into the plane using the sinusoidal projection [24]. This mapping is achieved in two steps. First, the solutions for the Bloch components are transformed into spherical polar angles $\theta(t)$ and $\phi(t)$. Next, the polar angles are transformed to new coordinates $U(t)$ and $V(t)$ via the transformation

$$U(t) = (\phi(t) - \pi) \cos(\theta(t) - \pi/2), \quad (6.21)$$

$$V(t) = \theta(t) - \pi/2. \quad (6.22)$$

In Fig. 6.6 we plot the trajectories using the sinusoidal projection for a value of Γ_b above the critical point (see the caption of Fig. 6.6 for numerical values of parameters). We can see that all initial states terminate in the unique steady state given by Eq. (6.15), corresponding to the point $U_{ss} = 0, V_{ss} = \pi/2$ in Fig. 6.6. Moreover we can see that all trajectories approach the stable steady state along one of two lines, corresponding to the stable steady state being a node (eigenvalues μ_{\pm} being purely real). Next, we consider the case where Γ_b is below the critical value and plot the trajectories using the sinusoidal projection in Fig. 6.7. In this case we see that different initial states terminate in either one of the two stable steady states given by Eqs. (6.16a)-(6.16c), the corresponding values for the points U_{ss}, V_{ss} are given in the caption of Fig. 6.7. We also note that none of the trajectories ever terminate at $U_{ss} = 0, V_{ss} = \pi/2$, corresponding to the steady state (6.15), since this solution is unstable in this regime. We can also see that the trajectories form spirals centered at the stable semiclassical steady states, corresponding to the eigenvalues being complex conjugate pairs (note that $\Gamma_b < \Gamma_b''$ for the choice of parameters in Fig. 6.6).

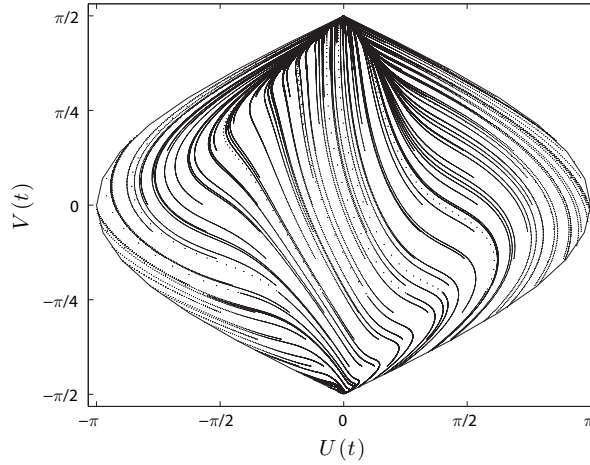


Figure 6.6. Trajectories for different initial conditions on the Bloch sphere using the sinusoidal projection, with $h = 0.2$, $\lambda = 0.3$, and $\Gamma_b = 0.45$.

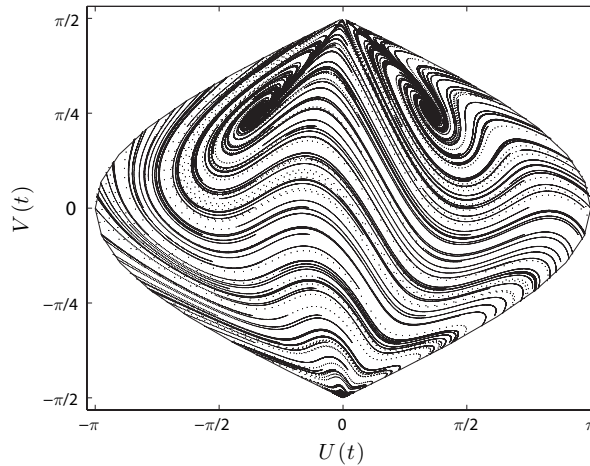


Figure 6.7. Trajectories for different initial conditions on the Bloch sphere using the sinusoidal projection, with $h = 0.2$, $\lambda = 0.3$, and $\Gamma_b = 0.15$. For this choice of parameters the stable steady states are located at $U_{ss} \simeq \pm 0.35\pi$, $V_{ss} \simeq 0.25\pi$ (as calculated from Eqs. (6.16a)-(6.16c)).

6.3.2 Entanglement

We consider as before the rescaled concurrence C_R and the phase dependent entanglement measure $\max\{0, C_\varphi\}$, both numerically for finite N and analytically in the thermodynamic limit. Note that in this model, for finite N and also in the linearized analysis, we have $\langle J_\varphi \rangle = 0$ (since there are no linear driving terms in the effective Hamiltonian (6.12) or the corresponding linearized Hamiltonian [6]), and thus $C_\varphi = 1 - (4/N)\langle J_\varphi^2 \rangle$. Again, we find that $C_R = \max_\varphi C_\varphi$, as for the above model and the model studied in [6].

In Fig. 6.8 (a) we plot $\max\{0, C_\varphi\}$ as a function of Γ_b and φ for $N = 100$ with parameters corresponding to the second-order phase transition. We see that well above the transition, $\Gamma_b > \Gamma_b^c$, entanglement is present for a broad range of angles φ . However, as the critical point is approached the range of angles φ which give nonzero entanglement, $C_\varphi > 0$, becomes increasingly narrow. Below the transition, $\Gamma_b < \Gamma_b^c$, the region of finite C_φ continues to narrow and its maximum simultaneously shifts toward $\varphi = 0$ as Γ_b decreases.

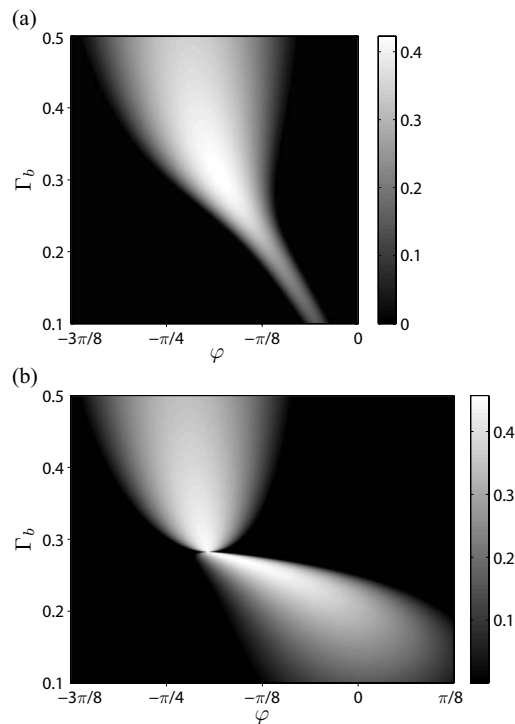


Figure 6.8. (a) Entanglement measure $\max\{0, C_\varphi\}$ for $N = 100$, $h = 0.2$, $\lambda = 0.3$, and $\Gamma_b^c = 0.28$. (b) Entanglement measure $\max\{0, C_\varphi\}$ in the thermodynamic limit, with $h = 0.2$, $\lambda = 0.3$, and $\Gamma_b^c = 0.28$.

This behavior can be explained by considering the spin Q -function. Figure 6.9 displays $Q_s(\eta)$ on the surface of the Bloch sphere for $N = 50$ and for a series of dissipation strengths Γ_b . Above the critical point $Q_s(\eta)$ is single-peaked and centered around the top of the Bloch sphere ($\theta = 0$), with a significant rotation in a direction between the x and y axes due to the large values of dissipation. Consequently we see that although C_φ is relatively broad above the transition, stemming from the broad shape of the lobe, its center (where it is maximal) is continually shifting toward smaller values of φ as the rotation of $Q_s(\eta)$ away from the x axis decreases with decreasing dissipation.

As Γ_b decreases towards the critical point, $Q_s(\eta)$ becomes increasingly elongated along a direction between the x and y axes, until, at the transition, it splits into two peaks located approximately at the two semiclassical steady-state amplitudes (6.16b) and (6.16c). These peaks continue to move apart in phase space as the dissipation strength is decreased further, approaching the corresponding dissipation-free points at $\theta = \pi/2$ and $\phi = 0, \pi$. Correspondingly, the range of φ over which C_φ remains finite becomes increasingly narrow and is focussed around an axis perpendicular to that along which the two peaks lie. This narrowing of the “width” of C_φ can be explained by noting that, since $\langle J_\varphi \rangle = 0$, we have $C_\varphi = 1 - (4/N)\langle [\sin(\varphi)J_x + \cos(\varphi)J_y]^2 \rangle$. For decreasing dissipation strength $\Gamma_b < \Gamma_b^c$, $\langle J_x^2 \rangle$ becomes of order $j^2 = N^2/4$ (see Fig. 6.5), and so the optimal choice of φ becomes more critical.

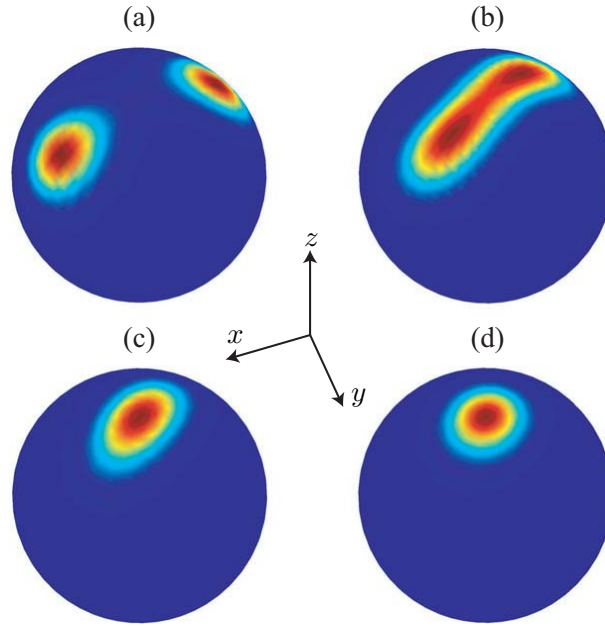


Figure 6.9. (Color online) Steady-state spin Q -function, $Q_s(\eta)$, on the Bloch sphere for (a) $\Gamma_b = 0.1$, (b) $\Gamma_b = 0.25$, (c) $\Gamma_b = 0.4$, and (d) $\Gamma_b = 1$, with $N = 50$, $h = 0.2$, $\lambda = 0.3$, and $\Gamma_b^c = 0.28$. Note that dark blue corresponds to the minimum value of zero of $Q_s(\eta)$ while dark red indicates the maximum value of $Q_s(\eta)$.

In Fig. 6.10 we plot the rescaled concurrence calculated for $N = 100$ (dashed line) and find that it peaks close to the critical point. In contrast to the model of the previous section, significant entanglement is present on both sides of the critical point.

We now consider the thermodynamic limit, where we can obtain analytic results for $N \gg 1$ by considering a linearized model. Using the Holstein Primakov representation [23] it is straightforward to linearize the master equation (6.11) around the stable semiclassical solutions (6.15) and (6.16a)-(6.16c). This basically involves replacing the spin ladder operators J_\pm by bosonic creation (annihilation) operators c_k^\dagger (c_k), where

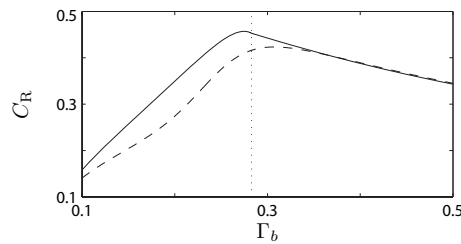


Figure 6.10. Rescaled concurrence C_R for $N = 100$ (dashed line), and the thermodynamic limit (solid line), with $h = 0.2$, $\lambda = 0.3$, and $\Gamma_b^c = 0.28$. The vertical dotted line indicates the location of the critical point $\Gamma_b^c = 0.28$.

$k \in \{<, >\}$ denotes below or above the critical point, representing the quantum fluctuations. Since we are not directly interested in the linearized master equation we will refrain from quoting it here and refer the reader to [6].

In Fig. 6.8(b) we display C_φ in the thermodynamic limit as a function of the dissipation strength Γ_b and the phase angle φ . We observe that above the transition, $\Gamma_b > \Gamma_b^c$, the behavior is very similar to the finite- N result of Fig. 6.8(a). However, the behavior below the critical point, $\Gamma_b < \Gamma_b^c$, is very different, with C_φ nonzero for a broad range of φ due to the linearized treatment, which only accounts for fluctuations around one of the two semiclassical steady-state amplitudes (i.e., around one of the two lobes appearing in the spin Q -function for $\Gamma_b < \Gamma_b^c$). Note that we can obtain plots of $\max\{0, C_\varphi\}$ similar to Fig. 6.8(a) for the region $\Gamma_b < \Gamma_b^c$, but determined from the linearized HP model (with a finite value of N), by making a rotation back to the original coordinate system and then setting, by hand, $\langle \chi_\varphi \rangle = 0$, to mimic an equal, incoherent mixture of the states associated with the two semiclassical amplitudes.

Finally, in Fig. 6.10 we also plot C_R as computed in the thermodynamic limit (solid line) from the linearized master equation [6]. We observe that in the linearized regime the peak of the concurrence is shifted *below* the critical point, whilst at the critical point there is a marked change in the behavior. However, we can once again recover a curve within the linearized HP model that is more similar to the finite- N result for $\Gamma_b < \Gamma_b^c$ by following the procedure outlined at the end of the previous paragraph.

It is interesting to note that the difference in the behavior of $\max\{0, C_\varphi\}$ between the finite- N and thermodynamic limit is analogous to that observed in [6]. However, in [6] the rescaled concurrence peaked at the critical point for both the finite- N calculations and the thermodynamic limit. Thus, unfortunately, the result for $\max\{0, C_\varphi\}$ in the thermodynamic limit does not give us any clues to the discrepancy observed in the rescaled concurrence.

6.4 First-Order Transition in Dissipative LMG Model

In this section we consider the dissipative LMG model described by the master equation (6.11) in the regime $\lambda > 2h$, where we find that a discontinuous first-order transition occurs. Moreover, we find that there are in fact two transition points that encompass a region of bistability, the size of which increases with increasing λ . In Sec. 6.3.1 we analyze the steady states and nonlinear dynamics of the semiclassical equations of motion. Then in Sec. 6.3.2 we determine the steady-state entanglement in the system.

6.4.1 Semiclassical analysis

Steady-state solutions

We consider, as previously, the semiclassical equations of motion given by Eqs. (6.13a)-(6.13c) and begin by studying their steady-state solutions. In the region $\Gamma_b > \lambda$ the stable steady-state solutions are given by Eq. (6.15), whilst for $\Gamma_b < \Gamma_b^c$ they are given by Eqs. (6.16a)-(6.16c). However, in the region $\Gamma_b^c < \Gamma_b < \lambda$ *both* steady-state solutions (6.15) and (6.16a)-(6.16c) are in fact stable, i.e., the semiclassical system is bistable [25]. These two solutions each exhibit a discontinuity, associated with a first-order phase transition, at the critical points Γ_b^c and λ , respectively. Note that for values of λ not significantly larger than $2h$, the bistable region is in fact very small, with $\Gamma_b^c \simeq \lambda$, and consequently the distinction between steady states in this region becomes somewhat redundant [6]. However, in the regime $\lambda \gg 2h$ the extent of the bistable region becomes significant and both stable steady states must be considered. In fact, in this situation we can expect that a complete description in terms of a single steady state will not be possible. We will focus on the regime of large λ , and study the system primarily for the characteristic parameters $\{h = 0.2, \lambda = 0.75, \Gamma_a = 0.01\}$.

The behavior of the semiclassical steady-state solutions as a function of Γ_b is illustrated in Fig. 6.11, together with finite- N solutions. Outside the bistable region, convergence of the finite- N solutions towards the semiclassical results is evident, while inside the bistable region the finite- N solutions appear to approach the semiclassical branch corresponding to Eqs. (6.16a)-(6.16c), although the rate of convergence with increasing N is clearly much slower, and indeed the finite- N curves are suggestive of some degree of “averaging” between the distinct semiclassical steady states. (In fact, consideration of the spin Q -function later in this section will support this picture.)

At the critical points, the semiclassical moments “jump” by a larger amount as λ is increased; specifically the size of the jump at the critical points is quantified by $\Delta \equiv 1 - Z_{ss}$, where Z_{ss} is given by Eq. (6.16a). For the critical point Γ_b^c this is given

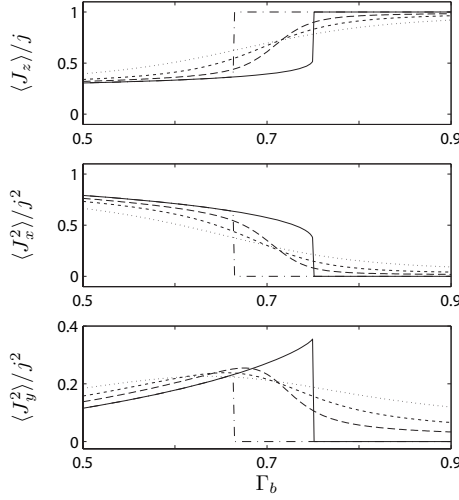


Figure 6.11. *Stable semiclassical solutions, (6.16a)-(6.16c) (solid line), and (6.15) (dash-dotted line), with $h = 0.2$, $\lambda = 0.75$, and $\Gamma_b^c = 0.66$. Also plotted are the finite- N steady-state moments for $N = 25$ (dotted line), 50 (short dashed line), 100 (long dashed line).*

by $\Delta = 1 - h/(\lambda - h)$ and for the critical point λ by $\Delta = 1 - 2h/\lambda$, hence we see that at either critical point the largest possible jump occurs in the limit $\lambda \gg h$.

Now let us again consider the stability of the steady-state solutions by examining the nontrivial eigenvalues μ_{\pm} of the matrix \mathbf{M} describing the linearized semiclassical equations of motion. For the steady-state solution (6.15), stable in the region $\Gamma_b^c < \Gamma_b$, the eigenvalues are again given by Eq. (6.18), whilst for the steady-state solutions (6.16a)-(6.16c), stable in the region $\Gamma_b < \lambda$, they are given by Eq. (6.19). We plot these eigenvalues in Fig. 6.12 and note the discontinuities in Eq. (6.18) and Eq. (6.19) at Γ_b^c and λ , respectively, as expected for a first-order transition. These discontinuities coincide with μ_+ , as given by Eq. (6.18), going to zero at Γ_b^c , and μ_+ , as given by Eq. (6.19), going to zero at λ .

In the bistable region the behavior of the eigenvalues associated with the steady states (6.16a)-(6.16c) is quite similar to that of the eigenvalues for $\Gamma_b < \Gamma_b^c$ for the second-order transition of Sec. 6.3. Note, however, that whilst for $\lambda < \frac{h}{2}(3 + \sqrt{5})$ (the case encountered previously in Sec. 6.3) one finds $\Gamma_b'' < \Gamma_b^c$, if $\lambda > \frac{h}{2}(3 + \sqrt{5})$ (corresponding to the case plotted in Fig. 6.12) we find that $\lambda > \Gamma_b'' > \Gamma_b^c$ (this was already noted in [6]).

Finally, over essentially all of the bistable region $\Gamma_b^c < \Gamma_b < \lambda$ we observe that the real part(s) of the eigenvalues associated with the solutions (6.16a)-(6.16c) are smaller (i.e., more negative) than the largest real part of the eigenvalues associated with the solutions (6.15). This points to the steady-state solutions (6.16a)-(6.16c) being more stable than the solutions (6.15) over the majority of the bistable region, which is consistent with the apparent convergence of the finite- N results with increasing N .

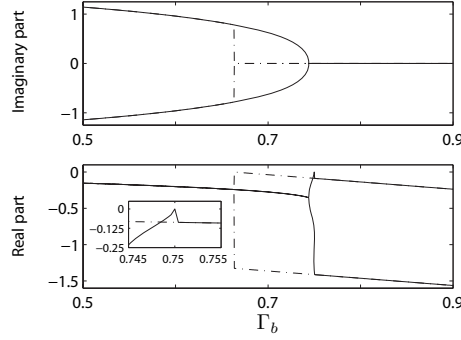


Figure 6.12. *Eigenvalues of the linearized equations of motion, μ_{\pm} , as given by Eq. (6.19) (solid line), and by Eq. (6.18) (dash-dotted line), for $h = 0.2$, $\lambda = 0.75$, and $\Gamma_b^c = 0.66$. The inset shows a magnification of the real part of μ_{\pm} near the critical point at $\Gamma_b = \lambda$.*

towards the solutions (6.16a)-(6.16c). We note, however, that for significantly larger values of λ , where the bistable region is much larger, either steady-state solution can be more stable depending on the choice of Γ_b within the bistable region, and thus a convergence of the finite- N results toward one of the two semiclassical solutions is not observed.

Time-dependent solutions

Time dependent solutions of the semiclassical equations of motion are now examined, again using the sinusoidal projection defined earlier. In particular, in Fig. 6.13 we plot trajectories $\{U(t), V(t)\}$ for a value of Γ_b within the bistable region $\Gamma_b^c < \Gamma_b < \lambda$ [26]. We see that, in this case, different initial states evolve to *either* the steady state (6.15), (corresponding to $U_{ss} = 0, V_{ss} = \pi/2$), *or* to either of the two steady states (6.16a)-(6.16c) (corresponding to $U_{ss} \simeq \pm 0.56\pi, V_{ss} \simeq 0.13\pi$). Again we see that the way in which the trajectories approach the respective steady states is directly related to the type of eigenvalue.

In Fig. 6.13 we note two distinct “gaps” centered at the points $\{U \simeq \pm 0.21\pi, V \simeq 0.31\pi\}$. These points in fact correspond to *unstable* steady-state solutions of the semiclassical equations of motion, given by

$$Z_{ss}^u = \frac{2h}{\Lambda'}, \quad X_{ss}^u = \pm \sqrt{\frac{\Lambda'^2 - 4h^2}{2\lambda\Lambda'}}, \quad Y_{ss}^u = \frac{\Gamma_b}{2h} X_{ss}^u Z_{ss}^u, \quad (6.23)$$

where $\Lambda' = \lambda - \sqrt{\lambda^2 - \Gamma_b^2}$. These points separate trajectories that terminate in different (stable) steady states, i.e., trajectories that pass “above” (“below”) these points terminate in the steady state $\{U_{ss} = 0, V_{ss} = \pi/2\}$ ($\{U_{ss} = \pm 0.56\pi, V_{ss} \simeq 0.13\pi\}$).

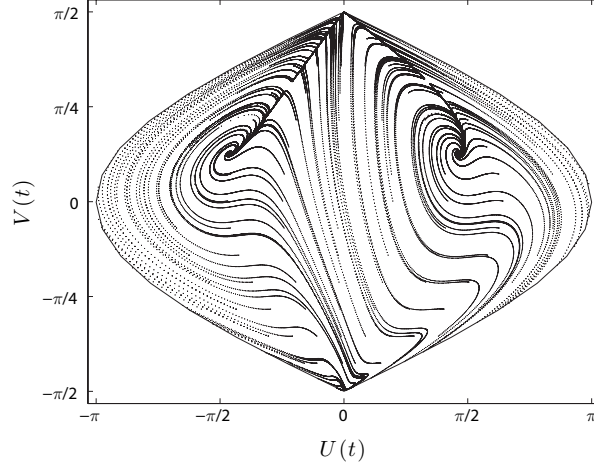


Figure 6.13. Trajectories on the Bloch sphere for different initial conditions, using the sinusoidal projection. Parameters are $h = 0.2$, $\lambda = 0.75$, and $\Gamma_b = 0.7$. For this choice of parameters the broken phase stable steady states are located at $U_{ss} \simeq \pm 0.56\pi$, $V_{ss} \simeq 0.13\pi$ (as calculated from Eqs. (6.4a)-(6.4a)), whilst the normal phase steady-state solution is located at $U_{ss} = 0$, $V_{ss} = \pi/2$. Note that the unstable solution described in the text is located at $U_{ss} \simeq \pm 0.21\pi$, $V_{ss} \simeq 0.31\pi$ for the parameters considered.

6.4.2 Entanglement

We now consider again the entanglement measures C_φ and C_R , both numerically for finite N and analytically for $N \gg 1$, corresponding to the linearized regime. Figure 6.14(a) shows a plot of C_φ as a function of Γ_b and φ for $N = 100$. We see that, well above the critical value $\Gamma_b = \lambda$, substantial entanglement is present over a broad range of angles φ . As Γ_b approaches λ from above, significant entanglement persists, but for a somewhat narrower range of angles φ . However, in the vicinity of $\Gamma_b = \lambda$ the entanglement diminishes rapidly for *all* values of φ as Γ_b decreases further.

To help understand these results we again utilize the atomic coherent state representation and study the spin Q -function. In Fig. 6.15 we plot $Q_s(\eta)$ on the Bloch sphere for a series of values of Γ_b in the vicinity of the first-order transition. Well above the critical point $Q_s(\eta)$ is a single-peaked function with little angular dependence. Correspondingly, C_φ is nonzero over a broad range of φ , with a maximum close to $\varphi = 3\pi/4$. Note that in contrast to the results found in [6], here there is a large shift of the optimum away from $\varphi = \pi/2$, since fluctuations in both the y and x directions are significant (see Fig. 6.11).

As Γ_b decreases towards the value λ , $Q_s(\eta)$ becomes increasingly stretched along a direction between the x - and y -axes. As the critical value $\Gamma_b = \lambda$ is traversed, $Q_s(\eta)$ changes from a single-peaked function to a triple-peaked function, corresponding to

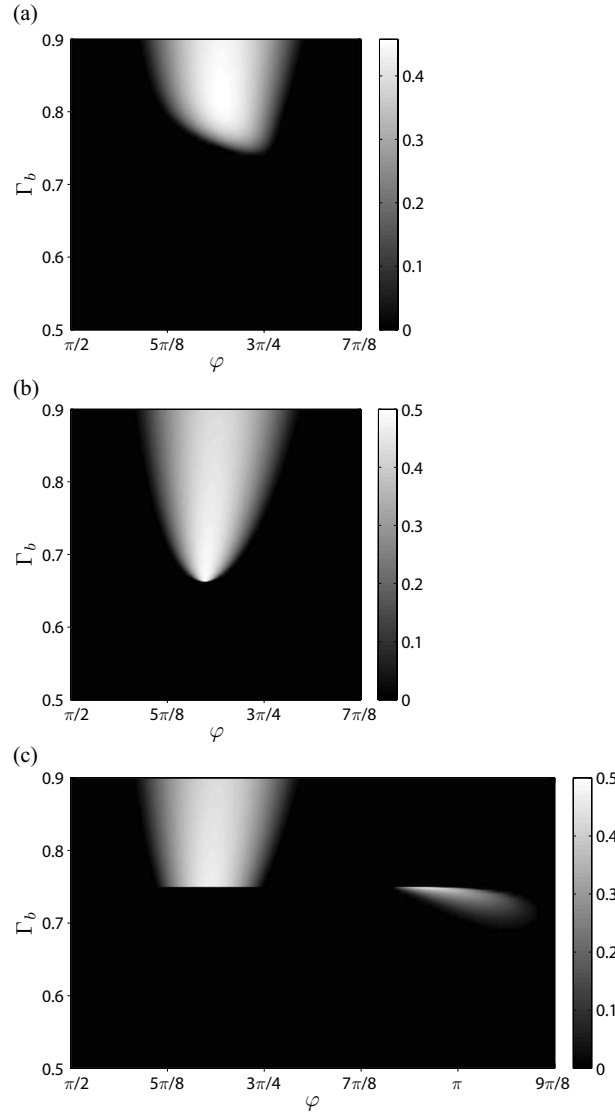


Figure 6.14. (a) Entanglement measure $\max\{0, C_\varphi\}$ for $N = 100$, $h = 0.2$, $\lambda = 0.75$, and $\Gamma_b^c = 0.66$. (b) Entanglement measure $\max\{0, C_\varphi\}$ in the thermodynamic limit, with the same parameters, for the steady state (6.15). (c) Entanglement measure $\max\{0, C_\varphi\}$ in the thermodynamic limit for the steady state (6.16a)-(6.16c).

the existence of three stable steady states in the region $\Gamma_b^c < \Gamma_b < \lambda$. As noted above, the range of φ over which C_φ remains finite narrows and then drops abruptly to zero as Γ_b approaches λ from above. This can be explained by noting that in the bistable region $\langle J_\varphi \rangle = 0$, and thus we again have $C_\varphi = 1 - (4/N) \langle [\sin(\varphi)J_x + \cos(\varphi)J_y]^2 \rangle$. Since both $\langle J_x^2 \rangle$ and $\langle J_y^2 \rangle$ are of order $j^2 = N^2/4$ in this region (see Fig. 6.11), this severely restricts the range of Γ_b and φ for which $C_\varphi > 0$.

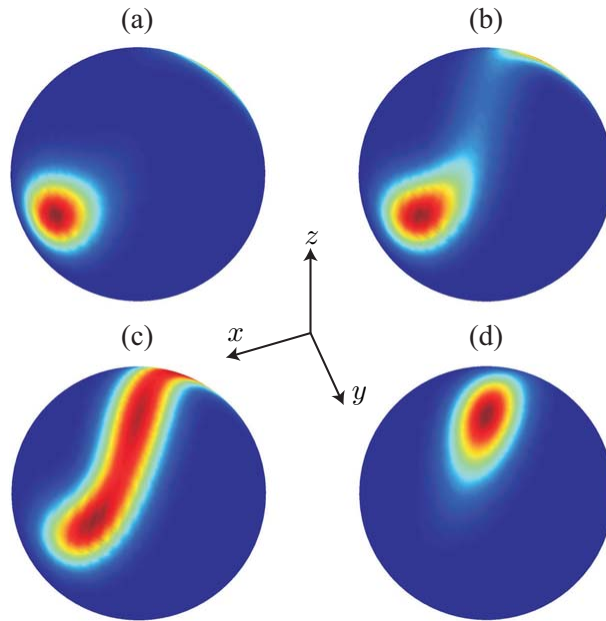


Figure 6.15. (Color online) Steady-state spin Q -function, $Q_s(\eta)$, on the Bloch sphere for (a) $\Gamma_b = 0.55$, (b) $\Gamma_b = 0.65$, (c) $\Gamma_b = 0.705$, and (d) $\Gamma_b = 0.85$, with $N = 50$, $h = 0.2$, $\lambda = 0.75$ and $\Gamma_b^c = 0.66$. Note that dark blue corresponds to the minimum value of zero of $Q_s(\eta)$ while dark red indicates the maximum value of $Q_s(\eta)$.

As the dissipation strength is decreased further, eventually the critical point Γ_b^c is crossed and the central peak of $Q_s(\eta)$ at the top of the Bloch sphere vanishes; we then recover the familiar two-lobed structure associated with the two semiclassical steady-state amplitudes. The moments $\langle J_x^2 \rangle$ and $\langle J_y^2 \rangle$ are still of order $j^2 = N^2/4$ in this region (and $\langle J_\varphi \rangle = 0$), and consequently $C_\varphi = 0$ for all φ .

Now we briefly turn to the thermodynamic limit again where we can obtain analytic results for $N \gg 1$ from the linearized HP model [6]. Outside the bistable region we can compute the entanglement by linearizing the fluctuations about the unique stable steady state. However, in the bistable region we can only compute the entanglement by linearizing about one or the other of the stable steady states.

In Fig. 6.14(b) we display C_φ as a function of the dissipation strength Γ_b and the phase angle φ for the choice of stable steady state given by Eq. (6.15). We observe that, for $\Gamma_b > \Gamma_b^c$, C_φ is nonzero over a broad range of φ centered around $\varphi = 3\pi/4$, whilst near the critical point Γ_b^c the corresponding range of φ narrows. Outside the bistable region C_φ is in reasonable agreement with the corresponding finite- N results, however, as might be expected inside the bistable region, the results differ considerably, since linearization around simply one of the stable steady states is inadequate.

In Fig. 6.14(c) we display C_φ for the choice of stable steady state given by Eqs. (6.16a)-(6.16c). For $\Gamma_b > \lambda$, C_φ is nonzero for a broad range of φ centered around $\varphi = 3\pi/4$,

which is also in reasonable agreement with the finite- N results. However, in addition, in the bistable region $\Gamma_b^c < \Gamma_b < \lambda$, we find that C_φ is nonzero for a small range of φ . Specifically, we see that with decreasing Γ_b , away from the critical point, C_φ becomes broader and its center moves toward $\varphi = \pi$. The existence of this second lobe and its behavior can be described by considering the fluctuations in the linearized regime. In contrast to the finite- N results one finds (not actually shown) that the fluctuations below the transition are less significant, thus giving $C_\varphi \neq 0$. The fact that the centre of C_φ moves toward π can be attributed to the dominating fluctuations in the x direction for $\Gamma_b \ll \Gamma_b^c$, as opposed to approximately equal fluctuations in the x and y direction for $\Gamma_b \simeq \Gamma_b^c$.

Finally, in Fig. 6.16 we plot the rescaled concurrence C_R as a function of the dissipation strength Γ_b , for $N = 100$ and in the thermodynamic limit (for each choice of stable steady state in the bistable region). For finite N the entanglement attains a peak value close to $\Gamma_b = \lambda$, while for $N \rightarrow \infty$ the entanglement peaks at either $\Gamma_b = \Gamma_b^c$ or $\Gamma_b = \lambda$ for the different steady states, respectively. It is worth noting that the entanglement for the case corresponding to the more stable steady state, i.e., Eqs.(6.16a)-(6.16c), agrees more closely with the finite- N result.

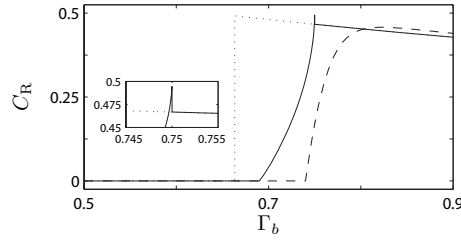


Figure 6.16. Rescaled concurrence C_R for $N = 100$ (dashed line), and in the thermodynamic limit [solid line for Eqs. (6.16a)-(6.16c), and dotted line for Eq. (6.15)], with $h = 0.2$, $\lambda = 0.75$ and $\Gamma_b^c = 0.66$.

6.4.3 Homodyne spectra

We have seen how entanglement in our system can be quantified in terms of moments of the collective spin operators. Spectra of fluctuations of the spin quadratures $J_\varphi = \sin(\varphi)J_x + \cos(\varphi)J_y$, i.e., homodyne spectra [27], also offer a useful probe of the system properties and are given by

$$\chi_\varphi(\nu) = \int_{-\infty}^{\infty} \langle J_\varphi(\tau) J_\varphi \rangle_{ss} e^{-i\tau\nu} d\tau, \quad (6.24)$$

i.e., by the Fourier transform of the two-time spin correlation function, with ν the Fourier space frequency. As we will see, such spectra can provide a very clear signature of bistability in the region $\Gamma_b^c < \Gamma_b < \lambda$. Note also that for the cavity-QED-based

realization of our interacting spin system, as described in [6], the cavity modes adiabatically follow the spin dynamics, and so $\chi_\varphi(\nu)$ can in fact be directly related to homodyne spectra of the cavity output field.

To compute Eq. (6.24) we calculate both the two-time correlation function $\langle J_\varphi(\tau)J_\varphi \rangle_{\text{ss}}$ (using the quantum regression formula) and its Fourier transform numerically for finite values of N [20]. In Fig. 6.17 we plot $\chi_\varphi(\nu)$ for a value of Γ_b in the bistable region (solid line) with the specific choice $\varphi = 0.52$ (discussed below); we see that three distinct peaks appear. The locations and widths of the peaks can be associated with the imaginary and real parts of eigenvalues of the system master equation (6.11), and for sufficiently large values of N these correspond simply to the eigenvalues μ_\pm obtained in the linearized analysis of Sec. 6.4.1. In the bistable region the eigenvalues corresponding to the trivial solution, i.e., μ_\pm as given by Eq. (6.18), have zero imaginary part, which corresponds to the central peak of $\chi_\varphi(\nu)$ in Fig. 6.17 located at $\nu = 0$. Similarly, for the eigenvalues corresponding to the nontrivial semiclassical solutions (6.16a)-(6.16c), i.e., μ_\pm as given by Eq. (6.19), we find $\text{Im}(\mu_\pm) \simeq \pm 2$ for the choice of parameters used in Fig. 6.17 (solid line), which coincide closely with the locations of the outer two peaks of $\chi_\varphi(\nu)$. The simultaneous presence in the finite- N spectrum of peaks corresponding to distinct semiclassical steady-state solutions signifies the bistability, i.e., the spectrum reflects contributions from both underlying stable semiclassical steady states. Note that within a linearized treatment, with linearization about only a single stable semiclassical steady state, no such superposition of spectral features can occur.

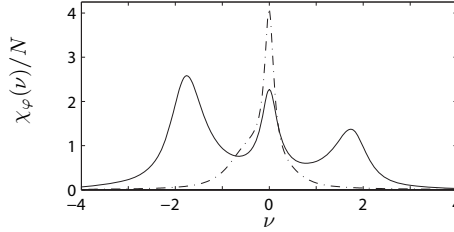


Figure 6.17. *Normalized homodyne spectrum, $\chi_\varphi(\nu)/N$, for $N = 100$, $h = 0.2$, and $\Gamma_a = 0.01$. The solid line is for parameters $\lambda = 1.5$ and $\Gamma_b = 1.185$, with $\Gamma_b^c = 1.02$, and $\varphi = 0.52$. The dash-dotted line is for parameters $\lambda = 0.75$ and $\Gamma_b = 0.71$, with $\Gamma_b^c = 0.66$, and $\varphi = 0.71$.*

For smaller values of λ , as considered in the linearized analysis of earlier sections, one is unable to resolve the three peaks of $\chi_\varphi(\nu)$ corresponding to the bistability (dash-dotted line in Fig. 6.17). In this regime of smaller λ , the bistable region is less pronounced and $\text{Im}(\mu_\pm)$ are smaller in magnitude, so the three peaks lie more closely together. In order to numerically resolve all peaks would require considerably larger values of N .

Outside the bistable region, the spectra for finite values of N consist simply of peaks associated with the unique stable semiclassical steady state. Specifically, for the trivial solution the spectra consist of a single peak centred at $\nu = 0$, whilst for the

nontrivial solution the spectra consist of two peaks located at $\nu = \text{Im}(\mu_{\pm})$ with μ_{\pm} given by Eq. (6.19). Note that within a linearized treatment we obtain similar results to the finite- N spectra outside the bistable region, since the stable semiclassical steady state is unique [6, 19].

Finally, we note that if we consider $\chi_{\varphi}(\nu)$ for the same parameters as in Fig. 6.17, but with different values of φ , then an additional very narrow peak (spike), superimposed on the central peak, occurs at $\nu = 0$. Mathematically, this feature occurs due to the presence of an eigenvalue of the Liouvillian, \mathcal{L} , with zero imaginary part and very small real part. Physically, it is associated with tunneling/switching between the pair of nontrivial semiclassical steady-states (6.16a)-(6.16c) [28]. This feature is absent in the usual linearized analysis, and so for the clearest possible comparison of the locations of the peaks of $\chi_{\varphi}(\nu)$ to the linearized eigenvalues we have focussed on a choice of φ where this spike is not present (as in Fig. 6.17). It is interesting to note that in fact the choice of φ that eliminates the “spike” corresponds to the axis joining the two semiclassical solutions which previously also played a crucial role in determining the optimized C_{φ} .

6.5 Conclusion

We have shown the presence of quantum phase transitions occurring due to the variation of the strength of dissipation in two different collective spin systems. For the cooperative resonance fluorescence model we computed the steady-state entanglement and showed how the results could be interpreted in terms of an atomic phase space distribution. In the dissipative LMG model we found that either a continuous or discontinuous phase transition occurs depending only on the ratio of the effective field and interaction strengths. The steady-state entanglement was analyzed in detail and the modifications due to strong dissipation were interpreted with the help of the atomic phase space distribution. In the regime of the first-order phase transition we showed that bistable behavior can occur as evidenced by the semiclassical analysis and, for finite N , homodyne spectra; specifically we showed that whilst a linearized analysis is generally inadequate in this regime, one of the two different stable solutions tends to dominate and this is also reflected by finite- N calculations. Finally, we have also briefly explained how both of these models might be implemented using an ensemble of atoms that interacts with optical cavity and laser fields, and thus how the entanglement properties might be measured via the cavity output field.

In the future, it would be interesting to compare the phase-dependent entanglement measure considered here with the context-based entanglement measure studied in [29], where entanglement is quantified by considering a continuous observation of the environment of a dissipative system. Specifically, the angle appearing in our phase-dependent measure can be associated with the phase of a local oscillator in the homodyne measurement considered in [29]. It would also be interesting to study entan-

lement criticality in dissipation-driven quantum phase transitions of other systems, such as generalized collective spin models [30] subjected to strong dissipation, or in collective models with additional short-range interactions [31] and dissipation.

Acknowledgements

The authors thank H. Carmichael for discussions and acknowledge support from the Austrian Science Foundation and from the Marsden Fund of the Royal Society of New Zealand.

Bibliography

- [1] For recent reviews, see D. Jaksch and P. Zoller, *Ann. Phys. (N.Y.)* **315**, 52 (2005), and I. Bloch, *Nature Phys.* **1**, 23 (2005).
- [2] M. Greiner, O. Mandel, T. Esslinger, T. Hänsch, and I. Bloch, *Nature* **415**, 39 (2002).
- [3] T. J. Osborne and M. A. Nielsen, *Phys. Rev. A* **66**, 032110 (2002).
- [4] D. Jaksch, C. Bruder, J. I. Cirac, C. W. Gardiner, and P. Zoller, *Phys. Rev. Lett.* **81**, 3108 (1998).
- [5] A. J. Leggett, S. Chakravarty, A. T. Dorsey, M. P. A. Fisher, A. Garg, and W. Zwerger, *Rev. Mod. Phys.* **59**, 1 (1987).
- [6] S. Morrison and A. S. Parkins, *Phys. Rev. A* **77**, 043810 (2008).
- [7] A. Kapitulnik, N. Mason, S. A. Kivelson, and S. Chakravarty, *Phys. Rev. B* **63**, 125322 (2001).
- [8] P. Werner, K. Völker, M. Troyer, and S. Chakravarty, *Phys. Rev. Lett.* **94**, 047201 (2005).
- [9] L. Capriotti, A. Cuccoli, A. Fubini, V. Tognetti, and R. Vaia, *Phys. Rev. Lett.* **94**, 157001 (2005).
- [10] M. A. Cazalilla, F. Sols, and F. Guinea, *Phys. Rev. Lett.* **97**, 076401 (2006).
- [11] P. D. Drummond and H. J. Carmichael, *Opt. Commun.* **27**, 160 (1978).
- [12] H. J. Carmichael, *J. Phys. B* **13**, 3551 (1980).
- [13] S. Schneider and G. J. Milburn, *Phys. Rev. A* **65**, 042107 (2002).

- [14] R. Bonifacio and L. A. Lugiato, Opt. Commun. **19**, 172 (1976); Phys. Rev. Lett. **40**, 1023 (1978); Phys. Rev. A **18**, 1129 (1978).
- [15] D. F. Walls, P. D. Drummond, S. S. Hassan, and H. J. Carmichael, Prog. Theor. Phys. Suppl. **64**, 307 (1978).
- [16] Note that we write the prefactor as γ/N in anticipation of taking the thermodynamic limit, $N \rightarrow \infty$ at constant density.
- [17] R. R. Puri and S. V. Lawande, Phys. Lett. **72A**, 200 (1979).
- [18] P. D. Drummond, Phys. Rev. A **22**, 1179 (1980).
- [19] F. Dimer, B. Estienne, A. S. Parkins, and H. J. Carmichael, Phys. Rev. A **75**, 013804 (2007).
- [20] For numerical solutions of the atomic collective-spin master equation we make use of: S. M. Tan, *Quantum Optics and Computation Toolbox for Matlab*, available at <http://www.qo.phy.auckland.ac.nz/qotoolbox.html>.
- [21] W. K. Wothers, Quant. Inf. Comp. **1**, 27 (2001).
- [22] J. K. Korbicz, J. I. Cirac, and M. Lewenstein, Phys. Rev. Lett. **95**, 120502 (2005); *ibid.* **95**, 259901 (2005).
- [23] T. Holstein and H. Primakoff, Phys. Rev. **58**, 1098 (1940).
- [24] J. P. Snyder, USGS Professional Paper **1395**, 243 (1987).
- [25] Note that although for $\Gamma_b < \Gamma_b^c$ there are already two stable steady states as given by Eqs. (6.16a)-(6.16c) this situation does not correspond to a bistability since the subsequent linearisation around each solution gives identical results.
- [26] Outside the bistable region we find results very similar to those already obtained in Sec. 6.3 for the second-order phase transition.
- [27] M. J. Collett and C. W. Gardiner, Phys. Rev. A **30**, 1386 (1984); C. W. Gardiner and M. J. Collett, *ibid.* **31**, 3761 (1985).
- [28] F. Dimer, PhD Thesis, University of Auckland (2007), unpublished.
- [29] H. Nha and H. J. Carmichael, Phys. Rev. Lett. **93**, 120408 (2004)
- [30] J. Vidal, Phys. Rev. A **73**, 062318 (2006).
- [31] C. F. Lee and N. F. Johnson, Phys. Rev. Lett. **93**, 083001 (2004).

Part II

Physical Replicas in Cold Atoms with Disorder

CHAPTER 7

PUBLICATION

Physical replicas and the Bose-glass in cold atomic gases[†]

arXiv:0805.0488 (2008)

S. Morrison¹, A. Kantian¹, A. J. Daley¹, H. G. Katzgraber², M. Lewenstein³, H. P. Büchler⁴, and P. Zoller¹

1) Institute for Theoretical Physics, University of Innsbruck, A-6020 Innsbruck, Austria

and Institute for Quantum Optics and Quantum Information of the Austrian Academy of Sciences, A-6020 Innsbruck, Austria

2) Theoretische Physik, ETH-Hönggerberg, CH-8092 Zürich, Switzerland

3) ICFO-Institut de Ciències Fotòniques, Parc Mediterrani de la Tecnologia, E-08860 Castelldefels (Barcelona), Spain, and

ICREA - Institució Catalana de Recerca i Estudis Avançats, 08010 Barcelona, Spain

4) Institute for Theoretical Physics III, University of Stuttgart, Pfaffenwaldring 57, 70550 Stuttgart, Germany

We study cold atomic gases in a disorder potential and analyze the correlations between different systems subjected to the same disorder landscape. Such independent copies with the same disorder landscape are known as replicas. While in general these are not accessible experimentally in condensed matter systems, they can be realized using standard tools for controlling cold atomic gases in an optical lattice. Of special interest is the overlap function which represents a natural order parameter for disordered systems and is a correlation

[†]The author of this thesis contributed to the present publication by analyzing the measurement scheme and performing all the analytical calculations of the overlap function. She also acted as a discussion partner in all other aspects of the work.

function between the atoms of two independent replicas with the same disorder. We demonstrate an efficient measurement scheme for the determination of this disorder-induced correlation function. As an application, we focus on the disordered Bose-Hubbard model and determine the overlap function within perturbation theory and a numerical analysis. We find that the measurement of the overlap function allows for the identification of the Bose-glass phase in certain parameter regimes.

7.1 Introduction

The interplay between disorder and interaction gives rise to a plethora of fundamental phenomena in condensed matter systems. The most predominant examples include spin glasses [1–3], the superconducting-to-insulator transition in thin superconducting films [4, 5], and localization phenomena in fermionic systems such as weak localization and the metal-insulator transition [6]. While the nature of order in spin glasses and its theoretical description is still highly debated [1, 7–14], a substantial contribution to the understanding of bosons in a disordered medium has been provided by work on the disordered Bose-Hubbard model introduced by Fisher *et al.* [15]. The disordered Bose-Hubbard model has recently attracted considerable attention due to its potential realization with cold atomic gases in an optical lattice [16–22].

A general challenge in the description of glass phases in disordered media is the absence of a simple order parameter distinguishing the different ground states. This problem becomes evident in the disordered Bose-Hubbard model where the phase diagram is determined by the competition between a superfluid phase, the Mott-insulator, and a Bose-glass phase. While the superfluid phase exhibits a finite condensate fraction and is characterized by off-diagonal long-range order, the Bose glass is only distinguished from the incompressible Mott-insulator by a vanishing excitation gap and a finite compressibility. However, in experiments on cold atomic gases the excitation gap and the compressibility are difficult to determine accurately and are also obscured by the finite harmonic trapping potential. The challenge is therefore to develop measurement schemes allowing for the experimental determination of these observables or to develop new observables to characterize the glass phase. While inaccessible in “real materials,” the Edwards-Anderson order parameter [1, 23] is commonly studied analytically and measured numerically to quantify the “order” in a disordered system. It can be expressed as the correlation between independently evolving systems with the same disorder landscape (so-called replicas), or as a correlation of the same system at different temporal measurements. Because the latter depends on an extra variable (temporal measurement window) it is advantageous to study two replicas of the system with the same disorder. Thus, the measurement of this order parameter requires the preparation of several samples with exactly the same disorder landscape, and the subsequent measurement of correlations between these.

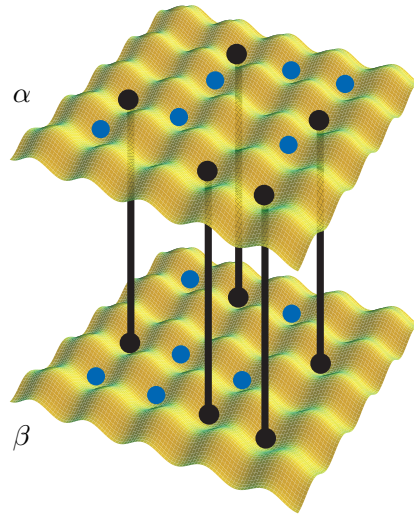


Figure 7.1. (Color online) Schematic representation of the implementation of disorder replicas with the cold atomic gases toolbox: Two planes α and β with equal disorder realizations, illustrated here for the case of a disorder landscape introduced using a second particle species (black dots), in which additional probe atoms (blue/lighter dots) evolve. The planes can be combined to measure correlation functions, such as the Edwards-Anderson overlap function.

We demonstrate that such a procedure is feasible in cold atomic gases allowing one to gain access to characteristic properties of disordered systems naturally hidden in condensed matter systems. The basic idea is to focus on cold atomic gases in an optical lattice: along one direction, the optical lattice is very strong and divides the system into independent two-dimensional (2D) planes [24–27]. In addition, the system is subjected to a disorder potential and we are interested in the situation where in each plane the same disorder landscape is realized (see Fig. 7.1). Although the atoms in different planes are decoupled, the presence of the same disorder landscape within each plane induces a correlation between the different realizations: this correlation is of special interest in the replica theory of spin glasses and allows one to measure the overlap function, a characteristic property of spin glasses. Furthermore, we show that this correlation function is accessible in experiments on cold gases: The main idea is to quench the motion of the atoms by a strong optical lattice, and combine the different planes into a single one. Subsequently, the particle number occupation within each well carries the information about the correlation function. The possibility for the accurate determination of the particle number within each well of an optical lattice has recently been demonstrated experimentally for the superfluid-Mott-insulator quantum phase transition [28].

Note that this measurement scheme for the overlap between system with the same disorder can be applied to any disordered one- or two-dimensional system realized with

cold atomic gases in an optical lattice. Of special interest is the realization of spin glasses and their study in the quantum regime. As an application, we focus here on the disordered Bose-Hubbard model and calculate the overlap function analytically in different regimes and compare it with one-dimensional numerical simulations. We find that the overlap function q exhibits a sharp crossover from the Mott-insulating phase with $q \approx 0$ [29] to the Bose-glass phase with $q \approx p(1 - p)$, with $p \in (0, 1)$, and thus makes it possible to distinguish the two phases. Because the superfluid phase can be detected via the interference peaks in a time-of-flight measurement, we propose that this novel measurement scheme for the overlap function can be used for a qualitative experimental verification of the phase diagram for the disordered Bose-Hubbard model.

Different implementations of disorder or quasi-disorder in cold atomic gases have been discussed and experimentally realized. Several groups attempted to search for traces of Anderson localization and the interplay of disorder-nonlinear interactions in Bose-Einstein condensates (BECs). The first experiments [30–34] were performed with laser speckles that had a disorder correlation length larger than the condensate healing length. Localization effects were thus washed out by interactions. As an alternative, superlattice techniques—which are combinations of several optical potentials with incommensurable spatial periods—were used to produce quasi-disordered potentials with short correlations. This approach allowed the observation of some signatures of the Bose glass by the Florence group [35]. Only very recently the Palaiseau group has managed to create speckle potentials on the sub-micron scale and directly observe Anderson localization effects in a BEC released in a one-dimensional waveguide [36]. The Florence group reported observations of localization phenomena in quasi-disordered potentials in BEC of K^{39} , which allows for complete control of the strength atomic interactions using Feshbach resonances [37]. It is worth noting that experimental attempts for local addressability in an optical lattice also offer the possibility to create disorder with correlation lengths comparable to the lattice spacing [38, 39]. Mixtures of cold gases, on the other hand, provide an alternative approach for the realization of disorder by quenching the motion of one species by a strong optical lattice, which then provides local impurities for the second species [40, 41]. While production of 2D planes with equal disorder realizations follows naturally if the disorder is implemented with laser speckles, we also show how such a system can be realized in the case of disorder induced by a mixture of atomic gases.

In Sec. 7.2, we start with a detailed description of the disordered Bose-Hubbard model and the different disorder realizations. After a short review of the phase diagram of the disordered Bose-Hubbard model, we provide the definition of the overlap function q characterizing the disorder-induced correlations between independent realizations of the system. In Sec. 7.3, we describe in detail the preparation of the system and the subsequent measurement scheme for the overlap function. In Sec. 7.4, we determine the overlap for the disordered Bose-Hubbard model via perturbation theory for physically-relevant limits and compare the result with numerical simulations of the one-dimensional system. Details of the calculations are presented in the appendices.

7.2 Bose-Hubbard model with Disorder

Cold atomic gases subjected to an optical lattice are well described by the Bose-Hubbard model [34, 42]

$$H = -J \sum_{\langle ij \rangle} b_i^\dagger b_j + \frac{U}{2} \sum_i n_i(n_i - 1) - \sum_i (\mu - \Delta_i) n_i, \quad (7.1)$$

with b_i^\dagger (b_i) the bosonic creation (annihilation) operator and $n_i = b_i^\dagger b_i$ the particle number operator at the lattice site i . The first term describes the kinetic energy of the atoms with hopping energy J between nearest-neighbor sites, the second term accounts for the onsite interaction between the atoms, and the third term describes the disorder potential with random-site off-sets Δ_i of the chemical potential μ .

The disorder potential $\{\Delta_i\}$ can be generated via different methods [30–32, 35, 40, 41] and is determined by a probability distribution $P(\delta)$ describing the probability of having an onsite shift with strength δ . The mean square of the disorder distribution

$$\Delta^2 = \int d\delta \delta^2 P(\delta) \quad (7.2)$$

gives rise to a characteristic energy scale Δ of the disorder potential (note that the mean energy shift of the disorder potential is absorbed in the definition of the chemical potential). In addition, the disorder potential is characterized by a correlation length. Here, we are interested in short-range disorder with the disorder in different wells independent of each other. The probability distribution $P(\delta)$ and its correlation length depend on the microscopic realization in cold atomic gases, thus the most promising possibilities are laser speckle patterns and mixtures of different cold atomic gases. While first experiments with laser speckles had a disorder correlation length larger than the lattice spacing [30, 31], experimental efforts towards local addressability in an optical lattice also offer the possibility for the creation of disorder with a correlation length comparable to the lattice spacing, as well as Gaussian probability distributions [38, 39]. Alternatively, a disorder potential can also be created in mixtures of cold atomic gases in optical lattices [43, 44] by quenching the motion of one species. Then, the disorder correlation length is naturally of the order of the lattice spacing, while the probability distribution becomes bimodal with $\Delta_i = \pm\Delta$; here we are primarily interested in such short range disorder with Δ_i being independent in different wells. Note that both Gaussian disorder, as well as bimodal disorder generally give rise to different physical phenomena in glass physics and thus both are interesting in their own right.

The zero-temperature phase diagram of the Hamiltonian (7.1) was first studied by Fisher *et al.* [15] where three different phases were discussed: the superfluid, the Mott-insulator, and the Bose-glass phases. In the two-dimensional regime of interest here, the superfluid phase appears for large hopping energies $J \gtrsim U, \Delta$ and is characterized by off-diagonal (quasi) long-range order (finite superfluid condensate) and a

linear excitation spectrum giving rise to a finite compressibility. On the other hand, for dominating interaction energies $U \gg \Delta, J$ the ground state corresponds to an incompressible Mott-insulator phase with an excitation gap and a commensurate filling factor, i.e., the averaged particle number in a single well $\langle n_i \rangle \in \mathbb{N}$ is an integer. While the quantum phase transition from the superfluid to the Mott-insulator has been experimentally identified [45], the disorder potential gives rise to an additional Bose-glass phase characterized by a vanishing excitation gap and finite compressibility; see Fig. 7.2 for a sketch of the phase diagram. The details of the phase diagram have been studied via analytical methods in the regime of Anderson localization [41, 46, 47] and in other regimes via numerical methods such as quantum Monte Carlo [48], density matrix renormalization group (DMRG) [49], dynamical mean-field theory [50], and analytical methods [51, 52]. Furthermore, recent interests focused also on the appearance of alternative phases for different disorder types in the Bose-Hubbard model, e.g., off-diagonal disorder giving rise to a Mott-glass phase [53].

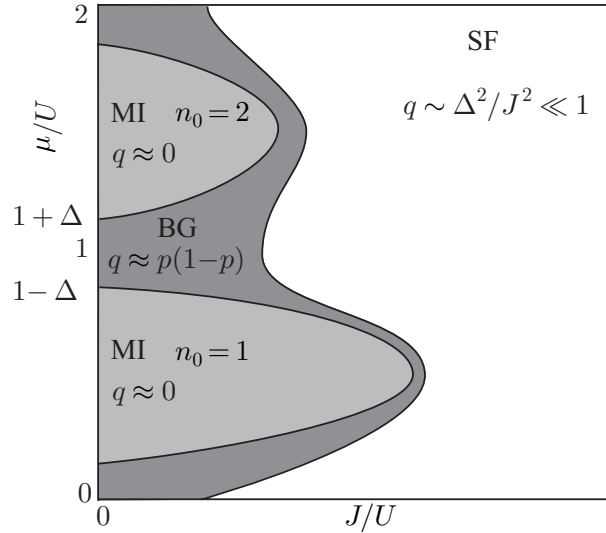


Figure 7.2. *Sketch of the phase diagram for the disordered Bose-Hubbard model: the Mott-insulator (MI) appears for integer filling and the overlap function q vanishes for small hopping $J/U \ll 1$, while in the Bose-glass phase (BG) the overlap function approaches a finite value $q = p(1-p)$ with $p \in (0, 1)$ characterizing the bimodal disorder distribution (see Sec. 7.4). Consequently a measurement of the overlap allows for a clear distinction between the Bose-glass and the Mott-insulator phase in this regime. In turn, the superfluid phase (SF) is characterized by off-diagonal long-range order resulting in coherence peaks in a time of flight experiment.*

The superfluid phase in the absence of disorder is experimentally identified via a measurement of the coherence peaks characterizing the condensate fraction, while the transition to a Mott-insulating phase is characterized by the disappearance of these interference patterns and as well as a change in the behavior of excitations [24, 45].

However, the identification of the Bose-glass phase in the presence of disorder requires an additional observable allowing for the distinction between the Mott-insulator and the Bose-glass, where the condensate fraction vanishes. Such an additional property is known from spin-glass theory as the Edwards-Anderson order parameter [1, 23] which appears as an order parameter in the mean-field theory on spin glasses [54]. In the present situation with a disordered Bose-Hubbard model, its generalization leads to

$$q_{EA} = [(\langle n_i \rangle - n)^2]_{av} = [\langle n_i^2 \rangle]_{av} - ([\langle n_i \rangle]_{av})^2, \quad (7.3)$$

where $n = [\langle n_i \rangle]_{av}$ denotes the mean particle density in the sample. It is important to note the different averages involved in the definition of the order parameter q_{EA} : for a fixed disorder realization, the average $\langle \dots \rangle$ denotes the thermodynamic average over the ground state of the system, while $[\dots]_{av}$ describes the disorder average over different disorder realizations. While the experimental determination of this quantity in the Bose-Hubbard model requires an exact state tomography of the system for each lattice site, a simpler and alternative route is obtained by preparing two systems with the same disorder landscape and measuring the correlations between these two decoupled systems: the remaining correlation is disorder induced and disappears for weak disorder. This so-called overlap function q between the two systems realized with the same disorder landscape takes the form

$$q = [\langle n_i^\alpha \rangle \langle n_i^\beta \rangle]_{av} - [\langle n_i^\alpha \rangle]_{av} [\langle n_i^\beta \rangle]_{av} \quad (7.4)$$

and where α and β describe the two different systems with the same disorder. This definition follows in close analogy of the mean-field order parameter in the replica theory of spin glasses [54].

7.3 Measurement of the Overlap Function

In this section we outline the key process of this work, i.e., the basic experimental procedure by which physical replicas can be prepared and used to measure the overlap function q defined in Eq. (7.4). This consists of three essential steps: (1) initial preparation of disorder replicas, (2) introduction of probe atoms and (3) the measurement process, involving recombination of the replicas and spectroscopy to measure the overlap itself. At no stage do we assume individual addressability of lattice sites, but rather consider global operations and the measurement of global quantities.

7.3.1 Initial preparation of disorder replicas

We consider a situation in which atoms are confined to a three-dimensional optical lattice, which is particularly deep along the z -direction, so that an array of planes with 2D lattice potentials are formed in the x - y plane, with no tunneling between the

planes. Each of these 2D planes of the potential can be divided into two subplanes, again along the z -direction, by adding a superlattice of half the original period which can be controllably switched on and off [25, 26]. The resulting two subplanes then constitute our replicas, and our goal is that these pieces should have the same disorder realization.

In the case of disorder generated optically (using, e.g., speckle patterns) the different layers exhibit the same disorder landscape for a suitable orientation of the lasers. However, for a disorder induced by a second species, the replicas must be produced in several steps. We start with a two-species mixture in the undivided plane. A fast ramping up of the optical lattice depth within the plane for the disorder species results in a Poissonian distribution of particles in the lattice. The next step is then a filtering procedure removing singly-occupied sites and keeping only doubly-occupied and unoccupied sites (which are distributed randomly). Such a filtering procedure has been achieved in recent experiments where atoms are combined to Feshbach molecules, and atoms remaining unpaired are removed from the system using a combination of microwave and optical fields that is energy-selective based on the molecular binding energy [55]. Finally, the superlattice is applied adiabatically providing a double-layer structure, where exactly one atom of the disorder species is transferred to each of the two subplanes. The result is two planes with a random distribution of atoms of the “disorder species,” with an exact copy in each subplane, i.e., a replica of the random disorder pattern. This is illustrated in Fig. 7.1.

Interactions between atoms of a probe species and the disorder species can now be adiabatically increased, or the probe species otherwise adiabatically introduced to the system (e.g., using spin-dependent lattices or superlattices). This results in two replicas of the same system, which we label α and β , with atoms in each replica evolving independently according to their system Hamiltonian in the same disorder potential. We again reiterate that the superlattice separating the replicas should be deep, so that there is no tunnelling between the replicas. The only correlations between the two should thus be determined by the identical disorder realizations.

7.3.2 Measurement process

To measure the overlap q as given in Eq. (7.4) we need to compute correlation functions that compare the state of probe atoms in the two replicas α and β . In each case, the correlation functions can be computed if we measure the joint probability distribution for occupation numbers in the two replicas (this is discussed in detail below). In particular, we need to determine the proportion of lattice sites in layer α having n particles given that there are m particles in the corresponding lattice site in layer β , which we denote p_{nm} , and the fraction of lattice sites in layer α, β with n particles denoted by $p_n^{\alpha, \beta}$ (both depicted in Fig. 7.3). We thus first freeze the state in each replica by ramping the lattice suddenly to deeper values in all three directions, so that

tunnelling no longer occurs. We can then measure the different possible configurations of particles occupying individual lattice sites in the layers α and β (see Figs. 7.3–7.5).

This is done in two steps: First, the layers are combined so that at each site each initial eigenstate involving different occupation numbers in the two replicas becomes a superposition of degenerate states involving the total number of atoms spread over motional states in a single well (see Fig. 7.4, Sec. 7.3.2 below). The final state is, of course, strongly dependent on the combination process, as well as the initial state before the combination of the layers. However, we need only determine the fraction of lattice sites with a total of n particles, denoted p_n , which is unchanged provided that the lattice is deep within each plane, to prevent tunnelling of atoms. The relative frequency with which each final configuration p_n occurs can then be measured based on the different spectroscopic energy shifts arising from different numbers of atoms in the final well, and different distributions of atoms over the motional states (see Fig. 7.5, Sec. 7.3.2 below). This involves weak coupling of atoms to an auxiliary internal state, similar to that performed in Ref. [28]. We show that the set of possible final states given an initial configuration can be distinguished spectroscopically from the set of states corresponding to initial configurations giving different contributions to p_n , and thus we can reconstruct the original joint probability distribution p_{nm} prior to combining the layers. The reduced probabilities $p_n^{\alpha,\beta}$ can be determined from similar spectroscopy without first combining the layers, allowing the full overlap function q to be constructed. Below we give further details of each step in this procedure.

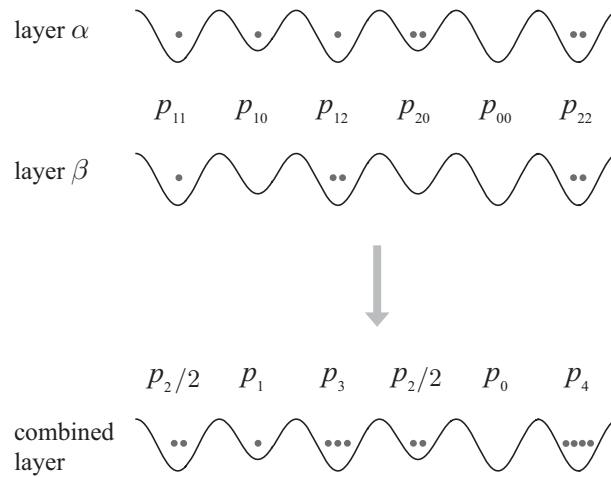


Figure 7.3. A sample system illustrating the required joint and combined system probabilities involved in the measurement scheme before and after combining the two layers respectively. Top: The individual layers α and β and the corresponding joint probability p_{nm} at each site. Bottom: Combined layer and the corresponding combined system probability p_n at each site. Note that this is only a guide, because after combining the layers the particles are spread across multiple motional states (not depicted).

Quantities that need to be measured

We need to measure two quantities to determine the overlap q , namely $[\langle \hat{q}_1 \rangle]_{av}$, where

$$\hat{q}_1 = \frac{1}{L} \sum_i n_i^\alpha n_i^\beta, \quad (7.5)$$

with $\alpha \neq \beta$ and L is the total number of lattice sites, corresponding to the density-density correlations between the two layers, and $[\langle \hat{q}_2^\alpha \rangle]_{av}$, $[\langle \hat{q}_2^\beta \rangle]_{av}$, where

$$\hat{q}_2^{\alpha,\beta} = \frac{1}{L} \sum_i n_i^{\alpha,\beta}, \quad (7.6)$$

corresponding to the average density of each layer. Then we can express

$$q = [\langle \hat{q}_1 \rangle]_{av} - [\langle \hat{q}_2^\alpha \rangle]_{av} [\langle \hat{q}_2^\beta \rangle]_{av}. \quad (7.7)$$

The disorder average should be performed by repeated measurements of the quantum average for different realizations of the disorder [56]. In general, one can expect that a measurement on n_i and n_j for large separation between sites i and j is independent of each other, and consequently the summation over lattice sites automatically performs a statistical quantum average [57]. In the following, we are interested in small filling factors such that lattice sites with three or more particles are rare and can be neglected in all three phases of the system.

First we focus on measurement of $[\langle \hat{q}_2^\alpha \rangle]_{av} [\langle \hat{q}_2^\beta \rangle]_{av}$, i.e., the second term of the overlap in Eq. (7.4). If the layers are prepared as discussed above, the symmetry $(1/L) \sum_i \langle n_i^\alpha \rangle = (1/L) \sum_i \langle n_i^\beta \rangle$ is preserved and thus we can measure the average over two replicas, $[\langle \hat{q}_2 \rangle]^2$ where [58]

$$\hat{q}_2 = \frac{1}{2}(\hat{q}_2^\alpha + \hat{q}_2^\beta) = \frac{1}{2L} \sum_i (n_i^\alpha + n_i^\beta). \quad (7.8)$$

For the average density we obtain:

$$\langle \hat{q}_2 \rangle = \frac{1}{2L} \sum_i \langle n_i^\alpha \rangle + \langle n_i^\beta \rangle = \frac{1}{2} \sum_n n(p_n^\alpha + p_n^\beta), \quad (7.9)$$

where $p_n^{\alpha,\beta} = N_n^{\alpha,\beta}/L$ with $N_n^{\alpha,\beta}$ the number of sites with n particles in layers α, β , and thus

$$\langle \hat{q}_2 \rangle = \frac{1}{2}(p_1^\alpha + p_1^\beta + 2p_2^\alpha + 2p_2^\beta). \quad (7.10)$$

Next we consider the measurement of $[\langle \hat{q}_1 \rangle]$ i.e., the first part of the overlap in Eq. (7.4). In this case the density-density correlations can be expressed as

$$\frac{1}{L} \sum_i \langle n_i^\alpha n_i^\beta \rangle = \sum_n n m p_{nm}, \quad (7.11)$$

where $p_{nm} = N_{nm}/L$ with N_{nm} the total number of sites with n particles in layer α and m particles in layer β , and thus, keeping terms up to two particles in total over the replicas at a given site

$$\langle \hat{q}_1 \rangle = \frac{1}{L} \sum_i \langle n_i^\alpha n_i^\beta \rangle = p_{11} + 2(p_{12} + p_{21}) + 4p_{22}. \quad (7.12)$$

Now consider $p_n = N_n/L$, with N_n the total number of particles from both layers, which can be measured by combining both layers (described in detail in Sec. 7.3.2) and subsequently applying a similar scheme to the one presented in Ref. [28] (described in detail in Sec. 7.3.2). Using the following equations that relate both p_n and $p_n^{\alpha,\beta}$ to p_{nm}

$$\begin{aligned} p_1 &= p_{01} + p_{10} & p_1^\alpha &= p_{10} + p_{12} + p_{11}, \\ p_2 &= p_{20} + p_{02} + p_{11} & p_1^\beta &= p_{01} + p_{21} + p_{11}, \\ p_3 &= p_{12} + p_{21} & p_2^\alpha &= p_{20} + p_{21} + p_{22}, \\ p_4 &= p_{22} & p_2^\beta &= p_{02} + p_{12} + p_{22}, \end{aligned}$$

we can show that $p_{11} = \frac{1}{2}(p_1^\alpha + p_1^\beta - p_1 - p_3)$ which in conjunction with $p_3 = p_{12} + p_{21}$ and $p_4 = p_{22}$ gives all necessary terms. Then, Eq. (7.12) simplifies to

$$\langle \hat{q}_1 \rangle = \frac{1}{2}(p_1^\alpha + p_1^\beta - p_1) + \frac{3}{2}p_3 + 4p_4. \quad (7.13)$$

Finally, note that \hat{q}_2 as given in Eq. (7.10), can also be expressed as $\langle \hat{q}_2 \rangle = \frac{1}{2} \sum_n n p_n$.

In the following two sections we show how to measure these conditional probabilities by combining the two replicas together, and performing spectroscopy where a single atom is coupled to a different internal state. In Sec. 7.3.2 we describe the process of combining the two layers into a single one whilst in Sec. 7.3.2 we describe a similar scheme to the one presented in Ref. [28] that can be used to distinguish different occupation numbers.

Combining layers

We now describe in more detail the process of combining the two layers into a single one and determine the resulting joint state for the different possible initial configurations. The combination of the layers is achieved by lowering the potential barrier that separates both layers (switching off the superlattice). Specifically, we now determine the final (after completely lowering the barrier) state for each of the different initial configurations of particles (prior to lowering the barrier).

After the superlattice is removed and layers are combined, the system is described by the Hamiltonian

$$H_{\text{comb}} = \sum_{k \in \{0,1\}} \left[\epsilon_k n_k + \frac{U_{kk}}{2} n_k (n_k - 1) \right] + 2U_{01} n_0 n_1, \quad (7.14)$$

where $U_{kl} = 2\omega_{\perp}a \int dz |w_k(z)|^2 |w_l(z)|^2$, with a the scattering length, ω_{\perp} the transverse trapping frequency, $w_k(z)$ the Wannier functions for band k , and ϵ_k the band energy ($k, l \in \{0, 1\}$).

States which are initially nondegenerate will evolve adiabatically to the corresponding eigenstate of the Hamiltonian (7.14), provided the barrier is lowered slowly with respect to the energy separation between the (nondegenerate) eigenstates. However, we note that some of the initial states are doubly degenerate due to the equal single particle energies in the two layers. Thus when the barrier is lowered these degenerate states become coupled to each other (because the single particle states change time dependently) and the final state will evolve into a process-dependent superposition of the different corresponding eigenstates of the Hamiltonian (7.14). However, this poses no problem for our measurement scheme since the states that are initially degenerate contribute equally to the probabilities we are trying to measure. Moreover, for a given initial configuration it is not necessary to know the full final state, in fact it is sufficient to know only the possible corresponding final eigenstates of the Hamiltonian (7.14) (with the same number of particles as the initial configuration) that contribute to the final state. Figure 7.4 depicts all the different possible states before and after combining the layers for up to a maximum of four particles in total.

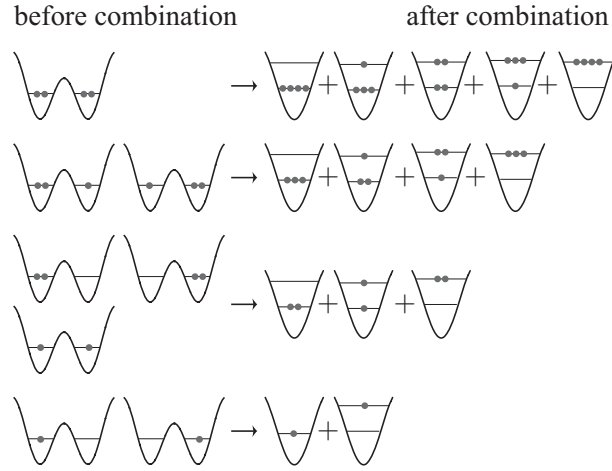


Figure 7.4. *Analysis of the process of combining the two initial replicas, showing possible states with at most double occupation (dots) in a given well before combination of the layers (left hand side), and the resulting possible states after combination of the layers (right hand side). Note that here ‘+’ indicates a general superposition with unspecified coefficients, as these are dependent on the precise time dependence of system dynamics during combination. Knowledge of these coefficients is not necessary in the measurement scheme presented here.*

In the next section we show how the different configurations for a given particle number can be measured and thus the total occupation numbers determined.

Number distribution characterization

We now investigate a scheme similar to the one presented in Ref. [28] that uses density-dependent energy shifts to spectroscopically distinguish different particle numbers at each site of the combined layer (see Sec. 7.3.2 above). We begin with all atoms in an internal state a , and investigate the weak coupling of particles to a second internal state b (with at most one particle transferred). Due to the difference in interaction energy between particles of species a and b , and particles solely of species a there is an energy shift between the “initial” state (all particles of species a) and “final” state (one particle of species b and all others particles of species a). Thus different initial particle numbers can be distinguished by the energy shift (corresponding to the Raman detuning at which the transfer is resonant), provided the shift is different for the different particle numbers. Since particles in the combined layer can be spread across multiple motional states (see Sec. 7.3.2 above), different energy shifts occur for different configurations of the same number of particles. Whilst we find that the energy shifts of some of the configurations (of the same number of particles) are identical or very similar, there are other configurations having substantially different energy shifts. Thus we have to check that the energy shifts for all configurations of a given number of particles can be distinguished from energy shifts of configurations corresponding to a different total number of particles. To this end we now present a detailed calculation of the energy shifts arising from all the different initial configurations of particles and show in which cases the total number of particles can be distinguished.

Let a_k^\dagger and b_k^\dagger denote the creation operators for particles of species a and b , respectively, in band k where $k \in \{0, 1\}$. Then the Raman coupling between the two internal states a and b is described by an effective Hamiltonian (within a rotating-wave approximation)

$$H_{\text{RC}} = \frac{\Omega(t)}{2}(a_0^\dagger b_0 + a_1^\dagger b_1 + \text{H.c.}) - \Delta(t)(b_0^\dagger b_0 + b_1^\dagger b_1), \quad (7.15)$$

where $\Delta(t)$ is the Raman detuning, $\Omega(t)$ the effective two-photon Rabi frequency, and we have assumed that $\Omega(t) \ll \Delta'$ where Δ' are the detunings of the lasers from the atomic excited state. In what follows we assume that $\int \Omega(t)dt \ll \pi$, i.e., weak coupling to internal state b and that the two lasers creating the Raman transition are running waves with equal wave vectors. Note that processes in which the internal state and the band would change do not occur provided the Raman detuning and effective two-photon Rabi frequency are smaller than the band separation.

The onsite interaction energy for atoms of species a and b in the lowest two bands is described by the following Hamiltonian

$$\begin{aligned} H_{\text{int}} = & \sum_{i \in \{a, b\}} \left[\frac{U_{00}^{ii}}{2} n_0^i (n_0^i - 1) + \frac{U_{11}^{ii}}{2} n_1^i (n_1^i - 1) + 2U_{01}^{ii} n_0^i n_1^i \right] + U_{00}^{ab} n_0^a n_0^b + U_{11}^{ab} n_1^a n_1^b \\ & + U_{01}^{ab} \left[n_0^a n_1^b + n_1^a n_0^b + (a_0^\dagger a_1 b_1^\dagger b_0 + a_1^\dagger a_0 b_0^\dagger b_1 + \text{H.c.}) \right], \end{aligned} \quad (7.16)$$

where

$$U_{kl}^{ij} = 2\omega_{\perp} a_{ij} \int dz |w_k(z)|^2 |w_l(z)|^2, \quad (7.17)$$

with a_{ij} the scattering length between two particles in internal states i and j ($i, j \in \{a, b\}$), ω_{\perp} the transverse trapping frequency, and $w_k(z)$ the Wannier functions corresponding to band k ($k, l \in \{0, 1\}$). Note we have also introduced the particle number operators $n_k^a = a_k^{\dagger} a_k$ and $n_k^b = b_k^{\dagger} b_k$. We further make the assumption that the lattice is very deep so that we can approximate all the Wannier functions by simple harmonic oscillator eigenfunctions. This assumption of a deep lattice gives the following simplified expressions $2U_{01}^{ij} = U_{00}^{ij}$ and $U_{11}^{ij} = (3/4)U_{00}^{ij}$.

Using Eq. (7.16) we now explicitly compute the energy shift $\Delta E = E_f - E_i$ associated with the processes $|i\rangle \rightarrow |f\rangle$, where $|i\rangle$ is the initial state corresponding to all particles of species a and having energy E_i , and $|f\rangle$ is the final state corresponding to one particle transferred to internal state b and having energy E_f . Clearly, ΔE depends on how the particles are initially distributed in the lower and higher bands after combining the two layers (see the right hand side of Fig. 7.4). There are two different cases to be considered; either all particles are initially in the same band (this is the situation in Ref. [28]) or particles are initially in both bands. In the latter case it is then possible that particles in either band are transferred to internal state b and since these different possible resulting states are coupled by the interaction Hamiltonian (7.16) the final resulting state is a superposition of these, corresponding to an eigenstate of the Hamiltonian (7.16).

For example, let us consider a total initial number of two particles as depicted in Fig. 7.5. The different initial and final states are most conveniently expressed in the occupation number basis $|N_0^a, N_1^a; N_0^b, N_1^b\rangle$ with $N_0^{a,b}$ ($N_1^{a,b}$) the number of particles of species a, b in the lower (higher) band at a given lattice site. First consider the case where both particles are initially in the lower or higher bands corresponding to the initial states $|2, 0; 0, 0\rangle$ or $|0, 2; 0, 0\rangle$ (see top and bottom of Fig. 7.5). The corresponding final states are given by $|1, 0; 1, 0\rangle$ and $|0, 1; 0, 1\rangle$, and the corresponding energy shifts are $\Delta E/U_{00}^{aa} = \epsilon - 1$ and $\Delta E/U_{00}^{aa} = \frac{3}{4}(\epsilon - 1)$, where we have defined $\epsilon \equiv U_{00}^{ab}/U_{00}^{aa}$. Next we consider the case where there is a particle in each band initially corresponding to the initial state $|1, 1; 0, 0\rangle$ (see middle of Fig. 7.5). Then the corresponding final states are the eigenstates of the Hamiltonian (7.16) in the subspace corresponding to one particle of species a and one particle of species b given by $|1, 1\rangle_{\pm} \equiv (1/\sqrt{2}) (|0, 1; 1, 0\rangle \pm |1, 0; 0, 1\rangle)$, with eigenenergies $E_{+}/U_{00}^{aa} = \epsilon$ and $E_{-}/U_{00}^{aa} = 0$. The associated energy shifts for these two possible final states are $\Delta E/U_{00}^{aa} = \epsilon - 1$ and $\Delta E/U_{00}^{aa} = -1$ respectively. Note that the Raman transition only couples the state $|1, 1\rangle_{+}$ to the initial state $|1, 1; 0, 0\rangle$ with a matrix coupling element $\Omega_{fi} = \sqrt{2}$, where $\Omega_{fi} \equiv \langle f | H_{\text{RC}} | i \rangle$, while for the state $|1, 1\rangle_{-}$ we find $\Omega_{fi} = 0$. Figure 7.5 summarizes the different possible configurations for a total of two particles together with the corresponding energy shift ΔE and matrix coupling element Ω_{fi} . We note that the energy shifts, ΔE , for the different final states to which the initial states couple (i.e., $\Omega_{fi} \neq 0$) are very similar, this is of advantage since our

scheme needs only to distinguish energy shifts for different *total* particle numbers.


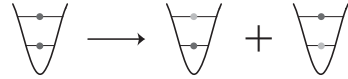
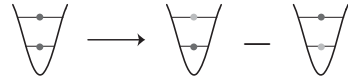

$ i\rangle \longrightarrow f\rangle$	Ω_{fi}	$\Delta E/U_{00}^{aa}$
	$\sqrt{2}$	$(\epsilon-1)$
	$\sqrt{2}$	$(\epsilon-1)$
	0	-1
	$\sqrt{2}$	$\frac{3}{4}(\epsilon-1)$

Figure 7.5. *Illustration of the number distribution characterization within the two layers for states with two particles in the combined layer. On the left are all possible initial configurations of two particles of species a in the combined lattice (dark-colored circles) and the corresponding final states with one particle each of species a and b (light-colored circles). On the right we list the respective coupling matrix elements, Ω_{fi} , and energy shifts, $\Delta E/U_{00}^{aa}$, for each of the configurations on the left.*

Similarly, we can determine the energy shifts and coupling matrix elements for other numbers of particles. If all particles are initially in the lower or higher state corresponding to the initial states $|N_0^a, 0; 0, 0\rangle$ or $|0, N_1^a; 0, 0\rangle$, the corresponding final states are given by $|N_0^a - 1, 0; 1, 0\rangle$ and $|0, N_1^a - 1; 0, 1\rangle$. The corresponding energy shifts are then given by $\Delta E/U_{00}^{aa} = (N_0^a - 1)(\epsilon - 1)$ and $\Delta E/U_{00}^{aa} = \frac{3}{4}(N_1^a - 1)(\epsilon - 1)$, and the matrix coupling element in each case is $\Omega_{fi} = \sqrt{N_0^a}$ and $\Omega_{fi} = \sqrt{N_1^a}$ respectively. For other initial configurations with m particles in the lower band and n particles in the higher band the corresponding final states are found by diagonalizing the Hamiltonian (7.16) in the appropriate particle subspace. This always results in a pair of eigenstates denoted $|m, n\rangle_{\pm}$ with eigenenergy $E_{\pm}^{(m,n)}$ and using these expressions the energy shift ΔE and coupling matrix elements Ω_{fi} can be directly determined. For a total initial number of three and four particles the expressions for $|m, n\rangle_{\pm}$, $E_{\pm}^{(m,n)}$, ΔE and Ω_{fi} are given in appendix 7.A.1 and 7.A.2, respectively, for all the different initial configurations. In Tab. 7.1 we list the results for up to a maximum number of four particles; the first column lists the different initial configurations and corresponding final states, the second column lists the corresponding matrix coupling elements Ω_{fi} and the third column lists the associated energy shifts ΔE .

$ i\rangle \rightarrow f\rangle$	Ω_{fi}	$\Delta E/U_{00}^{aa}$	Ω_{fi}	$\Delta E/U_{00}^{aa}$
$ 1, 0; 0, 0\rangle \rightarrow 0, 0; 1, 0\rangle$	1	0	1	0
$ 0, 1; 0, 0\rangle \rightarrow 0, 0; 0, 1\rangle$	1	0	1	0
$ 2, 0; 0, 0\rangle \rightarrow 1, 0; 1, 0\rangle$	$\sqrt{2}$	$\frac{3}{4}(\epsilon - 1)$	1.4	-0.018
$ 2, 0; 0, 0\rangle \rightarrow 1, 0; 1, 0\rangle$	$\sqrt{2}$	$(\epsilon - 1)$	1.4	-0.024
$ 1, 1; 0, 0\rangle \rightarrow 1, 1\rangle_+$	$\sqrt{2}$	$(\epsilon - 1)$	1.4	-0.024
$ 1, 1; 0, 0\rangle \rightarrow 1, 1\rangle_-$	0	-1	0	-1
$ 3, 0; 0, 0\rangle \rightarrow 2, 0; 1, 0\rangle$	$\sqrt{3}$	$2(\epsilon - 1)$	1.7	-0.049
$ 2, 1; 0, 0\rangle \rightarrow 2, 1\rangle_+$	$\sqrt{3}$	$2(\epsilon - 1)$	1.7	-0.049
$ 2, 1; 0, 0\rangle \rightarrow 2, 1\rangle_-$	0	$\frac{\epsilon}{2} - 2$	0	-1.5
$ 1, 2; 0, 0\rangle \rightarrow 1, 2\rangle_+$	$\eta_+^{(1,2)}$	$E_+^{(1,2)} - 3$	1.7	-0.29
$ 1, 2; 0, 0\rangle \rightarrow 1, 2\rangle_-$	$\eta_-^{(1,2)}$	$E_-^{(1,2)} - 3$	-0.0034	-1.8
$ 0, 3; 0, 0\rangle \rightarrow 0, 2; 0, 1\rangle$	$\sqrt{3}$	$\frac{3}{2}(\epsilon - 1)$	1.7	-0.037
$ 4, 0; 0, 0\rangle \rightarrow 3, 0; 1, 0\rangle$	$\sqrt{4}$	$3(\epsilon - 1)$	2	-0.073
$ 3, 1; 0, 0\rangle \rightarrow 3, 1\rangle_+$	$\sqrt{4}$	$3(\epsilon - 1)$	2	-0.073
$ 3, 1; 0, 0\rangle \rightarrow 3, 1\rangle_-$	0	$\epsilon - 3$	0	-2.0
$ 2, 2; 0, 0\rangle \rightarrow 2, 2\rangle_+$	$\eta_+^{(2,2)}$	$E_+^{(2,2)} - \frac{23}{4}$	2.0	-0.070
$ 2, 2; 0, 0\rangle \rightarrow 2, 2\rangle_-$	$\eta_-^{(2,2)}$	$E_-^{(2,2)} - \frac{23}{4}$	-0.0031	-2.0
$ 1, 3; 0, 0\rangle \rightarrow 1, 3\rangle_+$	$\eta_+^{(1,3)}$	$E_+^{(1,3)} - \frac{15}{4}$	2.0	1.4
$ 1, 3; 0, 0\rangle \rightarrow 1, 3\rangle_-$	$\eta_-^{(1,3)}$	$E_-^{(1,3)} - \frac{15}{4}$	-0.0054	-0.52
$ 0, 4; 0, 0\rangle \rightarrow 0, 3; 0, 1\rangle$	$\sqrt{4}$	$\frac{9}{4}(\epsilon - 1)$	2	-0.055

Table 7.1. *Resonant energies and coupling strengths for the transfer of single atoms in the combined layer to a different internal state. Column one lists the different initial configurations and the corresponding final states up to a maximum number of four particles. In the second and third column we list the matrix coupling elements Ω_{fi} and energy shifts ΔE , respectively, corresponding to the different initial configurations in the first column. The states $|m, n\rangle_{\pm}$ are listed in the text and appendices together with the corresponding eigenenergies $E_{\pm}^{(m,n)}$ and coupling matrix elements $\eta_{\pm}^{(m,n)}$. The last two columns give numerical values of Ω_{fi} and ΔE for the specific value $\epsilon = 0.98$.*

It is possible to distinguish different occupation numbers for specific ranges of ϵ if the energy shifts for different total numbers of particles are distinct. The desired range of ϵ is then between points where any energy shifts for different total number of particles would coincide (e.g., $\epsilon = 1$) [59]. For a specific example we consider the value $\epsilon = 0.98$ (corresponding to scattering length values in Ref. [28]) and give numerical values for the matrix coupling elements Ω_{fi} and the energy shifts ΔE in columns four and five, respectively, in Tab. 7.1. Then, to a high accuracy, the determination of p_n

is obtained by applying the coupling between the different internal states a and b for a short time $t_n = \Delta t / \sqrt{n}$ at all resonant frequencies in Tab. 7.1 with total number of particles n (ignoring the resonances with small and vanishing couplings Ω_{fi}). The total number of transferred particles is then proportional to p_n and efficiently avoids problems arising from non-adiabatic combination of the layers.

7.4 Overlap Function in the Disordered Bose-Hubbard model

In this section we determine the overlap function q [see Eq. (7.4)] in the disorder Bose-Hubbard model, both analytically and numerically. We focus on a bimodal disorder potential $\Delta_i = \pm\Delta$ with the probability distribution $P(\Delta) = 1 - P(-\Delta) = p$, which is the appropriate description for the chosen disorder implementation (see discussion in earlier sections). In the following, we present the modifications due to the presence of a weak ($\Delta < U/2$) bimodal disorder potential, and the prediction for the overlap function within the different phases (see Fig. 7.2). It follows from this constraint that we do not enter the compressible disordered phase, and hence the system will always have a unique ground state. Thus, the ground states in two exact copies α, β of the system (i.e. same disorder distribution) are the same, and consequently $\langle n_i^\alpha \rangle = \langle n_i^\beta \rangle$. We therefore expect a Sherrington-Kirkpatrick-type behavior for the overlap [60], i.e. the overlap between any two copies will always be the same, and thus the overlap function q can in fact be calculated using Eq. (7.3).

While the above is a self-evident statement for a replica-symmetric system such as the one we examine here, it may no longer be true for systems thought to exhibit replica-symmetry breaking (e.g. a classical spin glass type model [54], or quantum systems with extended interactions [61]). For the latter type of system, measurement of the overlap function using physical replicas (see Sec. 7.3) is thought to yield different values for the overlap depending on α and β , the defining signature of replica symmetry-breaking.

In Sec. 7.4.1 we analytically calculate the overlap function, for the various phases of the disorder Bose-Hubbard model (7.1), whilst in Sec. 7.4.2 we present results for the overlap function from numerical simulation of the one-dimensional system.

7.4.1 Analytical determination of the overlap function

Starting with the limit of vanishing hopping $J = 0$, Eq. (7.1) reduces to an onsite Hamiltonian and the ground state is given by $|\Omega\rangle = \prod_i |\Omega\rangle_i$ with $|\Omega\rangle_i$ the lowest energy state within each site i . This lowest energy states takes the form $|\Omega\rangle_i = |n_i\rangle$ with $|n_i\rangle$ being a state with fixed particle number n_i at site i , with n_i subject to the constraint

$$U(n_i - 1) < \mu - \Delta_i < Un_i. \quad (7.18)$$

For a weak bimodal disorder potential ($\Delta < U/2$), we have to distinguish two different cases.

First, for a chemical potential within the range $U(n_0 - 1) + \Delta < \mu < Un_0 - \Delta$ the above constraint in Eq. (7.18) is fulfilled independently of the site parameter i for the integer value n_0 , i.e., at each site the ground state is characterized by the integer particle density $[\langle n_i \rangle]_{av} = n_0$ and we obtain a Mott-insulator (MI) phase (see Fig. 7.2). Furthermore, the overlap parameter vanishes identically in this limit, i.e., $q = 0$ for a Mott-insulator at $J = 0$.

Second, for chemical potentials in the range $Un_0 - \Delta < \mu < Un_0 + \Delta$, the particle number at sites with different disorder potential Δ_i differs by a single particle, i.e., at each site with disorder potential $\Delta_i = \Delta$ the particle number is determined by n_0 , while at sites with disorder potential $\Delta_i = -\Delta$ the lowest energy state is characterized by $n_0 + 1$ particles. Therefore, the averaged particle density and the overlap parameter take the form

$$[\langle n_i \rangle]_{av} = n_0 + (1 - p) \quad q = p(1 - p). \quad (7.19)$$

This situation corresponds to the disorder-induced Bose-glass (BG) phase (see Fig. 7.2) and the ground state is characterized by nonhomogeneous filling. Similarly to the case of the MI phase, the particle number is fixed over a finite range of the chemical potential and thus the BG is incompressible. In contrast to the MI phase, the BG phase is characterized by a non-vanishing overlap parameter dependent on p .

Next, we focus on small hopping, $J \ll U, \Delta, \mu$, and determine the overlap function using perturbation theory. We seek a unitary transformation of the form $U = e^{-iS}$ which transforms the total Hamiltonian (7.1) to an effective Hamiltonian having the same eigenspectrum but acting only in the space of the unperturbed eigenstates. Using this unitary transformation we can directly determine the corrections due to hopping in perturbation theory by computing $\langle \Omega | \tilde{n}_i | \Omega \rangle$ where $\tilde{n}_i \equiv U^\dagger n_i U$. Details are given in appendix 7.B.

We start with the Mott-insulator and consider the leading order (non-vanishing) correction to the overlap function which occurs at fourth order due to a site (disorder) independent density, $\langle \Omega | n_i | \Omega \rangle = n_0$ (using $|\Omega\rangle_i = |n_0\rangle$ in the MI). To lowest order in perturbation theory the overlap is then given by

$$q = J^4 \left([\langle \tilde{A}_2 \rangle^2]_{av} - [\langle \tilde{A}_2 \rangle]_{av}^2 \right), \quad (7.20)$$

where

$$\tilde{A}_2 = -\frac{1}{2}[S_1, [S_1, n_i]], \quad (7.21)$$

with

$$S_1 = -i \sum_{\langle jk \rangle} c_{jk} |\Omega\rangle \langle \phi_{jk}| + \text{H.c.}, \quad (7.22)$$

and $|\phi_{jk}\rangle = |n_0 + 1\rangle_j |n_0 - 1\rangle_k \Pi_{l \neq ij} |n_0\rangle_l$. Using these expressions it is straightforward to compute the expectation value of the density correction

$$\langle \tilde{A}_2 \rangle = n_0(n_0 + 1) \sum_{\langle j(i) \rangle} \left(\frac{1}{(E_0 - E_{ij})^2} - \frac{1}{(E_0 - E_{ji})^2} \right), \quad (7.23)$$

where $E_0 - E_{ij} = -U + \Delta_j - \Delta_i$. It is now straightforward to calculate the disorder averages and the overlap is given by

$$q = 64(n_0(n_0 + 1))^2 p(1-p) z(z+1) \frac{J^4 U^2 \Delta^2}{(U^2 - 4\Delta^2)^2}, \quad (7.24)$$

where z is the number of nearest neighbors.

Next we turn to the Bose-glass phase and consider the leading order (non-vanishing) correction to the overlap function which occurs here at second order. The expression for the overlap in lowest-order perturbation theory is then given by

$$q = q_0 + J^2 \left([\langle n_i \rangle \langle \tilde{A}_2 \rangle]_{av} - [\langle n_i \rangle]_{av} [\langle \tilde{A}_2 \rangle]_{av} \right), \quad (7.25)$$

where $q_0 = p(1-p)$ (the overlap at zero hopping), \tilde{A}_2 and S_1 are as given above for the MI phase but with

$$|\Omega\rangle = \prod_l [d_l |n_0 + 1\rangle_l + (1 - d_l) |n_0\rangle_l], \quad (7.26)$$

and

$$\begin{aligned} |\phi_{jk}\rangle &= [d_j |n_0 + 2\rangle_j + (1 - d_j) |n_0 + 1\rangle_j] [d_k |n_0\rangle_k + (1 - d_k) |n_0 - 1\rangle_k] \\ &\quad \times \Pi_{l \neq jk} [d_l |n_0 + 1\rangle_l + (1 - d_l) |n_0\rangle_l], \end{aligned} \quad (7.27)$$

where $d_{j,k,l}$ ($1 - d_{j,k,l}$) is zero (one) for $\Delta_{j,k,l} = \Delta$ ($\Delta_{j,k,l} = -\Delta$). Again, using these expressions it is straightforward to compute the expectation value of the density correction and for $n_0 \geq 1$ we obtain

$$\langle \tilde{A}_2 \rangle = \sum_{\langle j(i) \rangle} \left(\frac{\gamma_{ij}^2}{(E_0 - E_{ij})^2} - \frac{\gamma_{ji}^2}{(E_0 - E_{ji})^2} \right), \quad (7.28)$$

where

$$E_0 - E_{ij} = -U(1 - d_i + d_j) + \Delta_j - \Delta_i, \quad (7.29)$$

and

$$\gamma_{ij} = (d_i \sqrt{n_0 + 2} + (1 - d_i) \sqrt{n_0 + 1})(d_j \sqrt{n_0 + 1} + (1 - d_j) \sqrt{n_0}). \quad (7.30)$$

Once again a straightforward calculation of the disorder averages gives the following expression ($n_0 \geq 1$) for the overlap:

$$q = p(1-p) \left(1 - J^2 \frac{(n_0 + 1)^2 U(U - 2\Delta) + \Delta^2}{2\Delta^2(U - \Delta)^2} \right). \quad (7.31)$$

An analogous calculation for $n_0 = 0$ gives

$$q = p(1 - p) \left(1 - \frac{J^2}{2\Delta^2} \right), \quad (7.32)$$

which corresponds to the $U \rightarrow 0$ limit of Eq. (7.31).

When the effects of hopping dominate, the bosonic atoms are in the superfluid phase (see Fig. 7.2). Then, the influence of weak disorder on the superfluid phase can be studied within a generalized mean-field approach. In analogy to the Gross-Pitaevskii formalism, we replace the bosonic operators b_i in the Hamiltonian (7.1) by a local complex field ψ_i , and minimize the corresponding free energy functional $H(\psi_i)$. The effect of disorder is to produce fluctuations in the local density. Hence we make the ansatz $\psi_i = e^{i\phi} \sqrt{n_0 + \delta n_i}$ where n_0 is the homogeneous density in the absence of disorder and $\delta n_i \propto \Delta_i$ is the disorder induced density fluctuation. Introducing the notation $\delta n = [\delta n_i]_{av}$ as the disorder-averaged density fluctuation, the particle density reduces to $[\langle n_i \rangle]_{av} = n_0 + \delta n$. We substitute this ansatz into $H(\psi_i)$, expand ψ_i for small fluctuations, $\delta n_i \ll n_0$ (see appendix 7.C) and minimize the resulting expression in Eq. (7.75) at fixed particle number, which is equivalent to requiring $[\delta n_i]_{av} = 0$. Note that for large dimension and thus a large number of nearest neighbors we may replace

$$\sum_{\langle j(i) \rangle} \delta n_j \approx z \delta n. \quad (7.33)$$

Using this relation and self-consistently solving for the density fluctuations δn_i (see appendix 7.C) gives the overlap function

$$q = \left(\frac{4n_0\Delta}{2Un_0 + zJ} \right)^2 p(1 - p), \quad (7.34)$$

where $n_0 = (\mu + Jz)/U + \frac{1}{2}$.

In summary, we find that in the limit of small hopping $J/U \ll 1$, the overlap signals a sharp crossover between the Mott-insulator with $q \approx 0$ and the Bose-glass with $q \approx p(1 - q)$, see Fig. 7.2. In turn, the superfluid phase is characterized by off-diagonal long range order giving rise to coherence peaks in a time of flight picture. Consequently, the overlap and the coherence peaks in time of flight allow for a clear identification of the phases in the disordered Bose-Hubbard model. However, we would like to point out that the overlap function behaves smoothly across the phase transition and consequently is not suitable for the precise determination of the exact location of the phase transition.

7.4.2 Numerical results

We have simulated the disordered Bose-Hubbard model (7.1) in 1D using a number-conserving algorithm based on time-dependent matrix product states [62, 63]. In the matrix product state representations, we reduce the Hilbert space by retaining only the χ most significant components in a Schmidt-decomposition of the state at each possible bipartite splitting of the system. States in 1D can be efficiently represented in this way, with relatively small χ giving essentially unity overlap between the represented state and the actual state. The simulations both serve as a check for the perturbation theory, and allow computation of the overlap function beyond the perturbation limit from the microscopic model.

Because we consider the regime $2\Delta < U$, the system remains incompressible and does not enter the disordered glass phase. Therefore we do not expect replica-symmetry breaking to occur. For our simulations, the presence of replica-symmetry is equivalent to convergence to a unique ground-state for any given disorder independent of initial conditions. The overlap function can then be computed as

$$q = \frac{1}{L} \sum_i \langle n_i \rangle^2 - \bar{n}^2, \quad (7.35)$$

where \bar{n} is the density of the system. Computation of the overlap function can be simplified in this way as $L^{-1} \sum_i \langle n_i \rangle$ self-averages to $[\langle n_i \rangle]_{av}$ for sufficiently large systems, which in turn self-averages to \bar{n} .

The ground states used in Eq. (7.35) are computed by imaginary-time evolution, c.f. Ref. [63], of the 1D Bose-Hubbard-model (7.1) with a randomly-chosen bimodal distribution, and different impurity strengths 2Δ . The lattice size is $L = 64$, representative of current experimental capabilities, and we compute the overlap as a function of Δ for several different values of U/J and the fraction of impurity-occupied sites, p . In Fig. 7.6 we display results for $U/J = 10$ and $p = 0.5$. We have performed convergence tests in the time step, the duration of imaginary-time evolution, the number of disorder realizations, and the number of retained states χ . We find that the overlap function converged even for surprisingly small values of $\chi \sim 20$ states in the large U/J limit (Mott-insulator or Bose-glass regime). Regarding the number of disorder realizations for each value of Δ , we find that whilst 10 random realizations of bimodal disorder are not sufficient to narrow the error down, 20 realizations suffice. Much of the observed fluctuations in the value of the overlap function for a given Δ stem from the fact that we allow the number of impurities in each realization to fluctuate around the mean Lp . Conversely, in our simulation data we observe different disorder realizations with the same number of impurities having overlaps closer to each other than the error bars in Fig. 7.6 would suggest.

As shown in Fig. 7.6, we generally found very good agreement between numerical simulations and perturbation theory in its region of validity. For the Mott-insulator regime (commensurate filling factor) this is the regime where $2\Delta \ll U$. We observe the

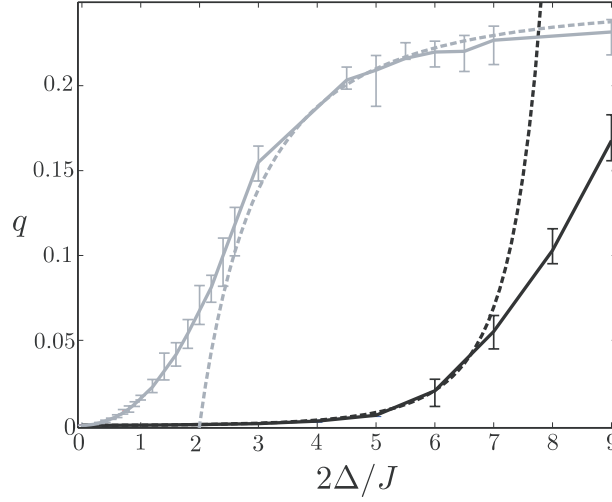


Figure 7.6. Overlap function q as a function of impurity strength Δ in the Mott-insulating phase at filling factor $n_0 = 1$ (black lines) and in the Bose-glass phase for $n_0 = 0$ (gray lines). In both cases, the impurity probability is $p = 0.5$ and $U/J = 10$, for $L = 64$. Simulation results (solid lines) are shown versus results from perturbation theory (dashed lines). Much of the variation in the simulated overlap function is due to the fact that we allow the number of impurities to fluctuate around the value given by Lp in each particular disorder realization. Note that the perturbation result in the Mott-insulator diverges as Δ approaches U due to energy degeneracy [c.f. Eq. (7.24)]. In the Bose-glass phase, second-order perturbation theory yields a divergence as Δ approaches 0, again due to energy degeneracy [c.f. Eq. (7.32)].

breakdown of our second-order perturbation theory as Δ approaches $U/2 = 5J$, which is caused by energy-degeneracy of adjacent impurity- and non-impurity occupied sites when $\Delta = U/2$. In the Bose-glass regime, breakdown of perturbation theory sets in for low Δ , as degeneracy occurs there for $\Delta = 0$.

7.5 Conclusion

We have shown how the Bose-glass phase can be identified by measuring the overlap function characterizing the correlations between disorder replicas, i.e., systems having identical disorder landscape. We have described a procedure to create disorder replicas using cold atomic gases in an optical lattice, focusing on the case of disorder induced by a second atomic species. A scheme to measure the overlap has been presented, which involves the characterization of the occupation numbers in both the individual replicas and the joint system, where both replicas have been combined. Specifically, we have shown that after combining the replicas together, particles can be distributed across

multiple motional states and we explained in detail how to determine the occupation number distribution in this situation. Using perturbation theory we have calculated the overlap for weak hopping and have shown the different behaviors exhibited in the Mott-insulator and Bose glass phases; these results are in good agreement with the results from a one-dimensional numerical simulation. In the opposite limit of very large hopping we also obtain analytical results for the overlap within a mean-field-theory treatment.

Applying our proposed measurement scheme for the overlap to other types of disordered models [54, 61] would provide interesting insights to characteristic properties of disorder-induced quantum phases. Of particular interest would be the quantum spin glass where the overlap corresponds to the Edwards-Anderson order parameter which has been conjectured to exhibit replica symmetry breaking [54], i.e., the results for the overlap depend on the particular replica. In addition to equilibrium properties considered here, the dynamics of the overlap might also possess an interesting behavior, and could be measured in a similar setup. In one-dimension the time evolution of the overlap could be determined numerically [63].

Acknowledgements

Work in Innsbruck was supported by the Austrian Science foundation through SFB F15, the EU network SCALA and project I118_N16 (EuroQUAM_DQS). S.M. thanks the Department of Physics of the University of Auckland for their hospitality. H.G.K. acknowledges support from the Swiss National Science Foundation under Grant No. PP002-114713. M.L. acknowledges support of ESF PESC Programme “QUDEDIS” and Spanish MEC grants (FIS 2005-04627, Consolider Ingenio 2010 “QOIT”).

7.A Energy Shifts and Couplings for Three and Four particles

In the following two sections we determine expressions for the eigenstates and eigenenergies of Eq. (7.16), i.e., $|m, n\rangle_{\pm}$ and $E_{\pm}^{(mn)}$ and associated energy shifts and couplings for all possible initial configurations of three and four particles. Note that the case where all particles are in the lowest or highest energy band has already been explained in Sec. 7.3.2 and will not be discussed here further.

7.A.1 Three particles

We consider the two different configurations described by the initial states i) $|2, 1; 0, 0\rangle$ and ii) $|1, 2; 0, 0\rangle$.

For case i) the two eigenstates are given by

$$|2, 1\rangle_+ = \frac{1}{\sqrt{3}}(|2, 0; 0, 1\rangle + \sqrt{2}|1, 1; 1, 0\rangle), \quad (7.36)$$

$$|2, 1\rangle_- = \frac{1}{\sqrt{3}}(-\sqrt{2}|2, 0; 0, 1\rangle + |1, 1; 1, 0\rangle), \quad (7.37)$$

with eigenenergies $E_+^{(2,1)} = 2\epsilon + 1$ and $E_-^{(2,1)} = \epsilon/2 + 1$ respectively. We see that only the state $|2, 1\rangle_+$ couples to the initial state $|2, 1; 0, 0\rangle$, with a matrix coupling element of $\Omega_{fi} = \sqrt{3}$, whilst for the state $|2, 1\rangle_-$ we find $\Omega_{fi} = 0$. The energy shifts for the two different possible processes are given by $\Delta E/U_{00}^{aa} = 2(\epsilon - 1)$ and $\Delta E/U_{00}^{aa} = \frac{\epsilon}{2} - 2$.

For case ii) the two eigenstates are given by

$$|1, 2\rangle_{\pm} = \frac{1}{\sqrt{1 + (\gamma_{\pm}^{(1,2)})^2}} \left(\gamma_{\pm}^{(1,2)} |0, 2; 1, 0\rangle + |1, 1; 0, 1\rangle \right), \quad (7.38)$$

where

$$\gamma_{\pm}^{(1,2)} = \frac{-1 - \epsilon \pm \sqrt{33\epsilon^2 + 2\epsilon + 1}}{4\sqrt{2}\epsilon}, \quad (7.39)$$

and with eigenenergies

$$E_{\pm}^{(1,2)} = \epsilon + 1 \pm \frac{1}{8}\sqrt{33\epsilon^2 + 2\epsilon + 1} + \frac{1}{8}(\epsilon - 1). \quad (7.40)$$

In this case both states $|1, 2\rangle_{\pm}$ have nonzero coupling to the state $|1, 2; 0, 0\rangle$ given by

$$\begin{aligned} \Omega_{fi} &= \eta_{\pm}^{(1,2)} \equiv \langle 1, 2 |_{\pm} H_{\text{RC}} | 1, 2; 0, 0 \rangle \\ &= \frac{1}{\sqrt{1 + (\gamma_{\pm}^{(1,2)})^2}} (\gamma_{\pm}^{(1,2)} + \sqrt{2}). \end{aligned} \quad (7.41)$$

The energy shifts for the two different possible processes are given by $\Delta E/U_{00}^{aa} = E_{\pm}^{(1,2)} - 3$.

7.A.2 Four particles

We consider the three different configurations described by the initial states i) $|3, 1; 0, 0\rangle$, ii) $|2, 2; 0, 0\rangle$ and iii) $|1, 3; 0, 0\rangle$.

For case i) the eigenstates are given by

$$|3, 1\rangle_+ = \frac{1}{\sqrt{4}}(|3, 0; 0, 1\rangle + \sqrt{3}|2, 1; 1, 0\rangle), \quad (7.42)$$

$$|3, 1\rangle_- = \frac{1}{\sqrt{4}}(-\sqrt{3}|3, 0; 0, 1\rangle + |2, 1; 1, 0\rangle), \quad (7.43)$$

with eigenenergies $E_+^{(3,1)} = 3(\epsilon + 1)$ and $E_-^{(3,1)} = \epsilon + 3$, respectively. We see that only the state $|3, 1\rangle_+$ couples to the initial state $|3, 1; 0, 0\rangle$, with a matrix coupling element of $\Omega_{fi} = \sqrt{4}$, whilst for the state $|3, 1\rangle_-$ we find $\Omega_{fi} = 0$. The energy shifts for the two different possible processes are given by $\Delta E/U_{00}^{aa} = 3(\epsilon - 1)$ and $\Delta E/U_{00}^{aa} = \epsilon - 3$.

For case ii) the eigenstates are given by

$$|2, 2\rangle_\pm = \frac{1}{\sqrt{1 + (\gamma_\pm^{(2,2)})^2}} (\gamma_\pm^{(2,2)} |1, 2; 1, 0\rangle + |2, 1; 0, 1\rangle), \quad (7.44)$$

where

$$\gamma_\pm^{(2,2)} = \frac{-1 + \epsilon \pm \sqrt{65\epsilon^2 - 2\epsilon + 1}}{8\epsilon}, \quad (7.45)$$

and with eigenenergies

$$E_\pm^{(2,2)} = 3 + 2\epsilon \pm \sqrt{65\epsilon^2 - 2\epsilon + 1} - \frac{1}{8}(1 + \epsilon). \quad (7.46)$$

In this case, generally both states $|2, 2\rangle_\pm$ have nonzero coupling to the state $|2, 2; 0, 0\rangle$ given by

$$\begin{aligned} \Omega_{fi} &= \eta_\pm^{(2,2)} \equiv \langle 2, 2 |_\pm H_{\text{RC}} | 2, 2; 0, 0 \rangle \\ &= \sqrt{\frac{2}{1 + (\gamma_\pm^{(2,2)})^2}} (\gamma_\pm^{(2,2)} + 1). \end{aligned} \quad (7.47)$$

The energy shifts for the two different possible processes are given by $\Delta E/U_{00}^{aa} = E_\pm^{(2,2)} - \frac{23}{4}$.

For case iii) the eigenstates are given by

$$|1, 3\rangle_\pm = \frac{1}{\sqrt{1 + (\gamma_\pm^{(1,3)})^2}} (\gamma_\pm^{(1,3)} |0, 3; 1, 0\rangle + |1, 2; 0, 1\rangle), \quad (7.48)$$

where

$$\gamma_{\pm}^{(1,3)} = \frac{-1 - \epsilon \pm \sqrt{13\epsilon^2 + 2\epsilon + 1}}{2\sqrt{3}\epsilon}, \quad (7.49)$$

and with eigenenergies

$$E_{\pm}^{(1,3)} = 3 + 2\epsilon \pm \sqrt{13\epsilon^2 + 2\epsilon + 1} - \frac{1}{4}(2 + \epsilon). \quad (7.50)$$

In this case, generally both states $|1, 3\rangle_{\pm}$ have nonzero coupling to the state $|1, 3; 0, 0\rangle$ given by

$$\begin{aligned} \Omega_{fi} &= \eta_{\pm}^{(1,3)} \equiv \langle 1, 3 |_{\pm} H_{\text{RC}} | 1, 3; 0, 0 \rangle \\ &= \frac{1}{\sqrt{1 + (\gamma_{\pm}^{(1,3)})^2}} (\gamma_{\pm}^{(1,3)} + \sqrt{3}). \end{aligned} \quad (7.51)$$

The energy shifts for the two different possible processes are given by $\Delta E/U_{00}^{aa} = E_{\pm}^{(2,2)} - \frac{15}{4}$.

7.B Perturbation Theory

In this section we derive the corrections to the overlap function due to small hopping in perturbation theory following closely the method presented in Ref. [64]. We start with the zero hopping Hamiltonian H_0 with ground state $|\Omega\rangle$ and eigenenergy E_0 . We treat the hopping Hamiltonian, JH_1 with $H_1 = -\sum_{\langle i,j \rangle} b_i^\dagger b_j$, which has eigenstates denoted by $|\phi_{ij}\rangle$ and eigenenergies denoted by E_{ij} in perturbation theory. We proceed by determining a unitary transformation that transforms the total Hamiltonian $H = H_0 + JH_1$ into an effective Hamiltonian H' with the identical eigenspectrum but acting only in the unperturbed Hilbert space of the state $|\Omega\rangle$. The required unitary transformation may be written as $U = e^{-iS}$ and can be determined consistently to any order by writing $S = JS_1 + J^2S_2 + \dots$. We assume that S has only non-diagonal matrix elements which connect the unperturbed ground state $|\Omega\rangle$ and the excited states $|\phi_{ij}\rangle$. Using the unitary transformation we can directly calculate the correction to the particle density due to the hopping by computing $\langle \Omega | \tilde{n}_i | \Omega \rangle$ where $\tilde{n}_i \equiv U^\dagger n_i U$. We show in the following sections that it is sufficient to determine S to first order. Moreover, it is straightforward to show that to first order the matrix elements of S , i.e. S_1 , are given by

$$\langle \Omega | iS_1 | \phi_{ij} \rangle = \frac{\langle \Omega | V | \phi_{ij} \rangle}{E_0 - E_{ij}}. \quad (7.52)$$

7.B.1 Mott-insulator

In this section we derive the leading order correction to the overlap function for small hopping in perturbation theory for the MI phase. We begin by expanding S to fourth order and calculate the average corrected density to be

$$\langle \tilde{n}_i \rangle = \langle n_i \rangle + \sum_{j=1}^4 J^j \langle A_j \rangle, \quad (7.53)$$

where

$$A_1 = [S_1, n_i], \quad (7.54)$$

$$A_2 = [S_2, n_i] - \frac{1}{2} [S_1, [S_1, n_i]], \quad (7.55)$$

$$A_3 = [S_3, n_i] - \frac{1}{2} ([S_1, [S_2, n_i]] + [S_2, [S_1, n_i]]) - \frac{1}{6} [S_1, [S_1, [S_1, n_i]]], \quad (7.56)$$

$$A_4 = [S_4, n_i] - \frac{1}{2} [S_2, [S_2, n_i]] + \frac{1}{24} [S_1, [S_1, [S_1, [S_1, n_i]]]] - \frac{1}{2} ([S_1, [S_3, n_i]] + [S_3, [S_1, n_i]]). \quad (7.57)$$

First, note that since we have chosen S to have no diagonal matrix elements $\langle [S_n, n_i] \rangle = 0$ to all orders.

We now calculate the first part of the overlap function (7.3) and find

$$\begin{aligned} [\langle \tilde{n}_i \rangle^2]_{av} &= [\langle n_i \rangle^2]_{av} + J^2 [\langle n_i \rangle \langle A_2 \rangle]_{av} \\ &\quad + J^3 [\langle n_i \rangle \langle A_3 \rangle]_{av} + J^4 [\langle n_i \rangle \langle A_4 \rangle + \langle A_2 \rangle^2]_{av} + \mathcal{O}(J^5). \end{aligned} \quad (7.58)$$

Similarly, for the second term of the overlap function (7.3) we obtain the following expression

$$\begin{aligned} [\langle \tilde{n}_i \rangle^2]_{av} &= [\langle n_i \rangle^2]_{av} + J^2 [\langle n_i \rangle]_{av} [\langle A_2 \rangle]_{av} + J^3 [\langle n_i \rangle]_{av} [\langle A_3 \rangle]_{av} \\ &\quad + J^4 ([\langle n_i \rangle]_{av} [\langle A_4 \rangle]_{av} + [\langle A_2 \rangle]_{av}^2) + \mathcal{O}(J^5). \end{aligned} \quad (7.59)$$

Using $\langle n_i \rangle = n_0$ we obtain the following expression for the overlap

$$q = [\langle \tilde{n}_i \rangle^2]_{av} - [\langle \tilde{n}_i \rangle]_{av}^2 = J^4 ([\langle A_2 \rangle^2]_{av} - [\langle A_2 \rangle]_{av}^2) + \mathcal{O}(J^5). \quad (7.60)$$

Note that because $\langle n_i \rangle = n_0$ at all lattice sites (independent of the disorder) the second- and third-order contributions cancel.

To determine the required commutators $[S_1, [S_1, n_i]]$ we write S_1 and n_i as projectors

$$S_1 = -i \sum_{\langle jk \rangle} c_{jk} |\Omega\rangle \langle \phi_{jk}| + \text{H.c.}, \quad (7.61)$$

$$n_i = n_0 |\Omega\rangle \langle \Omega| + n_0 \sum_{\langle jk \rangle \neq i} |\phi_{jk}\rangle \langle \phi_{jk}| + (n_0 + 1) \sum_{\langle j(i) \rangle} |\phi_{ij}\rangle \langle \phi_{ij}| + (n_0 - 1) \sum_{\langle j(i) \rangle} |\phi_{ji}\rangle \langle \phi_{ji}|, \quad (7.62)$$

where

$$c_{jk} = \frac{\langle \Omega | V | \phi_{jk} \rangle}{E_0 - E_{jk}}, \quad (7.63)$$

$$|\Omega\rangle = \prod_i |n_0\rangle_i, \quad (7.64)$$

and

$$|\phi_{jk}\rangle = |n_0 + 1\rangle_j |n_0 - 1\rangle_k \prod_{l \neq i, j} |n_0\rangle_l. \quad (7.65)$$

Using these expressions it is straightforward to compute the expectation value of the density correction

$$\langle A_2 \rangle = n_0(n_0 + 1) \sum_{\langle j(i) \rangle} \left(\frac{1}{(E_0 - E_{ij})^2} - \frac{1}{(E_0 - E_{ji})^2} \right), \quad (7.66)$$

where $E_0 - E_{ij} = -U + \Delta_j - \Delta_i$.

7.B.2 Bose-glass

In this section we derive the leading order correction to the overlap function for small hopping in perturbation theory for the BG phase. Again we consider the corrected density $\langle \tilde{n}_i \rangle$ as given in Eq. (7.53) but only up to second order in J . Again we have $\langle [S_n, n_i] \rangle = 0$ because we have chosen S to have no diagonal matrix elements. Thus the overlap to second order is given by

$$q = [\langle \tilde{n}_i \rangle^2]_{av} - [\langle \tilde{n}_i \rangle^2]_{av}^2 = q_0 - J^2 ([\langle n_i \rangle \langle A_2 \rangle]_{av} - [\langle n_i \rangle]_{av} [\langle A_2 \rangle]_{av}) + \mathcal{O}(J^3), \quad (7.67)$$

where $q_0 = [\langle n_i \rangle^2]_{av} - [\langle n_i \rangle]_{av}^2$ is the overlap at zero hopping derived in Sec. 7.4.1. Since $\langle n_i \rangle$ is now site dependent the second-order contribution does not vanish.

To determine the required commutators $[S_1, [S_1, n_i]]$ we again write S_1 and n_i as projectors

$$S_1 = -i \sum_{\langle jk \rangle} c_{jk} |\Omega\rangle \langle \phi_{jk}| + \text{H.c.}, \quad (7.68)$$

$$\begin{aligned} n_i &= (n_0 + d_i) |\Omega\rangle \langle \Omega| + (n_0 + d_i) \sum_{\langle jk \rangle \neq i} |\phi_{jk}\rangle \langle \phi_{jk}| + (d_i(n_0 + 2) + (1 - d_i)(n_0 + 1)) \\ &\quad \times \sum_{\langle j(i) \rangle} |\phi_{ij}\rangle \langle \phi_{ij}| + (d_i n_0 + (1 - d_i)(n_0 - 1)) \sum_{\langle j(i) \rangle} |\phi_{ji}\rangle \langle \phi_{ji}|, \end{aligned} \quad (7.69)$$

where

$$c_{jk} = \frac{\langle \Omega | V | \phi_{jk} \rangle}{E_0 - E_{jk}}, \quad (7.70)$$

with

$$|\Omega\rangle = \prod_l [d_l |n_0\rangle_l + (1 - d_l) |n_0 + 1\rangle_l], \quad (7.71)$$

and

$$\begin{aligned} |\phi_{jk}\rangle &= [d_j |n_0 + 2\rangle_j + (1 - d_j) |n_0 + 1\rangle_j] [d_k |n_0\rangle_k + (1 - d_k) |n_0 - 1\rangle_k] \\ &\times \prod_{l \neq jk} [d_l |n_0 + 1\rangle_l + (1 - d_l) |n_0\rangle_l], \end{aligned} \quad (7.72)$$

where $d_{j,k,l}$ ($1 - d_{j,k,l}$) is zero (one) for $\Delta_{j,k,l} = \Delta$ ($\Delta_{j,k,l} = -\Delta$). Again, using these expressions it is straightforward to compute the expectation value of the density correction and for $n_0 \geq 1$ we obtain

$$\langle A_2 \rangle = \sum_{\langle j(i) \rangle} \left(\frac{\gamma_{ij}^2}{(E_0 - E_{ij})^2} - \frac{\gamma_{ji}^2}{(E_0 - E_{ji})^2} \right), \quad (7.73)$$

where

$$\gamma_{ij} = (d_i \sqrt{n_0 + 2} + (1 - d_i) \sqrt{n_0 + 1}) (d_j \sqrt{n_0 + 1} + (1 - d_j) \sqrt{n_0}), \quad (7.74)$$

and $E_0 - E_{ij} = -U[d_i + (1 - d_j)] + \Delta_j - \Delta_i$.

7.C Mean Field Theory

We replace the annihilation operators b_i in the Hamiltonian (7.1) by the mean field $\psi_i = e^{i\phi} \sqrt{n_0 + \delta n_i}$ and expand the fluctuations $\delta n_i \ll n_0$ up to second order to obtain

$$\begin{aligned} H(\delta n_i) &= -\frac{J}{4n_0} \sum_{\langle ij \rangle} \delta n_i \delta n_j - \frac{1}{2} (\delta n_j^2 + \delta n_i^2) + \frac{U}{2} \sum_i \delta n_i^2 + (2n_0 - 1) \delta n_i \\ &\quad - \sum_i (\mu + zJ - \Delta_i) \delta n_i + \mathcal{O}(\delta n_i^3). \end{aligned} \quad (7.75)$$

Next, we minimize Eq. (7.75) at fixed particle number which is equivalent to requiring $[\delta n_i]_{av} = 0$. Using Eq. (7.33) and consistently solving gives

$$\delta n_i = \frac{\Delta(2p - 1) - \Delta}{U + \frac{zJ}{2n_0}}. \quad (7.76)$$

Finally, then the overlap can be expressed in terms of these fluctuations as follows

$$q = [\langle n_i \rangle^2]_{av} - [\langle n_i \rangle]_{av}^2 = [\delta n_i^2]_{av} - [\delta n_i]_{av}^2. \quad (7.77)$$

Substituting Eq. (7.76) into Eq. (7.77) and performing the disorder average for a bimodal distribution gives the result in Eq. (7.34) for the overlap function q .

Bibliography

- [1] K. Binder and A. P. Young, *Rev. Mod. Phys.* **58**, 801 (1986).
- [2] M. Mézard, G. Parisi, and M. A. Virasoro, *Spin Glass Theory and Beyond*, (World Scientific, Singapore, 1987).
- [3] A. P. Young, editor, *Spin Glasses and Random Fields*, (World Scientific, Singapore, 1998).
- [4] A. M. Finkel'Stein, *Physica B* **197**, 636 (1994).
- [5] M. P. A. Fisher, *Phys. Rev. Lett.*, **65**, 923 (1990).
- [6] P. A. Lee and T. V. Ramakrishnan, *Rev. Mod. Phys.* **57**, 287 (1985).
- [7] G. Parisi, *Phys. Rev. Lett.* **43**, 1754 (1979).
- [8] M. Mézard, G. Parisi, N. Sourlas, G. Toulouse, and M. Virasoro, *Phys. Rev. Lett.* **52**, 1156 (1984).
- [9] A. J. Bray and M. A. Moore, *Scaling theory of the ordered phase of spin glasses*, L. Van Hemmen and I. Morgenstern, editors, *Heidelberg Colloquium on Glassy Dynamics and Optimization*, page 121, (Springer, New York, 1986).
- [10] D. S. Fisher and D. A. Huse, *Phys. Rev. Lett.* **56**, 1601 (1986).
- [11] D. A. Huse and D. S. Fisher, *J. Phys. A* **20**, L997 (1987).
- [12] C. Newman and D. L. Stein, *Phys. Rev. Lett.* **76**, 515 (1996).
- [13] F. Krzakala and O. C. Martin, *Phys. Rev. Lett.* **85**, 3013 (2000).
- [14] M. Palassini and A. P. Young, *Phys. Rev. Lett.* **85**, 3017 (2000).
- [15] M. P. A. Fisher, P. B. Weichman, G. Grinstein, and D. S. Fisher, *Phys. Rev. B* **40**, 546 (1989).
- [16] B. Damski, J. Zakrzewski, L. Santos, P. Zoller, and M. Lewenstein, *Phys. Rev. Lett.* **91**, 080403 (2003).
- [17] A. Sanpera, A. Kantian, L. Sanchez-Palencia, J. Zakrzewski, and M. Lewenstein, *Phys. Rev. Lett.* **93**, 040401 (2004).
- [18] R. Roth and K. Burnett, *J. Opt. B* **5**, S50 (2003).
- [19] R. Roth and K. Burnett, *Phys. Rev. A* **67**, 031602 (2003).
- [20] I. Bloch, J. Dalibard, and W. Zwerger, arXiv:cond-mat/0704.3011 (2007).

- [21] M. Lewenstein, A. Sanpera, V. Ahufinger, B. Damski, A. Sen, and U. Sen, *Adv. Phys.* **56**, 243 (2007).
- [22] D. Jaksch and P. Zoller, *Ann. Phys.* **315**, 52 (2004).
- [23] S. F. Edwards and P. W. Anderson, *J. Phys. F: Met. Phys.* **5**, 965 (1975).
- [24] T. Stöferle, H. Moritz, C. Schori, M. Köhl, and T. Esslinger, *Phys. Rev. Lett.* **92**, 130403 (2004).
- [25] J. Sebby-Strabley, M. Anderlini, P. S. Jessen, and J. V. Porto, *Phys. Rev. A* **73**, 033605 (2006).
- [26] S. Fölling, S. Trotzky, P. Cheinet, M. Feld, R. Saers, A. Widera, T. Müller, and I. Bloch, *Nature* **448**, 1029 (2007).
- [27] I. B. Spielman, W. D. Phillips, and J. V. Porto, *Phys. Rev. Lett.* **98**, 080404 (2007).
- [28] G. K. Campbell, J. Mun, M. Boyd, P. Medley, A. E. Leanhardt, L. G. Marcassa, D. E. Pritchard, and W. Ketterle, *Science* **313**, 649 (2006).
- [29] Note that our overlap function is defined as the averaged squared deviation from the mean. That is why, while the overlap of the two Mott replicas is indeed perfect, our overlap function, defined via deviations, is zero.
- [30] J. E. Lye, L. Fallani, M. Modugno, D. S. Wiersma, C. Fort, and M. Inguscio, *Phys. Rev. Lett.* **95**, 070401 (2005).
- [31] C. Fort, L. Fallani, V. Guarrera, J. E. Lye, M. Modugno, D. S. Wiersma, and M. Inguscio, *Physical Review Letters* **95**, 170410 (2005).
- [32] D. Clément, A. F. Varón, M. Hugbart, J. A. Retter, P. Bouyer, L. Sanchez-Palencia, D. M. Gangardt, G. V. Shlyapnikov, and A. Aspect, *Phys. Rev. Lett.* **95**, 170409 (2005).
- [33] D. Clément, A. F. Varón, J. A. Retter, L. Sanchez-Palencia, A. Aspect, and P. Bouyer, *New J. Phys.* **8**, 165 (2006).
- [34] T. Schulte, S. Drenkelforth, J. Kruse, W. Ertmer, J. Arlt, K. Sacha, J. Zakrzewski, and M. Lewenstein, *Phys. Rev. Lett.* **95**, 170411 (2005).
- [35] L. Fallani, J. E. Lye, V. Guarrera, C. Fort, and M. Inguscio, *Phys. Rev. Lett.* **98**, 130404 (2007).
- [36] J. Billy, V. Josse, Z. Zuo, A. Bernard, B. Hembrecht, P. Lugan, D. Clément, L. Sanchez-Palencia, P. Bouyer, and A. Aspect, arXiv:0804.1621 (2008).

- [37] G. Roati, C. D’Errico, L. Fallani, M. Fattori, C. Fort, M. Zaccanti, G. Modugno, M. Modugno, and M. Inguscio, arXiv:0804.2609 (2008).
- [38] P. J. Lee, M. Anderlini, B. L. Brown, J. Sebby-Strabley, W. D. Phillips, and J. V. Porto, *Phys. Rev. Lett.* **99**, 020402 (2007).
- [39] A. V. Gorshkov, L. Jiang, M. Greiner, P. Zoller, and M. D. Lukin, arXiv:cond-mat/0706.3879 (2007).
- [40] P. Vignolo, Z. Akdeniz, and M. P. Tosi, *J. Phys. B.* **36**, 4535 (2003).
- [41] U. Gavish and Y. Castin, *Phys. Rev. Lett.* **95**, 020401 (2005).
- [42] D. Jaksch, C. Bruder, J. I. Cirac, C. W. Gardiner, and P. Zoller, *Phys. Rev. Lett.* **81**, 3108 (1998).
- [43] K. Günter, T. Stöferle, H. Moritz, M. Köhl, and T. Esslinger, *Phys. Rev. Lett.* **96**, 180402 (2006).
- [44] S. Ospelkaus, C. Ospelkaus, O. Wille, M. Succo, P. Ernst, K. Sengstock, and K. Bongs, *Phys. Rev. Lett.* **96**, 180403 (2006).
- [45] M. Greiner, O. Mandel, T. Esslinger, T. W. Hänsch, and I. Bloch, *Nature* **415**, 39 (2002).
- [46] R. C. Kuhn, C. Miniatura, D. Delande, O. Sigwarth, and C. A. Müller, *Phys. Rev. Lett.* **95**, 250403 (2005).
- [47] A. de Martino, M. Thorwart, R. Egger, and R. Graham, *Phys. Rev. Lett.* **94**, 060402 (2005).
- [48] R. T. Scalettar, G. G. Batrouni, and G. T. Zimanyi, *Phys. Rev. Lett.* **66**, 3144 (1991).
- [49] S. Rapsch, U. Schollwöck, and W. Zwerger, *Europhys. Lett.* **46**, 559 (1999).
- [50] K. Byczuk, W. Hofstetter, and D. Vollhardt, *Phys. Rev. Lett.* **94**, 056404 (2005).
- [51] V. I. Yukalov, E. P. Yukalova, K. V. Krutitsky, and R. Graham, *Phys. Rev. A* **76**, 053623 (2007).
- [52] K. V. Krutitsky, M. Thorwart, R. Egger, and R. Graham, arXiv:cond-mat/0801.2343 (2008).
- [53] P. Sengupta and S. Haas, *Phys. Rev. Lett.* **99**, 050403 (2007).
- [54] G. Parisi, *Phys. Rev. Lett.* **50**, 1946 (1983).

- [55] K. Winkler, G. Thalhammer, F. Lang, R. Grimm, J. Hecker Denschlag, A. J. Daley, A. Kantian, H. P. Büchler, and P. Zoller, *Nature* **441**, 853 (2006).
- [56] Note that in some situations, quantum averaging can be exploited to assist in producing disorder averages, see B. Paredes, F. Verstraete, and J. I. Cirac, *Phys. Rev. Lett.* **95**, 140501 (2005).
- [57] For small systems it may be necessary to improve the statistics by a repetition of the measurement.
- [58] In case the occupation number distribution in each replica is not equal, each should be individually addressed and measured, e.g., using a magnetic field gradient during the measurement.
- [59] These points can easily be determined analytically by equating energy shifts for different total particle numbers (as given in Tab. 7.1) and solving for ϵ .
- [60] D. Sherrington and S. Kirkpatrick, *Phys. Rev. Lett.* **35**, 1792 (1975).
- [61] T. Giamarchi, P. Le Doussal, and E. Orignac, *Phys. Rev. B* **64**, 245119 (2001).
- [62] G. Vidal, *Phys. Rev. Lett.* **91**, 147902 (2003).
- [63] G. Vidal, *Phys. Rev. Lett.* **93**, 040502 (2004).
- [64] C. Cohen-Tannoudji, J. Dupont-Roc, and G. Grynberg, *Atom Photon Interactions: Basic Processes and Applications*, (John Wiley & Sons Inc, New York, 1992).

ACKNOWLEDGMENTS

Last but not least, I want to thank everyone who helped and supported me during my studies and without whom this thesis would not have come to successful completion.

Firstly, I want to thank my mother Ursula and her partner Garry very much for their continued support during the highs and lows of my studies. I also wish to thank greatly my partner Sascha for his continued moral support, patience and understanding through all stages of my study. Thanks also to Rosemarie and Gerhard for their support.

Next I would like to thank Peter Zoller for giving me the opportunity to join his fantastic group and for many interesting physics discussions. I also want to thank Hans-Peter Büchler and Andrew Daley for their never ceasing patience and help in discussing my projects during most of my PhD. Foremost, however, I would like to thank Scott Parkins very much for offering me the possibility to work with him, and spending much time in interesting and productive physics discussions during a very large part of my PhD. I am also extremely grateful for Scott and Howard Carmichael's efforts that resulted in my two visits to the Quantum Optics group at the University of Auckland. In addition, I also want to thank my other collaborators Adrian Kantian, Helmut Katzgraber, Maciek Lewenstein, and Howard Carmichael, for many interesting and fruitful discussions. Of course I also wish to thank the following current and former group members in Innsbruck for many helpful and stimulating physics discussions: Andi Griessner, Peter Rabl, Viktor Steixner, Uri Gavish, Gavin Brennen, Andrea Micheli, Uwe Dorner, Tomasso Calarco, and Konstanze Jähne. Furthermore, I also would like to thank the secretaries Marion Grünbacher and Nicole Jorda for help with administrative matters, and also the past and present IT staff Julio Lamm-Knapp, Hans Embacher, Thomas Mayr, Mecit Sandicki, and Andreas Knabl for their technical assistance. I also want to thank all the staff of the Physics Department at the University of Auckland for their kind and helpful hospitality during both my stays.

Finally I wish to thank everybody who made my free time away from studies very enjoyable: Viktor, Andi, Peter, Helga, Andrew, Hans-Peter, Simon, Jürgen, Clemens, Irina, Ruth, Leo, Maggie, Michael, Linmei, Kate, Paul, Cleo and Willis. I especially wish to thank my office mate and good friend Konstanze for many excellent conversations (physics and beyond), laughs and her ever ready help in all things. Finally I want to thank my old friends and fellow scientists Duncan, Joel, and Brett, with whom I began my physics journey and who have given me moral support from down-under.

